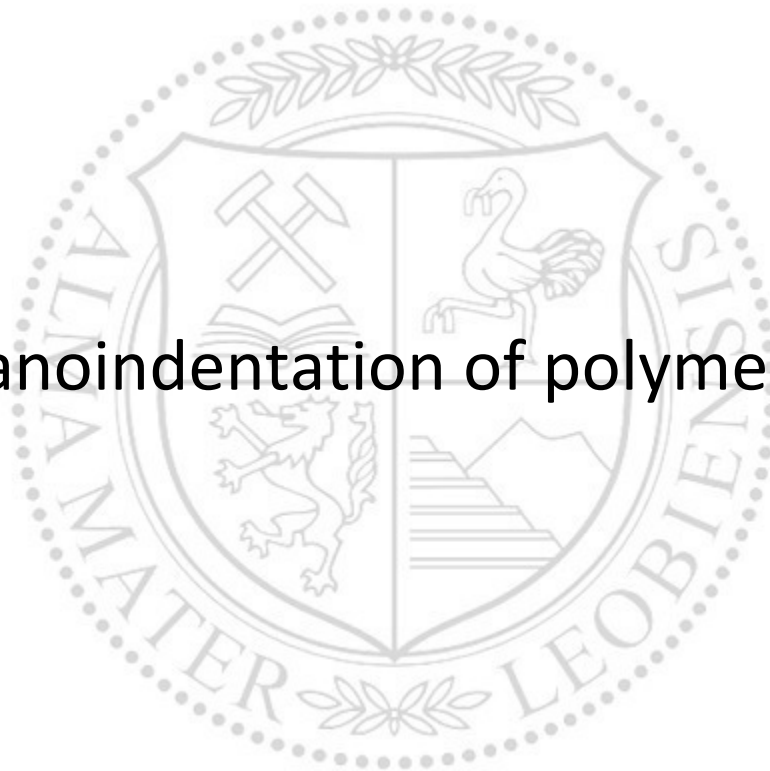**Chair of Materials Science and Testing of Polymers**

Doctoral Thesis

Nanoindentation of polymers

Petra Christöfl

December 2023

MONTANUNIVERSITÄT LEOBEN
www.unileoben.ac.at

AFFIDAVIT

I declare on oath that I wrote this thesis independently, did not use other than the specified sources and aids, and did not otherwise use any unauthorized aids.

I declare that I have read, understood, and complied with the guidelines of the senate of the Montanuniversität Leoben for "Good Scientific Practice".

Furthermore, I declare that the electronic and printed version of the submitted thesis are identical, both, formally and with regard to content.

Date

Signature Author

Petra Christöfl

Doctoral thesis

Nanoindentation of polymers

Authored by

DI Petra Christöfl

Submitted to
Chair of Materials Science and Testing of Polymers
Montanuniversität Leoben
Leoben, Austria

Conducted at
Polymer Competence Center Leoben GmbH
Leoben, Austria

Academic Supervisor
Univ.-Prof. Dipl.-Ing. Dr.mont. Gerald Pinter
Chair of Materials Science and Testing of Polymers
Montanuniversität Leoben

Co Supervisor
Priv.-Doz. Dipl.-Ing. Dr.mont. Gernot Oreski
Polymer Competence Center Leoben GmbH

ACKNOWLEDGEMENTS

FUNDING

ABSTRACT

Instrumented Nanoindentation (NI) has been a valuable tool to measure mechanical properties such as hardness and elastic modulus for various materials over the last 20 years. As a further development of hardness testing, it served as an appropriate method to determine mechanical properties, especially on thin films, on a small amount of sample or from special regions on a sample. NI of polymers have only been a marginal phenomenon over the last few years. The basic method in NI evaluation is the O&P method, which assumes elastic material relaxation after deformation. A polymer relaxes viscoelastic after deformation which makes the interpretation of NI data complex.

In this work, the emphasis lies on the investigation of polymers by NI. The main goals of this cumulative work are:

(I)   Evaluation of the O&P analysis and creep method in combination with material modelling on an isotropic (amorphous) material and compare it to a common macroscopic test.

(II)   Expansion of the evaluation from (I) to a more complex semi-crystalline system to evaluate the influence of morphology on the NI results.

(III)   Bring results from (I) and (II) into application where the occurrence of polymeric aging are detected by NI.

(IV)   Introduce an innovative sample preparation method to investigate polymeric multilayers in cross-section.

After a short introduction to NI of polymers a state-of-the-art section reviews literature ranging from the mechanical behaviour of polymers to NI methods and techniques. In the first publication NI was used to examine the viscoelastic properties of poly(methyl methacrylate) (PMMA) as an amorphous polymer model. An evaluation combining adhesive contact and empiric spring-dashpot models was applied to obtain the instantaneous elastic modulus E_0 and the infinitely elastic modulus E_∞ from NI creep curves. The value of E_0 was compared to moduli obtained with atomic force microscopy-based NI (AFM-NI) and macroscopic compression tests. Furthermore, the elastic modulus was evaluated by the O&P method for the NI and AFM-NI results. Comparison of the elastic modulus E_0 from the creep measurements of NI and AFM-NI to compression tests revealed good agreement of the results. However, only the O&P-based AFM-NI results yielded to lower values.

In paper two the material selection was expanded from amorphous to semi-crystalline polymers, as the influence of morphological structures such as spherulites or crystal-lamellae on localized NI depth-force behaviour is discussed controversially in literature. The main objective of paper two was to determine the influence of crystalline zones of semi-crystalline POM (Polyoxymethylene) on NI results. A POM tensile bar was investigated by NI at various positions of the cross-section. Areas at the edge of the sample had a lower modulus than areas in the middle of the cross-section. This agreed with polarized light microscopy results showing a skin layer with less crystallinity close to the sample edge. Semi-crystallinity influenced the NI results obtained for POM. The mean of the modulus distribution over the POM cross-section was in good agreement with macroscopic compression test results.

In paper three a fast and sensitive method to detect polymer aging at an early stage was developed by NI. For this purpose, a commercially available transparent and 50 micrometer thick polyethylene terephthalate (PET) film was aged under different artificial conditions. The evolution of mechanical properties with rising aging time was investigated via NI methods established in paper one and two and macroscopic tensile testing. Physical aging was monitored by the first heating of differential scanning calorimetry (DSC) and chemical aging was studied with gel permeation chromatography (GPC). NI data was compared to tensile test data with good agreement between the results on the nano- and macroscale. A correlation between GPC data and NI creep data indicated a primarily

chemical aging of the present PET films. Paper three states that NI is an appropriate method to determine the degradation of PET at an early stage.

In paper four NI on thin, polymeric multilayer film cross-sections were studied. Here NI violated assumptions of semi-infinite and homogeneous samples because NIs were always near free edges and heterophase interfaces. The structural compliance method was used to correct NI results for specimen-scale flexing and edge effects, where the effect of both edges and specimen-scale flexing is to introduce a structural compliance (Cs). The Cs showed a strong position dependence applied to a polymeric multilayer. The effect was larger near the edges and layer interfaces. The Cs correction had little effect on the hardness values; however, the influence on measured elastic modulus was significant. The corrected modulus values tended to be higher than the uncorrected ones in the stiff layers.

KURZFASSUNG

Instrumentierte Nanoindentation (NI) hat sich in den letzten 20 Jahren als wertvolles Instrument zur Messung mechanischer Eigenschaften wie Härte und Elastizitätsmodul für verschiedene Materialien erwiesen. Als Weiterentwicklung der Härteprüfung diente sie als geeignete Methode zur Bestimmung mechanischer Eigenschaften insbesondere an dünnen Schichten, wenn nur eine geringe Probenmenge zur Verfügung steht oder wenn spezielle Bereiche einer Probe untersucht werden müssen. Die Untersuchung von Polymeren mittels NI war in den letzten Jahren nur eine Randerscheinung. Die grundlegende Methode bei der NI-Auswertung ist die O&P-Methode, die von einer elastischen Materialrelaxation nach der Verformung ausgeht. Ein Polymer entspannt sich nach der Verformung viskoelastisch, was die Interpretation der NI-Daten komplex macht.

In dieser Arbeit liegt der Schwerpunkt auf der Untersuchung von Polymeren durch NI. Die Hauptziele dieser kumulativen Arbeit sind:

(I)   die Auswertung der traditionellen Analyse von O&P und der Kriechmethode in Kombination mit Materialmodellierung an einem isotropen (amorphen) Material und der Vergleich mit makroskopischen Tests.

(II)   die Auswertung aus (I) auf ein komplexeres teilkristallines Material auszuweiten, um den Einfluss der Morphologie auf die NI-Ergebnisse zu bewerten.

(III)   die Ergebnisse aus (I) und (II) im Bereich Polymeralterung durch NI anzuwenden.

(IV)   die Einführung einer innovativen Probenvorbereitungsmethode zur Untersuchung von polymeren Multilayern im Querschnitt (IV).

In Publikation eins wurde NI zur Untersuchung der viskoelastischen Eigenschaften von Poly(methylmethacrylat) (PMMA) als amorphes Polymermodell verwendet. Eine Auswertung, die Kontakt- und empirische Feder-Dämpfer-Modelle kombiniert, wurde angewandt, um den momentanen Elastizitätsmodul E_0 und den unendlichen Elastizitätsmodul E_∞ aus NI-Kriechkurven zu erhalten. E_0 wurde mit Modulen aus Rasterkraftmikroskopie-NI (AFM-NI) und makroskopischen Drucktests verglichen. Der Vergleich von E_0 aus den Kriechmessungen von NI und AFM-NI mit Druckversuchen zeigt eine gute Übereinstimmung der Ergebnisse. Allerdings ergeben die O&P-basierten AFM-NI-Ergebnisse niedrigere Werte.

In Publikation zwei wurde der Einfluss von morphologischen Strukturen wie Sphärolithen oder Kristalllamellen auf lokale NI in der Literatur kontrovers diskutiert wird. Das Hauptziel von Publikation zwei ist es, den Einfluss kristalliner Zonen von teilkristallinem POM auf die NI-Ergebnisse zu bestimmen Ein POM-Zugstab wurde mittels NI im Querschnitt untersucht. Bereiche am Rand der Probe hatten ein niedrigeres E-Modul als Bereiche in der Mitte. Dies stimmt mit den Ergebnissen der Polarisationslichtmikroskopie überein, die eine Hautschicht mit geringerer Kristallinität in der Nähe des Probenrandes zeigen. Die Teilkristallinität beeinflusst die für POM erzielten NI-Ergebnisse. Der Mittelwert der Verteilung des E-Moduls über den POM-Querschnitt stimmt gut mit den Ergebnissen der makroskopischen Druckprüfung überein.

In Publikation drei wird gezeigt, dass NI eine schnelle und empfindliche Methode zum frühzeitigen Nachweis der Polymeralterung sein kann. Daher wurde eine transparente und 50 Mikrometer dicke Polyethylenterephthalat (PET)-Folie unter verschiedenen Bedingungen gealtert. Die Entwicklung der mechanischen Eigenschaften mit zunehmender Alterungszeit wurde mit Hilfe der in Publikation eins und zwei vorgestellten NI Methoden und makroskopischen Zugversuchen untersucht. Die physikalische Alterung wurde mittels Differential-Scanning-Kalorimetrie (DSC) überwacht, und die chemische Alterung wurde mittels Gelpermeationschromatographie (GPC) untersucht. NI und Zugversuchsdaten wurden mit guter Übereinstimmung verglichen. Eine Korrelation zwischen den GPC-Daten und den NI-Kriechdaten deutete darauf hin, dass die Alterung der vorliegenden PET-Folien in

erster Linie auf die chemische Alterung zurückzuführen ist. In Publikation drei wird festgestellt, dass NI eine geeignete Methode ist, um die frühzeitige Degradation von PET zu bestimmen.

In Publikation vier werden dünne, polymere Mehrschichtfolienquerschnitte mittels NI untersucht. Da hier die NI immer an freien Kanten und heterophasigen Grenzflächen auftritt, ist die Voraussetzung für die O&P Auswertung - halbunendliche und homogene Proben- nicht gegeben. Die Methode der strukturellen Nachgiebigkeit (Cs) wurde verwendet, um die NI-Ergebnisse in Bezug auf die Biegung der Probe und die Kanteneffekte zu korrigieren, wobei sowohl die Kanten als auch die Biegung der Probe eine Cs bewirken. Die Cs zeigte eine starke Positionsabhängigkeit bei der Anwendung auf eine polymere Mehrschicht und war in der Nähe der Kanten und der Schichtgrenzen größer. Die Cs-Korrektur hatte nur geringe Auswirkungen auf die Härtewerte; der Einfluss auf den gemessenen E-Modul war jedoch erheblich. Die korrigierten Modulwerte waren in den steifen Schichten tendenziell höher als die unkorrigierten Werte.

TABLE OF CONTENTS

LIST OF ABBRAVIATIONS

a	contact radius of an indenter tip
α	cone angle of a sphero-conical indenter tip
a_c	radius of the contact area
$A=f(h_c)$	contact area of the indenter tip
β	geometry factor of the indenter tip
b	Burgers vector
C_m	machine compliance
C_s	structural compliance
C_p	a compliance term related to specimen and indenter properties
C_t	total compliance
$C(x)$	1D height-height correlation function
AFM-Ni	Atomic Force Microscopy Nanoindentation
DMA	Dynamic Mechanical Analysis
E	elastic modulus
E_{eff}	Effective modulus
E_c	elastic modulus of the crystal phase
E_r	reduced elastic modulus
E'	storage modulus
E''	loss modulus
E^*	Complex modulus
ε	strain
ε_v	viscous strain
ε_e	elastic strain
F	load
F_{max}	maximum load
f_0	half amplitude of the quasi static force
ρ_g	density of geometrical dislocations
h_{max}	the contact depth of the indenter at the F_{max}
h_i	small indentation of the indenter before the contact force can be reached
H	hardness
H_a	hardness of the amorphous phase
H_c	hardness of the crystalline phase
Δh	number of shearing planes
h	penetration depth
h_p	permanent indentation depth
h_c	contact indentation depth
h_0	half amplitude of the quasi static force
l_c	thickness of crystal lamellar
ISE	Indentation size effect
m	fitting parameter for the O&P fit
NI	Nanoindentation
η	viscosity
O&P	Oliver and Pharr
PET	Polyethylene terephthalate
PMMA	poly(methyl methacrylate)
POM	Polyoxymethylene
R	Radius of a sphero-conical indenter tip
S	slope of the unloading curve of the load penetration curve

xi

S_s	sample stiffness
SPM	Scanning Probe Microscopy
Tg	Glass transition temperature
t_h	time from the start of the NI to the beginning of the unloading
θ	semi-angle of a Berkovich indenter tip
σ_{ee}	surface free energy of the crystals
σ	stress
σ_e	elastic stress
σ_v	viscous stress
V_c	volume fraction of the crystalline phase
δ	phase shift between stress and strain

PART I: INTRODUCTION, STRUCTURE AND STATE OF THE ART

1. INTRODUCTION AND STUCTURE OF THE THESIS

The trend towards miniaturization especially in electronics effects products among the whole value chain from smartphone interiors to batteries for cars. The base materials of those products range from metals, ceramics and also polymers. It is crucial to evaluate and understand the main material properties of products and devices to get an understanding of their (long-term) performance. The mechanical properties of a material which exemplify the reaction to an external force, let classify a material to its utility to a certain application and can also serve for lifetime predictions.

With ongoing miniaturization, the requirements to the mechanical properties of materials are rising but also the need of testing those parameters on a small scale or on a small amount of the sample is obvious. For this purpose, the scientists Warren Oliver and George Pharr introduced the so-called Oliver and Pharr method for measuring and mapping the mechanical properties of thin films, thin surfaces, and small amounts of material by Nanoindentation (NI). Nowadays hardness and elastic modulus are the most measured properties, but the technique has also been further developed for estimations in strain hardening, yield stress, creep and residual stress fracture toughness. [53, 54]

The method of Oliver and Pharr (O&P) was mainly developed for testing hard, rigid and isotropic materials which perform elastic-plastic under load. The behaviour of polymers is instead visco-elastic-plastic under load which makes the Oliver and Pharr method only applicable in a limited way.

There have been various efforts to perform NI on polymers in recent years varying from simply using NI O&P method on polymers neglecting their viscoelastic behaviour to NI creep tests in combination with material modelling approaches. [33, 39, 68, 69] A systematic study on how to use NI on a large variety of different polymer types, such as thermoplastics, thermoplastic elastomers, thermosets and elastomers is missing. This work will concentrate on the systematic investigation of NI on thermoplastic polymers. The structure of the thesis and the goals of the different chapters are presented following:

Part 1: Introduction, structure and state-of-the-art

Part 2: Collection of the papers, summary, conclusion and outlook

> Paper 1: Comprehensive investigation of viscoelastic properties of PMMA by
>
> nanoindentation
>
> Paper 2: Morphological characterization of semi-crystalline POM using nanoindentation
>
> Paper 3: Nanoindentation for fast investigation of PET film degradation
>
> Paper 4: Improved nanoindentation methods for polymer based multilayer film cross-sections

In the **introduction and state-of-the-art chapter**, a brief overview on the need for observations on NI of polymers is given. Furthermore, it describes the current status regarding NI of polymers. Thermoplastic polymers are mainly used within this work and therefore the state-of-the-art chapter describes the material properties and viscoelastic behaviour of thermoplastics. Then the recent methods and developments of NI with emphasis on polymers are described. Thermal drift and surface roughness are amongst others influencing NI on polymers and therefore adequately described within this chapter. The state-of-the -art chapter closes with the comparison of NI results with macroscopically tested mechanical properties.

The **collection of the publications** is the core of the thesis. In **paper one**, a "Comprehensive investigation of viscoelastic properties of PMMA" is explained by nanoindentation. PMMA here served

as a model system for an amorphous thermoplastic polymer. The goal of this paper was to compare NI methods such as O&P and creep to macroscopic tests like compression tests systematically.

The semi-crystalline POM was investigated by NI in the **second paper** "Morphological characterization of semi-crystalline POM using Nanoindentation". Here the focus lied on the investigation of crystalline phases in contrast to more amorphous phases of POM. The main goal was to quantify if and why the morphology of POM influences NI results.

The **third paper** deals with "Nanoindentation for fast investigation of PET film degradation". In this publication, a PET-based backsheet for PV application was examined in an aged and unaged version to find out if aging behaviour can be detected by NI.

The **fourth paper** deals with "Improved Nanoindentation methods for polymer-based multilayer film cross-sections". Here, an innovative sample preparation method gave rise to examine cross-sections of polymeric thin films in cross section without the influence of surrounding embedding material.

The **summary and conclusion** give a short overview about the main outcomes of the thesis. It also put the results in relation to each other and presents the big picture of the whole thesis. The **outlook** section clearly states a proposal for a continuation of this research based on the findings in the thesis.

2. STATE OF THE ART

I. Material properties of thermoplastic polymers

Polymers are classified according to their molecular structure into thermoplastics, elastomers and thermosets, whereby thermoplastics can be divided into amorphous and semi-crystalline thermoplastics. While elastomers and thermosets exhibit primary and secondary bonds between the molecular chains, thermoplastic polymers only have secondary bonds between their molecular chains, which can result in amorphous or crystalline phases. Amorphous phases exhibit chains arranged randomly in no particular order, whereas crystalline phases show ordered molecular chains. [18]

With proper material selection for the specific application, polymers show fairly good resistance to degradation when in contact with the environment. To ensure long-lasting high performance, the knowledge of aging mechanisms and their influence on material properties is crucial. Polymer degradation in terms of polymer aging can occur as a reversible (physical aging) or irreversible (chemical aging) process. In most cases, a combination of both mechanisms leads to changes in material properties [20].

Physical aging describes property changes of polymers and is mostly a result of a thermodynamically unstable condition of a polymer below glass transition temperature (Tg). These changes become obvious with the change of outer form, structure or the change of measurable physical properties. The main types of physical aging are relaxation, post-crystallization, segregation, plasticizer migration and agglomeration. Due to reversibility, changes are no longer present after melting. [20]

Chemical aging mostly changes the molecular weight and the chemical composition of a polymer by the occurrence of chemical reactions, for example, chain scission, oxidation, degradation, hydrolysis, post-condensation and post-polymerization. The chemical aging of polymers is irreversible and leads to modified material properties. [20]

Hardness H and elastic modulus E are important parameters used to describe the mechanical behaviour of polymers. In materials science, E is often obtained from uniaxial tensile testing, where the relation between stress and strain delivers E. Transverse contraction takes place perpendicular to stress and the relation between transverse strain and axial strain equals the Poisson's ratio v. [3] Hardness is defined as the resistance of a body against the penetration of another harder body. This

definition is simple but also blurry. Most of the standardized hardness tests use a hard indenter and press it perpendicular into the surface of a specimen. [32]

The mechanical properties of thermoplastics depend on their morphological properties such as crystallinity or crystal lamellar thickness. Crystallinity is described by a higher order of macromolecular chains presented as crystal lamellae. The degree of crystallinity is therefore the crystalline part in a polymer expressed in percent. The hardness of polymer phases has been well established in the literature [1, 25, 28] and is described by the additivity law [25]:

$$H = H_c v_c + H_a(1 - v_c) \tag{1}$$

with H_c, the hardness of the crystalline phase, H_a, the hardness of the amorphous phase and v_c the volume fraction of the crystalline phase. Such an additivity law is not described so far for the elastic modulus, although there is a dependence of elastic modulus and degree of crystallinity, where higher crystallinity leads to higher E. Ref. [26] presents a direct dependency of the thickness of crystal lamellar lc and Ec, the elastic modulus of the crystal phase of Polyethylene terephthalate (PET). In summary, both, the higher thickness of the crystal lamellar and higher crystallinity lead to higher E of PET.

Furthermore, also the hardness of the crystalline phase H_c is influenced by the crystal lamellar thickness l_c. With H_c^∞ the hardness of an infinitely thick crystal and b a parameter related to the ratio between the surface free energy of the crystals σ_{ee}, and the energy required to plastically deform them through several shearing planes Δh, H can be written as: [2, 15, 16]

$$H_c = \frac{H_c^\infty}{1 + \frac{b}{l_c}} \quad b = \frac{2\sigma_{ee}}{\Delta h} \tag{2}$$

II. Viscoelastic behaviour of thermoplastic polymers

One of the most important material parameters used is E, which describes the stress (σ)- strain (ε) behaviour for the elastic deformation of a material in terms of Hooks law $\sigma = E\varepsilon$. In contrast to metals and ceramics, polymers exhibit temperature and time-dependent strain. Polymeric materials show viscoelastic material response when being deformed, exhibiting mechanical properties between elastic solids and viscous fluids and all kinds of intermediate states.

An ideal elastic solid has a defined shape and deforms under external load, whereby the energy from deformation is stored and released once the external load is removed. An ideal viscous liquid offers no definite shape and flows irreversibly under external load. A viscoelastic polymer can be described by the interaction of elastic solids and viscous liquids. The flow of the viscous liquid fraction of the viscoelastic polymer causes a time dependency of the material when deforming according to Newton's law $\sigma = \eta\dot{\varepsilon}$, whereby η is the viscosity. [43]

The stiffness and strength of materials are often represented by stress-strain curves obtained by applying a deformation with a constant strain rate to a material. For elastic materials, the slope of such stress-strain curves is constant and proportional to the elastic modulus (Figure 1a). On the contrary, a viscoelastic material shows a non-linear stress-strain behaviour for constant strain rate deformation (Figure 1b), where the loading and unloading curve yields a hysteresis curve. Furthermore, varying strain rates will lead to varying stress-strain curves of the same material, thus viscoelastic materials show a strain rate dependency [43].
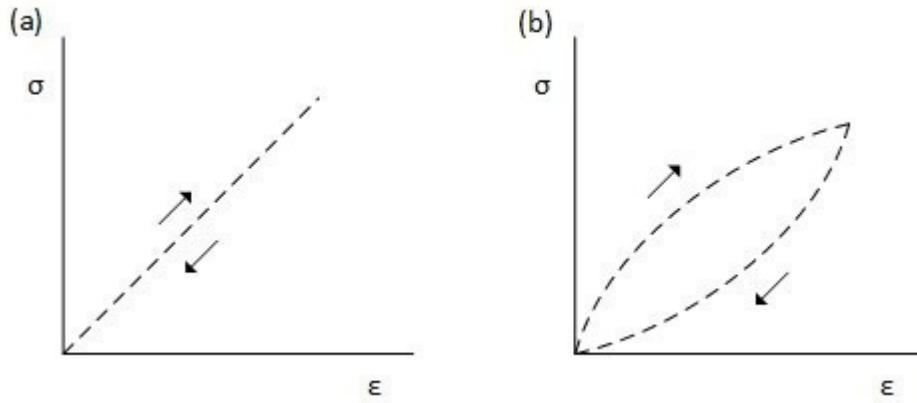
Figure 1: Stress-strain curves for elastic deformation (a) and viscoelastic deformation (b).

In the regime of small strains, polymers behave as linear viscoelastic. This means that Hook's and Newton's laws are valid. Here, viscoelastic materials can be described by combinations of independent springs and dashpots, representing the elastic and viscous part of the deformation. Only by being in the regime of linear viscoelasticity, stresses and strains can be decomposed additively.

There exists various literature about material modelling of viscoelastic materials in NI [7, 8, 13, 30]. Nevertheless, the basic material models of Kelvin-Voigt and Maxwell [18] are shown here exemplarily (see Figure 2).
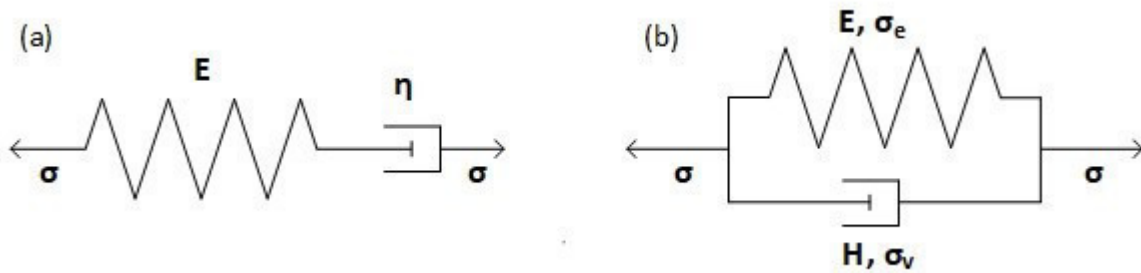

Figure 2: Basic viscoelastic models: (a) Maxwell element and (b) Kelvin-Voigt element.

The Maxwell model is a series connection of a spring and a dashpot element, representing the combined elastic and viscous deformation of a material. The total strain ε of the element consists of the elastic strain ε_e and the viscous strain ε_v as

$$\varepsilon = \varepsilon_e + \varepsilon_v. \tag{3}$$

The total stress σ provides a stress balance of the elastic stress σ_e and the viscous stress σ_v

$$\sigma = \sigma_e = \sigma_v \tag{4}$$

Hooks law delivers for the elastic part $\varepsilon_e = \sigma/E$ and for the viscous part $\dot{\varepsilon}_v = \sigma/\eta$. The derivation of strain $\dot{\varepsilon} = \dot{\varepsilon}_e + \dot{\varepsilon}_v$ delivers the material equation

$$\dot{\sigma} + \frac{E}{\eta} \cdot \sigma = E \dot{\varepsilon} \tag{5}$$

which can be solved analytically but also numerically.

Another basic model is the Kelvin-Voigt model with a spring and a dashpot in parallel. The total strain ε hereby corresponds to ε_e and ε_v with

$$\varepsilon = \varepsilon_e = \varepsilon_v. \tag{6}$$

4

The balance of strains delivers

$$\sigma = \sigma_e + \sigma_v \tag{7}$$

and the material equation

$$\sigma = E.\varepsilon_e + \eta.\dot{\varepsilon}_v = E.\varepsilon + \eta.\dot{\varepsilon}. \tag{8}$$

Creep and relaxation experiments are mostly modelled by a combination of Kelvin-Voigt and/or Maxwell elements.

III. Recent methods and developments of NI on polymers

NI is a further development of conventional hardness testing with a focus on highly local and low indentation depth testing. Micromechanical characterization with NI was developed for linear elastic and isotropic materials based on Hertzian theory with frictionless and non-confirming surfaces and is therefore mostly used for metals and ceramics. [23]

a. Standard methods of elastic modulus and hardness determination in NI

Basic research about stresses arising from pressing an elastic solid sphere into an infinite plate was performed by H. Hertz [38] in 1882. Sneddon expanded the theory of Hertz to sharp indenter tips pressing into infinitely large samples [63]. In 1986 it was Dorner and Nix [17], who introduced depth-sensing indentation instruments to determine E and H of thin foils. Nowadays, the analysis of indentation experiments is mostly done by the method of O&P [1] with the assumption of elastic-plastic behaviour of the material, limited to linear elasticity. For NI experiments, a hard indenter tip (see section NI tip shapes) is pressed into a material, while the progress of indentation depth with a given load (or vice versa) is recorded (Figure 3a and b). The power law fit of the unloading curve of the load (F) - penetration (h) curve is done by equation (9), with h_p, the permanent indentation depth, h_{max}, the contact depth of the indenter at the maximum force F_{max} and a fitting parameter m. [73]

$$\frac{F}{F_{max}} = \left(\frac{h - h_p}{h_{max} - h_p}\right)^m \tag{9}$$
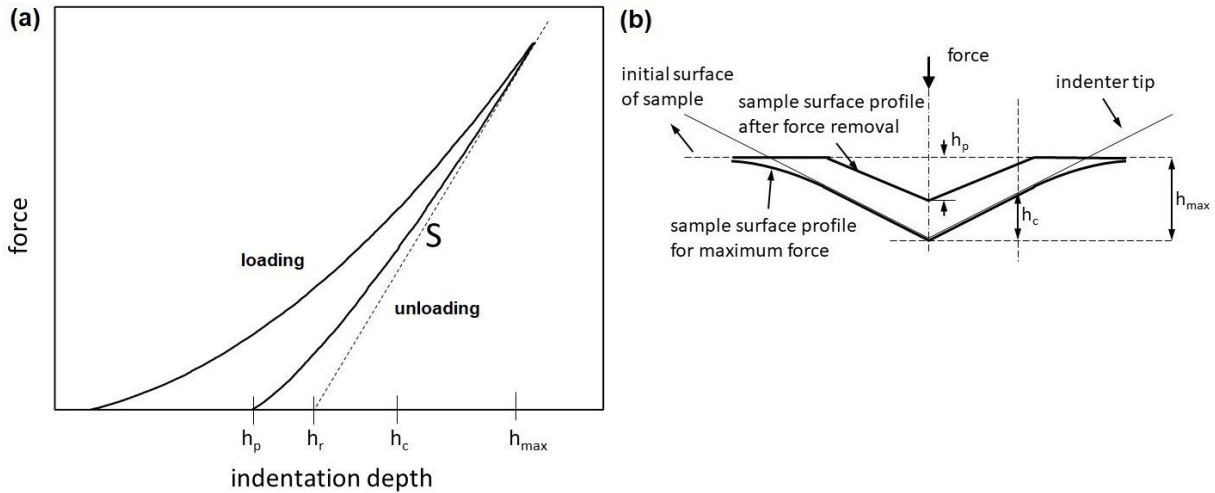
Figure 3: Schematic indentation load-displacement curve with the slope S of the unloading curve used in the O&P analysis and h_p, the depth of the residual impression, h_c the contact depth, h_{max}, the maximum indentation depth and h_r, the tangent indentation depth. (b) Cross section of a sharp indenter tip in contact with the sample. [12]

The contact stiffness S is the slope of the fit $S = \left(\frac{dF}{dh}\right)_{max}$ (10)

for the upper portion of the unloading curve.

The reduced modulus E_r is calculated by equation (11) [73]:

$$E_r = \frac{\pi S}{2\beta\sqrt{A(h_c)}} \qquad (11)$$

E_r is hereby obtained with the assumption that the unloading is purely elastic. $A=f(h_c)$ is the contact area of the indenter tip with the sample for the contact depth h_c and β, the geometry factor of the indenter tip which equals 1 for a sphero-conical indenter tip and 1.128 for a Berkovich indenter tip. The functional form $A=f(h_c)$ is determined by the indenter tip geometry and the depth of contact h_c [53] and is normally computed in a calibration process on a reference sample. Further information about different indenter shapes can be found in chapter NI tip shapes. With the correct contact area from calibration, the hardness can be determined with

$$H = \frac{F_{max}}{A(h_c)} \qquad (12)$$

The O&P method is the most applied in commercial depth sensing instruments software.

b. NI tip shapes

The following section mostly orients on the statements from A. C. Fischer-Cripps [23].

Indenter tips are usually made of diamond, a very hard but brittle material. With an oriented crystalline structure, the diamond shows a modulus in the range of 800-1200 GPa. For the NI analysis a value of 1000 GPa with a Poisson's ratio of 0.07 is mostly used. To avoid inconsistency for calibration as well as for the measurement, the indenter tip has to be clean, which can be accomplished by pressing the tip into a copper block.

There are three main types of NI tips: spherical, sharp (for example Berkovich) and flat-end tips.
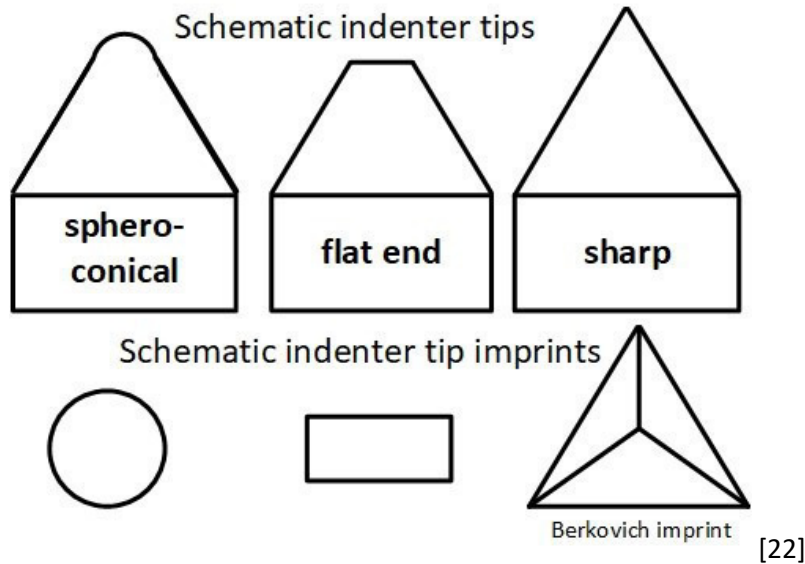
Figure 4: Schematic of the indenter tips: sphero-conical, flat end and sharp such as Berkovich

The indenter tip mainly used within this work is a spherical (or sphero-conical) tip, as it provides a soft transition from elastic to elastic-plastic contact. In the case of polymers, the contact is viscoelastic. The bigger the radius of a conical tip, the smaller the indentation depth for a smaller force. This leads to lower strains so that linear viscoelastic deformation can be achieved [67]. The spherical indenter tip is typically made as a sphero-cone with cone angle α for better mounting. For indentation, only the very tip is used. Spherical diamond tips are routinely fabricated in the range of 1 µm to 100 µm tip radius. The contact area of a spherical indenter is given by

6

$A=\pi(2Rh_c-h_c{}^2) \approx 2\pi Rh_c$ (13)

for small indentation depths (Figure 5a).

Berkovich indenter tips (Figure 5b) are the most widely used in NI, because they have the same projected area-to-depth ratio as Vickers indenters, which are used in conventional macroscopic hardness testing and served also as models for NI. So, the Berkovich indenter delivers a kind of comparability to common hardness testing. Berkovich indenters are easy to fabricate because the construction of a three-sided pyramid allows a meeting of the sides at a single point. In contrast to that, Vickers indenters are four-sided pyramids. The semi-angle (center line to face angle) of a typical Berkovich indenter θ is 65.27° and the tip radius is in the range of 50-100 nm. The projected area of contact is given by

$$A = 3\sqrt{3}h_c^2 \tan^2 \theta$$ (14)

which leads to A=24.494 $h_c{}^2 \approx$ 24.5 $h_c{}^2$ for the given angle.

The cube corner indenter tip is very similar to the Berkovich indenter, while it exhibits a semi-angle of 35.26°. A flat end indenter offers a constant contact area and no function of contact depth, which makes the interpretation of the data easier. But the friction at the edges of the tip has to be considered and opens new issues. Flat end indenter tips have not been used within this work.
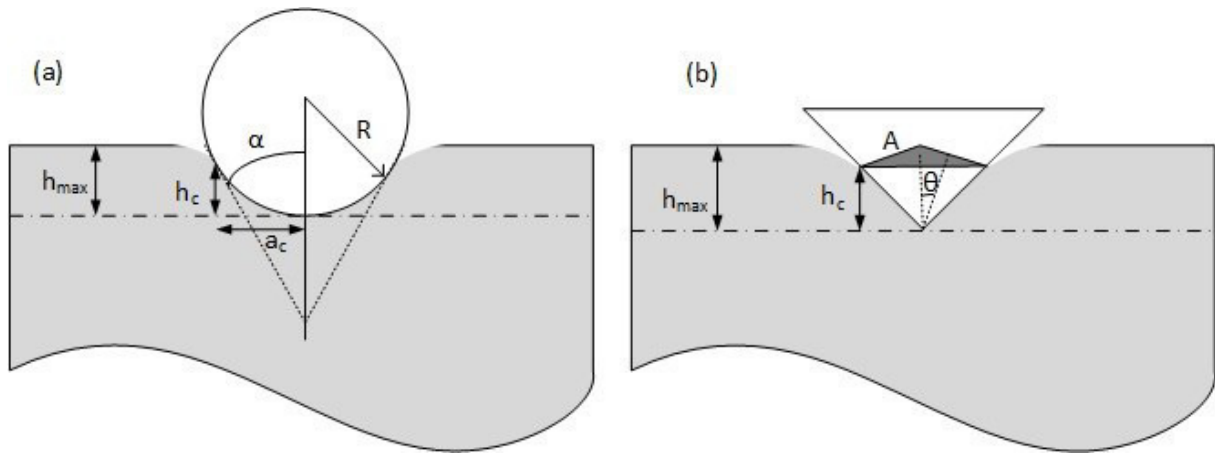

Figure 5: Parameters for the spherical (a) and the Berkovich (b) indenter tip: h_c: contact depth; a_c: the radius of the contact area; h_{max}: maximum indentation depth from the sample surface; R: radius of the spherical indenter; α and ϑ: semi angles of the faces for spherical and Berkovich indenter tip. The projected area A is shown although it would not be seen in an ideal side view inspired by [23].

One key element in indenting viscoelastic materials is the selection of the right tip shape regarding experimental objectives. One selection criterion is the representative strain. The concept of representative strain is often used to simplify the response of NI, where the NI strains are only dependent on their geometrical factors and not on material parameters. For a comprehensive study about representative strain, the reader is referred to [14].

The representative strain for the conical indenter is given by:

$$\varepsilon = 0.2 \ \cot\alpha$$ (15)

and leads to 8% for a Berkovich indenter tip. If larger strains are needed i.e. for crack introduction, sharper tips with higher representative strains may be useful. Furthermore, sharp tips introduce plastic deformation from the moment of contact, which is more suitable for the hardness evaluation of

7

polymers. For hardness evaluation, the exact determination of the area of contact is very important, which can be obtained more precisely for the Berkovich indenter tips due to geometry.

For spherical indenters, the transition from elastic to elastic-plastic contact is smooth. Here the representative strain varies according to load (indentation depth) and with a_c, the radius of contact at a given indentation depth h_c given by:

$$\varepsilon = 0.2\frac{a_c}{R} \tag{16}$$

c. Sample mounting

NI samples are typically mounted with a thin layer of glue on a hard support. Sometimes magnets or clamps are used to hold the sample rigidly. Indentation depths are usually in the range of μm. The surface should be flat, in a right angle to the indenter tip and parallel to the axis of translation. A small deviation of parallelism of maximum 25 μm over a crossing of 4 mm is usually tolerable. [24]

Within this work some samples are embedded in epoxy resin, ground and polished to examine the cross-section of a thin film. The author is aware that polishing a sample could influence its surface properties and therefore also influence the values for the mechanical properties.

d. Contact mechanics

Analysis of contact mechanics in NI can be useful for predictions concerning material behaviour. When performing NI, the indenter tip is brought into contact with the flat surface of a sample. This is well described in [59], the basis of the following paragraph.

In the so-called normal contact problem, two bodies are brought into contact with each other facing forces normal to their surfaces. In the case of spherical NI, the contact between a rigid sphere with the radius R and an elastic half-space (Hertz contact problem, see Figure 6) can be described in a qualitative estimation: With no elastic interactions between the sphere and the surface, the penetration depth is h_c. It follows that the contact radius is $a \approx \sqrt{2Rh_c}$ and the contact area corresponds to A=πa²≈2πRh_c. The size of the strongly deformed area is on the same scale as the contact diameter 2a. Therefore, the elastic deformation in this area corresponds to ε≈ h_c/2a. From Hooke's law, the correspondence principle is

$$\sigma = \varepsilon E \approx E\frac{h_c}{2a}. \tag{17}$$

Continuative with the relationship

$$F = \sigma A \approx \frac{Eh_c}{2a}a^2\pi \approx \frac{Eh_c}{2}\pi\sqrt{2Rh_c} = \frac{\pi}{\sqrt{2}}Eh_c^{3/2}R^{1/2} \tag{18}$$

the force is proportional to $h_c^{3/2}$.

In the case of plastic deformation, the dependence of the normal force σ_0 would be $\sigma_0 = \frac{F_N}{A}$ with the normal force F_N and the contact area A. Using the approximation A≈2πRh_c, the force dependence is

$$F_N=2\pi\sigma_0 Rh_c \tag{19}$$

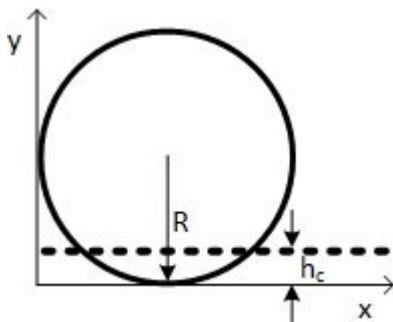which means that the force is directly proportional to the penetration depth h_c.

Figure 6: Hertz contact problem of a rigid sphere with an elastic half space with R, the radius of the sphere and the penetration depth h_c inspired by [59].

e. Investigation of time-dependent properties (Creep methods)

The main phenomena in polymers resulting from viscoelastic deformation are creep and stress relaxation. Deformation of a polymer under constant load leads to creep whereas constant deformation leads to stress relaxation.

The NI O&P method is mainly used to determine mechanical properties such as hardness and elastic modulus of polymers [6, 40, 62]. As this method is only valid for elastic deformation, sufficient low loads have to be used. Polymers show viscoelastic deformation, which means that creep occurs during indentation and a so-called "nose" (see Figure 7) appears on the unloading curve where the displacement increases upon load release [6] when the unloading phase follows right after the loading phase without a peak holding phase.
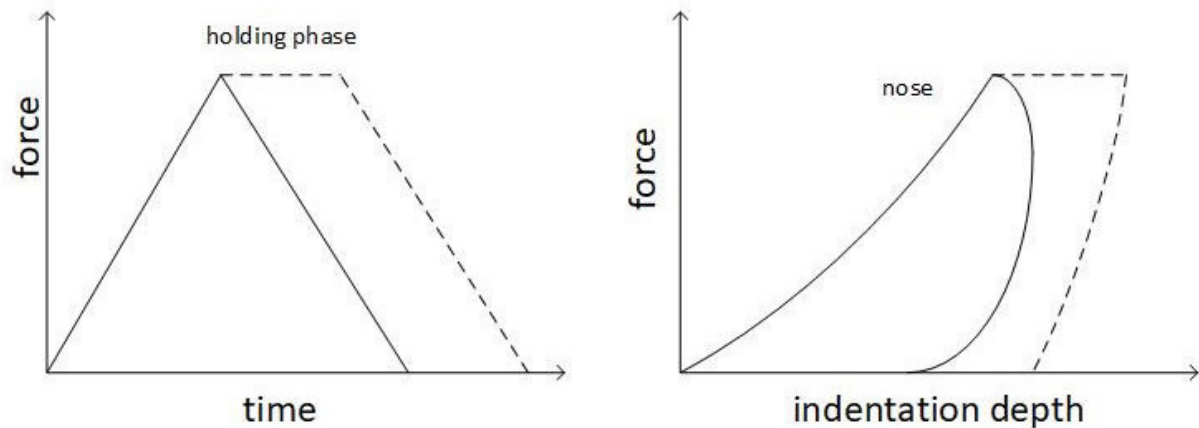

Figure 7: Indentation on viscoelastic material with holding phase (dashed line) and without holding phase (solid line) leading to nose formation: (a) loading (b) force - indentation depth response inspired by [6].

The creep rate of the investigated material is higher than the unloading rate resulting in a negative slope at the beginning of the unloading phase which makes the use of the O&P method inapplicable. The nose is usually avoided by the introduction of a holding period at peak load in combination with a rapid unloading rate. In Ref. [6] it is suggested to use a certain holding period of a few seconds to reach an equilibrium before unloading. Then creep will mainly happen during the holding phase. However, when indenting viscoelastic materials the influence of creep on the unloading curve is still a matter of discussion [12, 27]. Viscoelastic creep also affects the analysis of the unloading curve with the power-law fit (2.1) and leads to divergent stiffness values. In some cases, it results in a non-converging solution for the power-law fit in section a [69]. To overcome this problem, Feng and Ngang proposed to introduce a correction term for the contact stiffness, which is equal to the ratio of the indenter displacement rate at the end of the holding phase to the unloading rate [21].

Another possibility is to investigate the creep (relaxation) itself. There has been some effort to characterize NI creep or relaxation response from polymers [9, 10, 22, 24, 49, 67, 68, 76]. Here indentation with long hold periods is used to investigate creep curves and calculate furthermore viscoelastic properties.

By fitting displacement-time curves from creep experiments with spring-dashpot models consisting of elements presented in Figure 2, it is possible to determine the viscoelastic parameters, which has been done in several approaches in literature [11, 39, 45, 68, 74].

M. Oyen [55, 57, 58] shows results from spherical indentation creep tests with a large-diameter-sphere indenter tip for single and also multiple ramp-and-hold creep tests. While most of the force-controlled indentation studies are assuming step-loading conditions, which is experimentally impossible, M.Oyen [55] implements Boltzmann integral operators for the analytical solution of the multi-stage creep

9

experiments. The consideration of the ramping (loading) phase of the indentation creep experiment leads to a so-called ramp correction factor. For the analysis of creep functions corresponding to the Standard Linear Solid Model (spring in series with a Kelvin element) is used. This analysis can as well be extended to multi-stage creep experiments. Also experimental conditions and variables influence the modulus results [57]. Materials with small time dependency agree well with known values, which is verified in [12] for Poly(methyl methacrylate) (PMMA). Here, modulus values from creep tests show good accordance with conventional compression tests. For materials with increased time-dependency, a certain influence of maximum force and loading time on the modulus result is obtained.

In another work, M.Oyen [56] extends the study on viscoelastic materials with spherical tips to using Berkovich tips. The influence of plastic deformation on a sharp tip complicates the viscoelastic analysis of the materials.

One issue when conducting creep measurements is the thermal drift, which adds displacement from thermal fluctuations caused by the environment and instrumental inaccuracies. This thermal drift becomes important when dealing with low load and therefore low depth creep experiments (see chapter thermal drift).

    f.   *Atomic Force Microscopy Nanoindentation (AFM-NI)*

Atomic Force Microscopy (AFM) [5] was developed to investigate the topography of surfaces at the micro- and nanoscale. In contrast to other microscopy methods like Light Optical Microscopy or Scanning Electron Microscopy, which base on lenses and electromagnetic waves, AFM records the z-profile (depth profile) of a sample with the help of a sharp tip, scanning the sample laterally in x and y direction. [60] The tip is attached to the end of a micrometer size cantilever, which deflects according to the topography. For most commercial AFM devices, the cantilever movement is read out by optical feedback. [47]
The method provides quantitative 3D information of a sample in a non-destructive manner.
Typically, an AFM device consists of the following main components: piezo scanner, probe composed of tip and cantilever, feedback laser, position sensitive photodetector and controller (see Figure 8). [19]
The piezo scanner is used to position the sample in the x, y and z range and is mostly realized as a tube or line scanner. The tube scanner consists usually of five piezoelectric elements arranged in a tube form to move voltage controlled in x, y and z directions. With a tube scanner also larger samples can be investigated. Linear scanners provide highly linear behaviour and extreme accuracy and exhibit less crosstalk between x, y, and z compared to tube scanners.
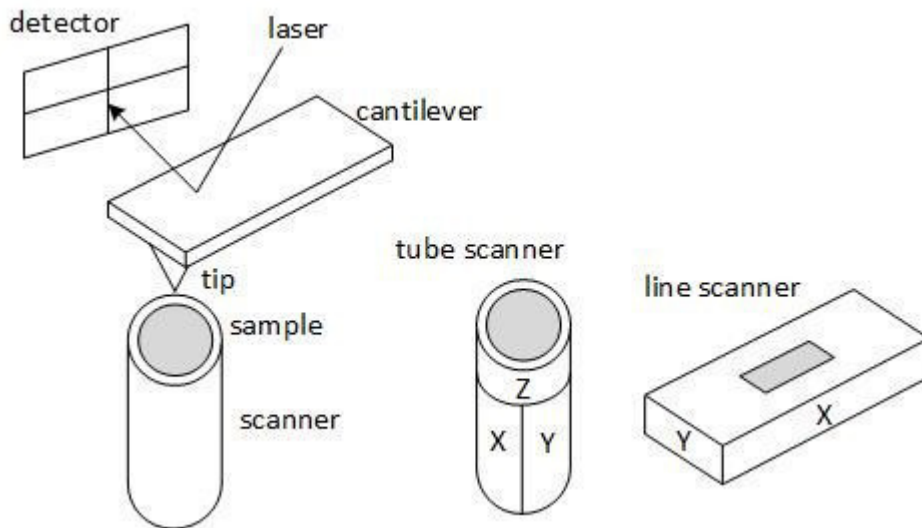
Figure 8: Sketch of an AFM device with tube or line scanner inspired by [75].

One key element of an AFM is the tip probe, i.e. the tip with the cantilever. It moves line-by-line in the so-called fast scan direction (x direction). Either, after each line in the fast scan direction, the scanner is set a step further in the slow scan direction (y direction). In this way, the area of interest is completely traced out. Often the slow scan direction is continuously increased during the fast scan action, causing a kind of zig-zag movement of the tip.

The basic AFM measurement modes are contact mode, non-contact mode [31] and intermittent contact mode. [41] For contact mode measurements, the tip scans across the sample with permanent tip-sample contact. Usually, the feedback is set to a fixed contact force, which means that a certain, present cantilever deflection has to be kept. This is achieved by moving the tip in z direction. The topography of the specimen is then recorded as z(x,y). For soft samples, contact mode can influence or even damage the surface due to the contact forces (especially uncontrolled lateral forces). For hard samples, the lifetime of the tip is reduced by wear.

To overcome these problems, AFM can also be operated in a non-contact mode [50], where the cantilever is oscillated close to its resonance frequency. In non-contact mode, the tip does not "touch" the surface. This means that the tip-surface separation is done with predominantly attractive forces. The signal is created by the attractive interaction between the tip and the force gradient emerging from forces of the surface, e.g. van der Waals forces. Different parameters can be utilized to operate the feedback, like amplitude, frequency or phase. The height z is adjusted so that either the shift in resonance frequency, the oscillation amplitude, or the phase shift between piezo drive and cantilever oscillation is kept constant. The recorded data is z (x,y). Real non-contact mode turned out to work reliably only under ultra-high vacuum conditions using either frequency modulation or a phase feedback loop. Operating in ambient conditions is difficult or often impossible. Therefore, intermittent contact mode has been established as the most common method for ambient air AFM imaging.

Intermittent contact mode (often also known as tapping mode) is a compromise between contact and non-contact mode. The cantilever is excited to vibrations slightly below its resonance frequency and near the surface of the sample. The tip touches the surface periodically so that it approaches the surface in each oscillation cycle close enough to come into the repulsive interaction regime. The tip-sample interaction causes damping, phase shift, or frequency shift of the cantilever oscillation. A feedback loop keeps either the amplitude (amplitude modulation) or the frequency shift (frequency modulation) constant by controlling the tip-sample distance. The z movement recorded as a function of lateral position delivers the topography z(x,y). This mode is most often used at ambient conditions and is well suited for soft materials such as polymers without demolishing the sample. Using intermittent contact mode in amplitude modulation also enables the detection of the mechanical

properties of polymers by recording the phase shift between the exciting oscillation and the cantilever's actual oscillation. [61]

The detection of the tip (cantilever) movement is based on measuring the deflection of the cantilever caused by the tip movement. For optical feedback (the most common method) a laser is focused on the end of the cantilever and its reflection is directed to a split 4-segment photodiode. If the cantilever deflects, the laser reflex is also moving. The position-sensitive split photodiode monitors the laser position. The cantilever deflection is determined by subtracting the light intensities received by the lower quarter and upper quarter of the photodiode. The intensity difference between the left and right quarters yields the torsion of the cantilever.

AFM acts as a highly sensitive force sensor, which also makes it suitable for NI experiments. [4] In AFM-NI the same probe tip that is used for topography scans is used to indent a material similar to conventional NI. Here, the AFM cantilever behaves like an actuator and load sensor at the same time. Thus, AFM NI delivers force and piezo distance data from the piezo's movement in the vertical direction (z), which depends on the cantilever deflection z_d and the indentation depth z_i. To get the correct indentation depth, the cantilever deflection z_d has to be subtracted from z: $z_i = z - z_d$ (Figure 9). After performing this correction, the force-distance plot from AFM NI can be evaluated.
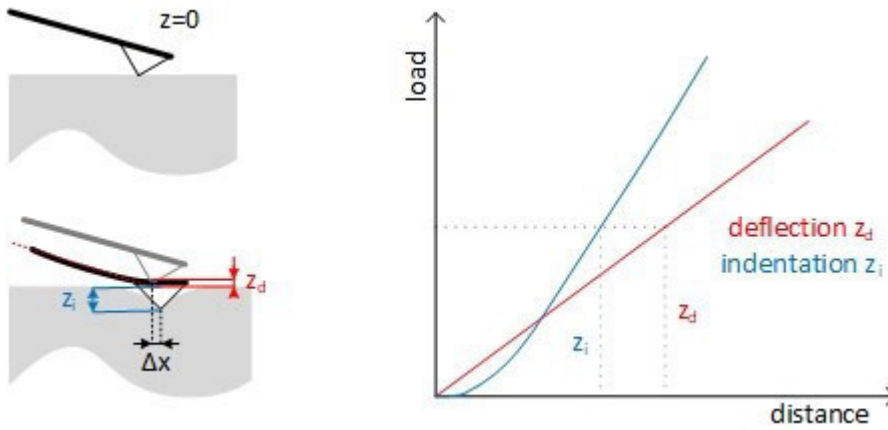

Figure 9: Sketch of an AFM NI experiment with corresponding force-distance plot inspired by [29].

One main difference between NI and AFM NI is the occurrence of a lateral movement and slight rotation of the tip during indentation (Δx in Figure 9). Conventional NI only deals with vertical tip movement whereas AFM NI exhibits vertical and lateral tip movement, which influences the determination of H and E.

g. Dynamic methods

NI provides the possibility to identify the viscoelastic parameters of a polymer either by creep testing or dynamic mechanical testing. Dynamic Mechanical Analysis (DMA) works with an overlay of a dynamic force and a quasistatic force and is well described in [46], which serves as the foundation of the subsequent chapter. Displacement following the loading force exhibits a phase shift δ to the force oscillations (Figure 10). The storage modulus (E') represents the elastic portion or the stored energy of the complex modulus and is associated with the stiffness of a polymer. The loss modulus (E'') represents the viscous part or the dissipated energy in a polymer, which is caused by internal friction processes like molecular motion, relaxation processes, transitions, morphology and other structural inhomogeneities. E' and E'' are related to σ_0 and ε_0, the instantaneous stress and strain:

$$E' = \frac{\sigma_0}{\varepsilon_0} \cos \delta \qquad\qquad (19)$$

$$E'' = \frac{\sigma_0}{\varepsilon_0} \sin \delta \qquad\qquad (20)$$

δ is the phase shift in between represented as

$$\tan \delta = \frac{E''}{E'}$$ (21)

Now for viscoelastic solids the complex modulus can be defined as:

E*=E'+iE'' (22)

For an elastic solid, the stress and the strain is in phase (δ=0), while a viscous liquid exhibits a phase lag between stress and strain of 90°. Viscoelastic polymers show a phase lag between 0 and 90° (see Figure 10).
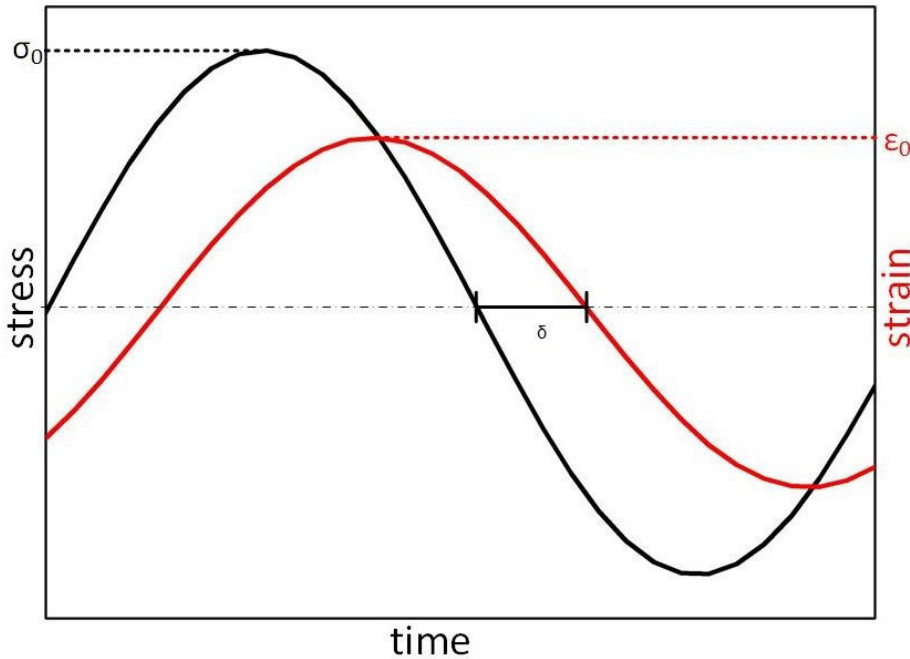
Figure 10: Stress/strain behaviour over time for loading of a viscoelastic solid: a stimulation with maximum σ_0 leads to a maximum strain of ε_0 with a phase lag of δ inspired by [43]

To test the frequency response of viscoelastic polymers, DMA testing can also be applied to NI testing. Here a small oscillation force is added to the quasi-static force with the half amplitude f_0 (Figure 11).

f(t)=$f_0$sin(ωt) (23)

The following displacement oscillation with the half amplitude h_0 exhibits a phase lag θ:

h(t)=$h_0$sin(ωt+θ) (24)

Figure 11: Dynamic NI: a small oscillation force is added to a quasi-static force f_0 (a) and a model of the instrument as Kelvin element coupled with sample (b) inspired by [37].
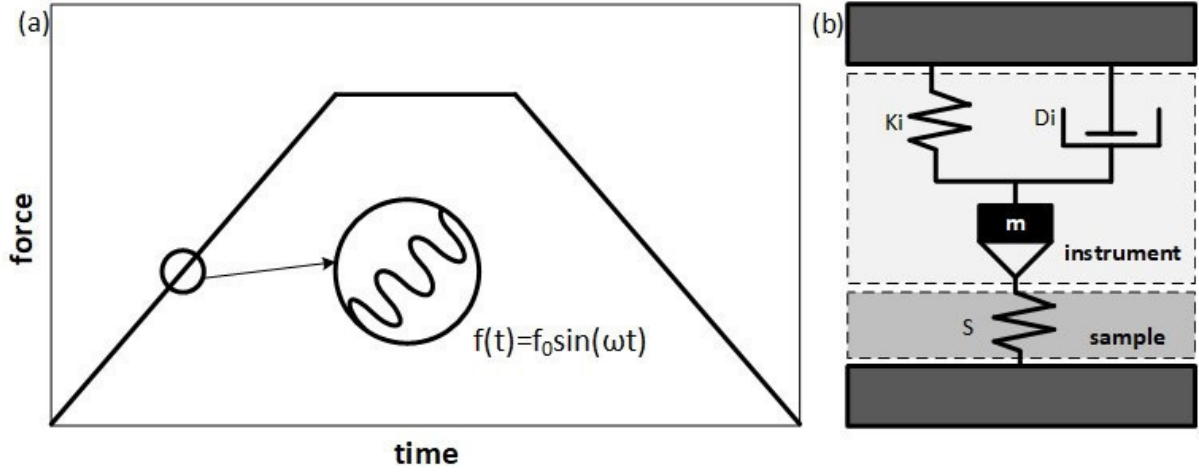
With the assumption of small oscillation amplitudes to stay in the regime of linear elasticity, the sample instrument interactions are modelled according to Figure 11b with the instrument as a Kelvin element coupled with a purely elastic sample. Now, the sample stiffness S_s can be calculated using

$$S_s = \frac{f_0}{h_0} \cos\theta + m\omega^2 - K_i \qquad (25)$$

The damping is calculated with

$$D = \frac{1}{\omega}\frac{f_0}{h_0} \sin\theta - D_i \qquad (26)$$

The machine parameters K_i, D_i and m are determined by dynamic calibration. The stiffness and damping equations can be solved analytically and result in E, H, E' and E'' as a function of indentation depth.

IV.   Influencing factors on NI of polymers

Load and penetration depth are measured directly during loading and unloading of the indenter. The contact area is then calculated with the help of the calibration curve to furthermore calculate the elastic modulus and the hardness. During this procedure, various issues can influence the measurement. An offset in the indentation depth data leads to errors in the result as well as changes in environmental conditions during the measurement. There are also material-related issues to be discussed like indentation size effect or pile-up and sink-in. Polymers show time-dependency and can therefore exhibit nose-building. In the following section, the most important influencing factors for NI polymer testing are described:

h.   Thermal Drift

Holding constant force on a specimen leads to creep of the specimen itself, meaning the indentation depth is rising during holding a constant force.

Another reason for a rising indentation depth during constant load is the thermal drift, where the instrument itself changes its dimensions because of environmental conditions and thermal expansion of various instrument components. To account for thermal drift a constant force segment at low force is introduced at the end of the unloading phase, which allows the calculation of a drift correction factor. This method provides fairly reliable values because the material is less likely to creep especially when using spherical indenters [24]. Another solution to deal with thermal drift is to install a reference ball next to the indenter tip, which is monitoring the influence of thermal drift on the expansion/shrinkage of the sample surface. In reference [39] extreme long indentation creep is studied on polymer samples with an ultra-stable NI with a mounted reference ball. Here the total drift rate for

a 20 h creep measurement is only 0.3 pm/s. Ref. [21] shows a study on metal samples about the effects of creep and thermal drift on modulus results in NI. The thermal drift has only little effect when t_h, the time from the start of the test to the beginning of the unloading equals following condition:

$$t_h \approx \frac{S}{|\dot{F}|} h_c \tag{27}$$

with $\dot{F}$ the unloading rate and S the contact stiffness.

i. Sample surface detection

In an ideal case, the NI device measures the indentation depth starting at the point when the tip touches the surface of the sample. The tip has to contact the sample before starting the measurement. For this purpose, a contact force has to be specified by the user, which is depending on the actual characterization force. Even a small contact load leads to a small indentation (h_i) of the indenter before the contact force can be reached. This results in a biased indentation depth and influences the modulus and hardness calculation. To obtain valid values for hardness and elastic modulus, h_i should be added to all measured displacements. For spherical indentation, h_i can be determined by fitting the elastic response relationship between load and indention depth starting from contact force. The fit can then be extrapolated for smaller forces to get h_i. [24]

j. Machine Compliance

The NI testing device registers the depth of penetration as well as any other displacements coming from deflections of the instrument when performing indentation tests, whereas the additional displacements are dependent on reaction forces from loading. In general, the machine compliance C_m is defined as the deflection of the instrument divided by the load. The unloading stiffness dF/dh is calculated from the first part of the unloading of the load penetration curve.

dF/dh is a superposition of responses from the specimen with stiffness S and the indentation device with the compliance C_m. C_m includes the compliance from different device components as from load frame, the indenter shaft and specimen mounting.

$$\frac{dh}{dF} = \frac{1}{S} + C_m \tag{28}$$

Using a Berkovich indenter with the area function A=24.5 h_c^2 and the relation $E^* = \frac{1}{2} S \frac{\sqrt{\pi}}{\sqrt{A}}$ leads to:

$$\frac{dh}{dF} = \sqrt{\frac{\pi}{24.5}} \frac{1}{2E^*} \frac{1}{h_c} + C_m \tag{29}$$

A spherical indenter with A=2πRh_c provides:

$$\frac{dh}{dF} = \left[\frac{1}{2E^* R^{1/2}}\right] \frac{1}{h_c^{1/2}} + C_m \tag{30}$$

A common method to obtain C_m is to plot dh/dF against $1/h_c^{1/2}$ for a spherical indenter or $1/h_c$ for a Berkovich indenter (see Figure 12). The data should be obtained from the elastic unloading of an elastic-plastic indentation at different loads. The resulting plot should be linear with a slope proportional to $1/E^*$. The intercept with the y-axis represents the machine compliance C_m (see Figure 12). Experiments show, that larger errors appear for lower indentation depths, affecting the fitted line to a higher extent. It is common sense, that initial data points are excluded from the linear regression or a weighted regression is used for the fit. [24]

Another approach to calibrate the NI device for C_m is done by Doerner and Nix [17] on fused silica. Here, a systematic analysis is introduced to identify probe tip imperfections or surface properties of the fused silica from very small indentations. The analysis provides a correlation between F_0, the load before the unloading and $C_t F_0$ with C_t as the total measured unloading compliance obtained from a semi-infinite homogeneous specimen. C_t is given by

$$C_t = C_p + C_m \tag{31}$$

with C_p, a compliance term related to specimen and indenter properties, expressed as $C_p = \frac{1}{E_{eff} A^{1/2}}$

15

Then C_t can be represented as

$$C_t = \frac{1}{E_{eff}A^{1/2}} + C_m \qquad (32)$$

C_m can be isolated as the y-axis intercept of a plot of C_t as a function of $A^{-1/2}$ for a series of indents over a range of loads. The data forms a straight line with the slope $1/E_{eff}$ and is called DN plot after its founders Doerner and Nix [17]. If this DN plot does not result in a straight line an anomalous experimental progress is assumed and the experiment should be discarded.
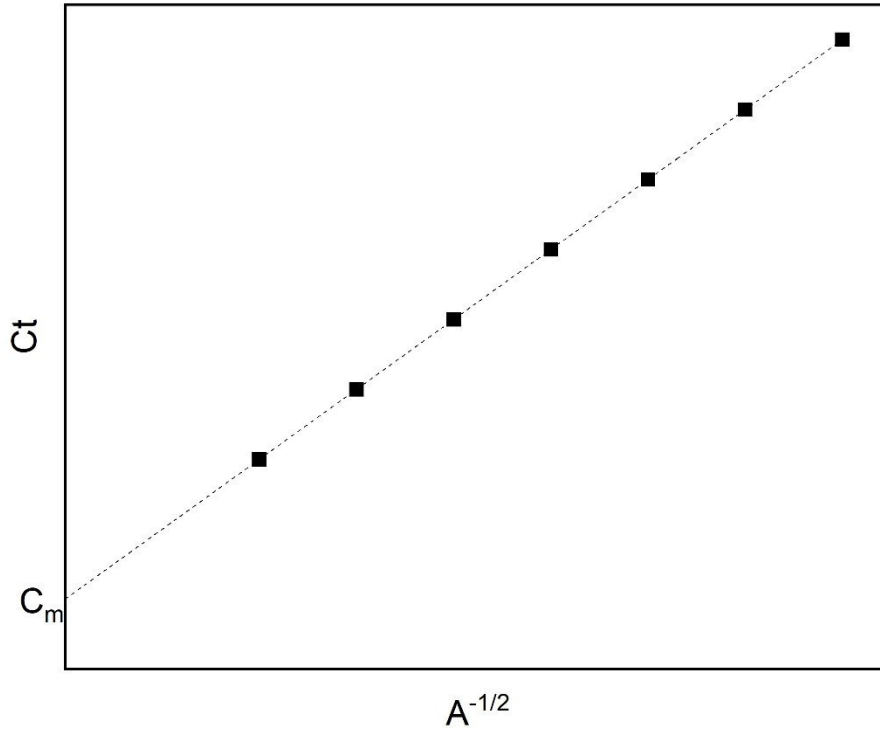

Figure 12: Machine compliance detection: sketch of a C_t against $A^{-1/2}$ plot, C_m is the intersection with the y axis inspired by [64].

In the experimental routine, C_m is then subtracted from experimental values of dh/dF before calculating E according to

h' =h-C_mF $\qquad (33)$

k. Indentation Size Effect (ISE)

Indentation into a homogeneous and isotropic material usually leads to an indentation depth-independent hardness. In some cases, depth-dependent hardness can be found, like in the presence of a thin oxide layer, for different material properties of surface and bulk material or in the presence of residual stresses from sample preparation or polishing. Also, uncertainties arising from area function calculation in the calibration process or simple frictions between the sample and indenter tip lead to depth dependencies [44]. Another reason for depth dependency can be the so-called indentation size effect (ISE).

For crystalline materials, Nix and Gao introduced an explanatory theory dealing with geometrically necessary dislocations [51]. Dislocations in a crystal form either statistically from deformation or due to the geometry of the indenter tip as so-called geometrically necessary dislocations when the material is deformed during indentation. The density of geometrical dislocations ρ_g in the plastically deformed crystalline material is given by

$$\rho_g = \frac{3}{2bh}\tan^2\theta \qquad (34)$$

16

with the Burgers vector b, the opening angle of the indenter tip θ and the indentation depth h. This indicates that a smaller indentation depth leads to a higher density of geometrical dislocations, thus to higher hardness for a smaller indentation depth. This effect is called ISE. The theory about geometrically necessary dislocations is built upon the presence of dislocations as a source within a crystalline material and applies for plastic deformation.

Size dependent deformation has also been investigated in polymers but it is still discussed differently in literature. The deformation mechanisms of polymers on the microscale differ from metals, as polymers bond between atoms and molecules. There is no structural long-range order for polymers, as it exists for crystalline solids like metals and therefore the theory with the geometrically necessary dislocations cannot be applied. There are reports about the existence of ISE when measuring polymers by NI, but the explanations considering microstructure and morphology of polymers are limited.

In [71], a hypothesis for ISE in amorphous polymers has been developed. The basis of this theory are so called shear transformation zones, which are assumed to be plasticity carriers in amorphous polymers [70]. They are localized atomic or molecular deformation zones, introduced by shear [70]. ISE are mostly determined by the size of the shear transformations. At larger scales, the flow units are statistically distributed and influence the plastic deformation uniformly. In Ref. [71], the probability function of finding shear transformations explains the ISE of amorphous polymers like PMMA. For a small indentation depth, the probability of finding a single shear transformation is low, hence the stress level is not big enough to trigger the formation of discrete shear transformations. Instead, the highly stressed volume beneath the indenter undergoes plastic deformation which causes higher hardness. For larger indentation depth, the probability of finding a shear transformation zone, that can undergo plastic deformation rises. When the indentation depth is high enough, deformation is mainly directed by the formation of shear transition zones, which can plastically deform.

l. Surface Roughness

Surface roughness is a very important issue for NI because for the calculation of elastic modulus and hardness evaluation, the evaluation of the contact area is crucible, which is a function of indentation depth. Imperfections from roughness lead to wrong indentation depths and therefore misleading values for contact area, elastic modulus and hardness (Figure 13). [7]
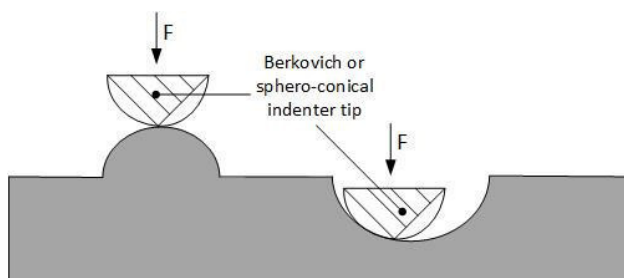

Figure 13: Sketch of the contact area between NI tip (Berkovich -striped, spherical -white) on a hill or in a hole- the contact area is dependent on surface roughness.

Basically, a rough surface can be determined as a surface height exhibiting a non-zero variance related to the mean height [77]. As per the definition, no real object can be perfectly smooth. The measured surface roughness depends very much on the investigated area of a sample, as also on the resolution of the instrument used. The vertical or height resolution identifies the smallest height variation that the instrument can detect. Results of surface roughness measurements are only valid down to the machine resolution.

When classifying surfaces in terms of their statistical properties, two categories can be identified: random and deterministic rough surfaces. A deterministic rough surface can be described by a deterministic function of the surface position. In contrast to that, a randomly rough surface cannot be

17

described by a deterministic function as there is no long-range order but can be outlined by a random field. Most surfaces investigated within this work by NI are randomly rough surfaces. If a randomly rough surface features fractal behaviour, where the roughness scales with the measurement area, the surface is called self-similar (Figure 14). In the special case of the same length scale in all dimensions, it is a cauliflower structure.
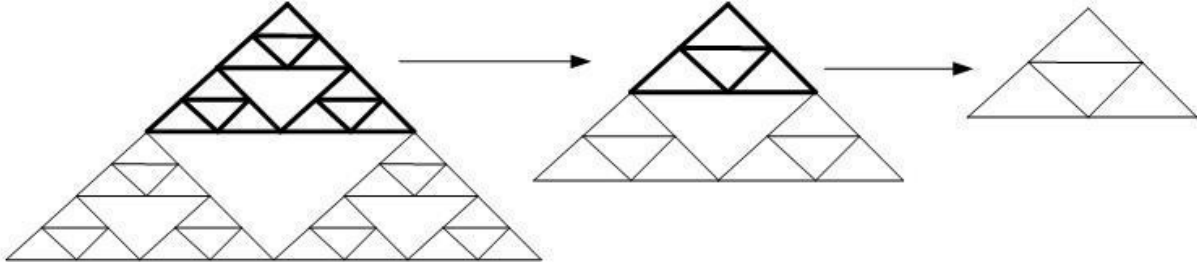

Figure 14: Sketch of a self-similar-fractal object. The Sierpinski triangle contains smaller triangles. The subunits are infinitely repeatable and characterize a self-similar fractal surface.

In the case of a self-affine fractal surface (Figure 15), the z-scale fluctuations are much smaller than the lateral dimensions. Self-affine fractal surfaces can also exhibit a cut-off with self-affine behaviour on the short range and smooth behaviour on a long-length scale.
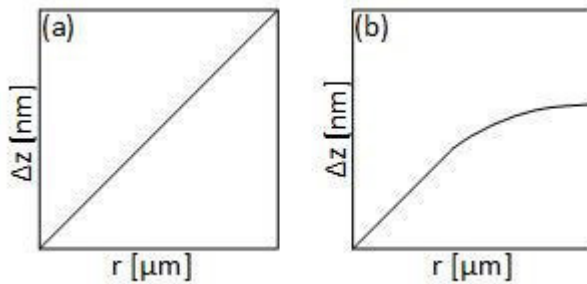

Figure 15: (a) Self-affine fractal surface: z-scale fluctuations are smaller than lateral fluctuations (b) Self affine fractal surface with cut-off: self-affine behaviour on short length scale, smooth on a long length scale inspired by [77].

A main characteristic of the randomly rough surface is the height-height distribution function. For surfaces on the nanoscale, it is important to identify the individual surface structures and to determine the distribution function size, shape and structure of the separation [65]. Given the line profile with distance x of the surface roughness the 1D height-height correlation function is given as:

$$C(x) = \langle [z(x_0 + x) - \langle z \rangle][z(x_0 - \langle z \rangle)] \rangle \tag{35}$$

with $\langle \ \rangle$ for averaging over all values. For samples exhibiting a self-affine fractal behaviour on a short-length scale and smoothness on the long scale, the height-height correlation length can be rewritten as

$$C(x) = \sigma^2 exp\left(-\frac{|x|}{\xi}\right)^{2\alpha} \tag{36}$$

The characters α, ξ and σ can be used to characterize the surface in terms of roughness.

Ref. [42] found that surface roughness influences significantly NI hardness and elastic modulus of single-crystal copper thin films. To decrease the influence of surface roughness on indentation results, the chosen indentation depth should be significantly larger than the surface roughness. In [42], it is also pointed out, that materials usually exhibit surfaces with random morphology with the influence of a randomly rough surface to NI experiments still being under research.

m. Pile-up and sink-in

Plastic deformation during indentation will either lead to pile-up or sink-in. Pile-up means an upward deformation of the specimen (Figure 16a) and will lead to a higher contact depth h_c and thus to an underestimation of the elastic modulus. Sink-in means that the surface of a sample moves inwardly and downwardly underneath the indenter tip (Figure 16b). The contact depth h_c is smaller than the maximum indentation depth h_{max} which leads to an underestimation of the contact area and thus to an overestimation of the elastic modulus. [20]
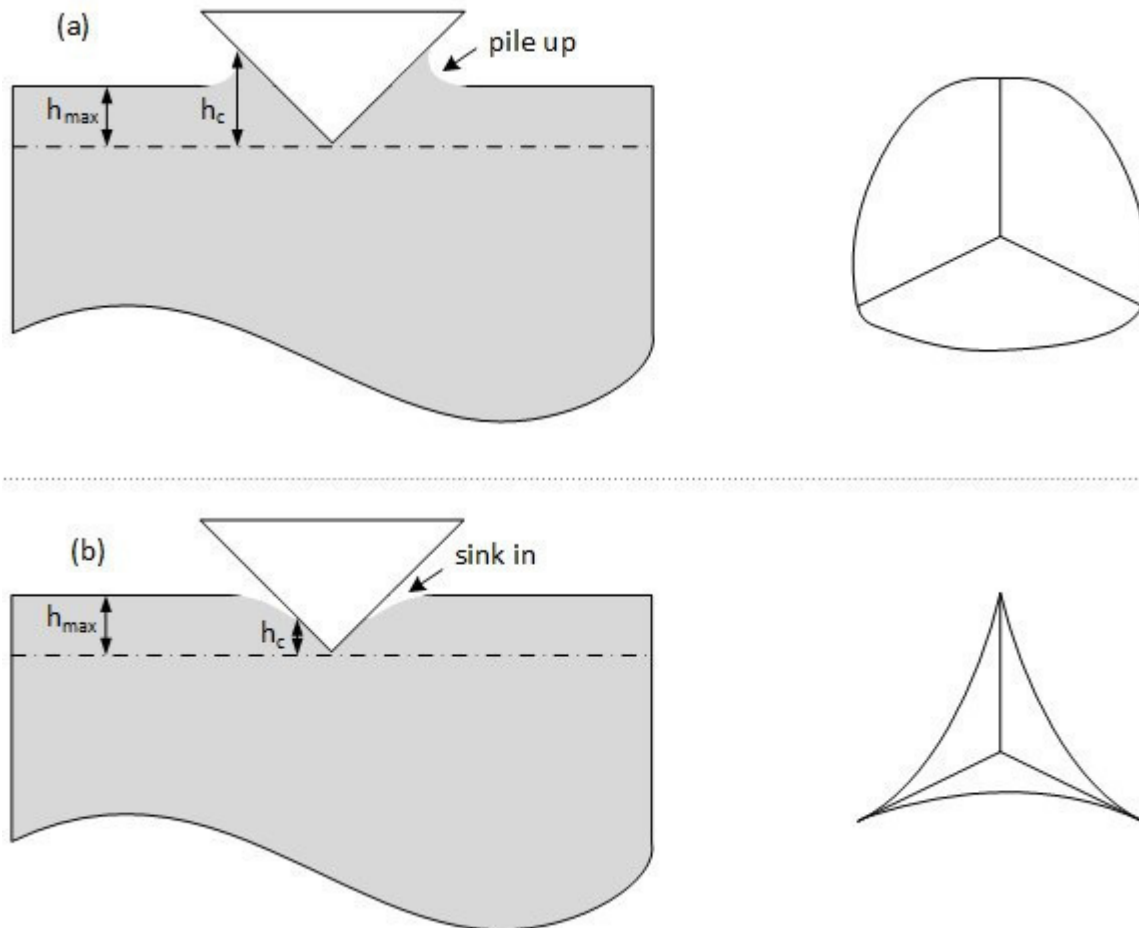

Figure 16: Sketch of pile up (a) and sink in (b) of NI with Berkovich Indenter tip: sketch of the indentation (left) and residual imprints (right) inspired by [23].

The time-dependent behaviour of polymers also influences the piling-up and/or the sinking-in [66]. [34] investigated the effects of pile-up on polymer matrix NI by determining the corrected contact area from Scanning Probe Microscopy (SPM) measurements. On the one hand, the corrected contact area was defined directly from the scan of the residual impression of the indentation and on the other hand it was possible to correct the contact depth h_c by directly measuring the pile-up and correcting the contact area with the calibration function. Both of these methods were found to lower the overestimated elastic modulus, where the method subtracting the pile-up heights delivers more accurate results. The depth of the remaining impression gained by SPM scans is much lower than the depth from the load-displacement curve at approximated zero loads which is seen to be evidence of viscoelastic recovery of the polymer after removing the indenter load. This makes the direct measurement of the imprint less meaningful. Elastic and viscoelastic recovery also leads to an incorrect measurement of the residual pile-up and will result in an incorrect calculation of the elastic modulus. To the author's knowledge, there is no literature yet on how to circumvent the occurrence of pile-up or sink-in when indenting polymers. [34] suggests to use of in-situ NI where pile-up at the state of

maximum load could be investigated as well as viscoelastic and elastic surface recovery. To the author's knowledge experimental work on this is still open.

Pile-up or sink-in does not only depend on material parameters. Also, factors like loading rate and amplitude, indenter shape and radius and underlying substrate [48] are influencing this behaviour. [48] demonstrates that a harder substrate is influencing pile-up of polymers significantly and softer materials like polymers with low H/E ratio exhibit less pile-up than harder materials.

V.   Comparison of NI results with macroscopically tested mechanical properties

Comparison of modulus and hardness data gained by Nanoindentation to conventional macroscopic tests is quite challenging. Errors such as instrument uncertainty and inaccuracy of indenter tip calibration influence data gained by NI. Also, material inhomogeneities, tip imperfections or roughness of the tested sample influence the measurement results. However, also data from macroscopic tests show measurement imprecisions.

Comparing NI with the most common mechanical testing method, the uniaxial tensile test, important differences concerning testing geometry and the principle of measurement have to be mentioned. First of all, the tested volume for a NI test, which is in the µm regime, is much smaller compared to the tensile test in the cm regime. Furthermore, the tested volume is continuously changing for NI, whereas it stays constant for the tensile test. For NI, the stresses and strains contributed from the tip are inhomogeneously distributed among the sample, which is no issue for the tensile test. Also, the direction of the force progresses radially for NI and unidirectionally for tensile testing. [30] compared results from NI, AFM-NI and tensile test, where a slight overestimation of moduli obtained with the tensile test was found.

Comparing dynamic NI to macroscopic Dynamic Mechanical Analysis (DMA) shows corresponding values for E' in many publications [35–37, 52, 72]. It is assumed that both methods work in the linear viscoelastic regime with a material response in the elastic-viscoelastic regime.

PART II: COLLECTION OF THE PAPER, SUMMARY, CONCLUSION AND OUTLOOK

1. COLLECTION OF THE PAPERS

I. Paper 1: Comprehensive investigation of viscoelastic properties of PMMA by NI

Petra Christöf[a], Caterina Czibula[b,d], Michael Berer[a], Gernot Oreski[a], Christian Teichert[b], Gerald Pinter[c]

[a] Polymer Competence Center Leoben, Roseggerstrasse 12, 8700, Leoben, Austria
[b] Institute of Physics, Montanuniversitaet Leoben, Franz- Josef-Str. 18, 8700, Leoben, Austria
[c] Chair of Materials Science and Testing of Polymers, Montanuniversitaet Leoben, Otto Glöckl-Straße 2, 8700, Leoben, Austria
[d] Christian Doppler Laboratory for Fiber Swelling, Graz University of Technology, Infeldgasse 23, 8010, Graz, Austria
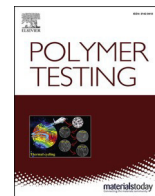
Petra Christöfl authorship contribution:

Conceptualization: definition of the goals of the scientific work, selection of the used methods

Methodology: design of experiments

Investigation: implementation of NI measurements including evaluation

Writing: original draft

POLYMER
TESTING

materialstoday

Check for
updates

Comprehensive investigation of the viscoelastic properties of PMMA by nanoindentation

Petra Christöfl [a,*], Caterina Czibula [b,d], Michael Berer [a], Gernot Oreski [a], Christian Teichert [b], Gerald Pinter [c]

[a] *Polymer Competence Center Leoben, Roseggerstrasse 12, 8700, Leoben, Austria*
[b] *Institute of Physics, Montanuniversitaet Leoben, Franz- Josef-Str. 18, 8700, Leoben, Austria*
[c] *Chair of Materials Science and Testing of Polymers, Montanuniversitaet Leoben, Otto Glöckl-Straße 2, 8700, Leoben, Austria*
[d] *Christian Doppler Laboratory for Fiber Swelling, Graz University of Technology, Infeldgasse 23, 8010, Graz, Austria*

ARTICLE INFO

ABSTRACT

Instrumented nanoindentation (NI) was used to examine the viscoelastic properties of poly(methyl methacrylate) (PMMA) as an amorphous polymer model. An evaluation combining adhesive contact and empiric spring–dashpot models has been applied to obtain the instantaneous elastic modulus E_0 and the infinitely elastic modulus E_∞ from nanoindentation creep curves. The value of E_0 has been compared to moduli obtained with atomic force microscopy-based nanoindentation (AFM-NI) and compression tests. Furthermore, the elastic modulus has been evaluated by the method introduced by Oliver and Pharr (O&P) for the NI and AFM-NI results. Comparison of the elastic modulus E_0 from the creep measurements of NI and AFM-NI to compression tests reveals good agreement of the results. However, only the O&P based AFM-NI results yield to lower values.

1. Introduction

Within the last two decades, nanoindentation (NI) has become a standard depth-sensing technique for testing local mechanical properties of materials. Here, the force and displacement of an indenter is continuously controlled over time. The currently most used Oliver and Pharr [24] (O&P) method for determining mechanical properties from NI tests was originally developed for hard, linear elastic and isotropic materials, based on the Hertzian theory [15] with frictionless and non-conforming surfaces.

The O&P method is mainly used to probe metals [35,38], although there exist also some reports to test polymers [20,33] using this method. In contrast to metals, polymers exhibit viscoelasticity at ambient conditions. If a linear elastic solid is loaded with a constant strain rate, the stress-strain behavior is described by a straight line with the slope E, the elastic modulus. In contrast to that, if a linear viscoelastic material is loaded with a constant strain rate, the stress-strain behavior is non-linear, because it is time-dependent. This means that a viscoelastic material will exhibit different stress-strain curves for different strain rates. For viscoelastic materials, a step-like strain or step-like stress in time are used to separate the influence of time from non-linearity. If the

stress is kept constant at a certain level, strain increases with time, which is called creep [19].

There are multiple limitations for the O&P method for NI of viscoelastic materials like polymers [1,33]. Viscoelastic creep occurs during loading, holding and also during the unloading phase of NI testing. Due to creep behavior during the unloading, the fit of the unloading curve is not sufficient. Prolonged holding segments at maximum load to reach a saturation can partly overcome this problem [5,11]. Another attempt is to establish a correction factor for the slope of the unloading curve of viscoelastic materials [10,23,29] minimizing the creep effects of the time dependent displacement to the elastic modulus. Nonetheless, in all these modifications of the O&P method, the viscoelastic behavior of the material is still neglected and, therefore has been not measured so far.

Standard material models for linear viscoelasticity can be used to model the viscoelastic response of a polymer from creep experiments obtained by depth-sensing methods like NI or atomic force microscopy (AFM) based nanoindentation [13]. By combining linear elastic Hookean springs and Newtonian viscous dashpots, one can describe the elastic response as well as the viscous response of the material [19]. Since the indentation depth for the presented NI experiments is shallow and the radius of the indenter's tip is rather large, the strain is low and it

can be assumed that the deformation is linear viscoelastic [31].

In literature, many examples of investigations combining NI creep measurements with viscoelastic modelling can be found for polymers. One experimental procedure uses a ramp-and-hold technique [25–27] to investigate creep of viscoelastic material with a spherical indenter. Here, several load and hold phases are arranged in series. The creep data are evaluated with a standard linear solid (SLS) model, combining a single spring parallel to a spring and dashpot in series, a so-called Maxwell element (see also Fig. 4). With this experimental approach, it is possible to investigate the load level independency, because the creep response is investigated for different loads and depths within one experiment.

In another approach [4], a three-element material model with a spring in series with a parallel spring and dashpot is applied to investigate creep data using a flat punch indenter for bulk polystyrene (PS). For poly(methyl methacrylate) (PMMA) [39], a model combining a spring and dashpot in parallel which are in series with a spring has been applied to model creep data that has been measured with a sharp indenter probe. Here, the obtained elastic modulus agreed well with the manufacturer's data for PMMA. The suitability of the assumption of linear viscoelasticity in NI [32] has been studied by creep compliance after a step load for epoxy, PMMA and two poly(dimethyl siloxane) (PDMS) elastomers. Variations of the used indenter type have been investigated as well for amorphous (glassy) polymers, semi-crystalline polymers and thermosets [31]. Creep experiments have been performed to study the applicability of linear viscoelasticity with a sharp Berkovich and conical indenters. The results indicate, that these indenters cannot be used for indentation creep experiments, because they do not induce a linear viscoelastic response but show non-linear behavior. Materials with time dependent behavior act linear elastic below a material dependent elastic strain of 1–2%. Therefore stress (strain) induced by NI can be decreased by lowering the force or by increasing the contact area between the indenter and the polymer. Also the employment of a large spherical indenter – causing maximum strain which is smaller than the material-dependent elastic strain limit – is recommended [16]. Additional to these analytical methods, a numerical solution has been derived for a load dependency for poly(vinyl acetate) (PVAc) and PMMA [17]. Furthermore, a numerically approach has been successfully compared to dynamic mechanical analysis (DMA) creep tests for a polyimide (PI) thin film [36].

For the modelling of the contact between a hard indenter probe and a soft polymer during the indentation process, contact mechanics theory derived by Hertz [15] is commonly applied due to its simplicity. Here, Hertz derived a dependency for the non-adhesive elastic contact between a sphere and an elastic half-space. When adhesive forces play an important role [28], the use of the Hertz theory is limited. This was investigated for AFM based nanoindentation (AFM-NI) experiments on PMMA and polycarbonate surfaces [13]. There, it was found that adhesion effects cannot be neglected and, therefore, adhesive contact mechanics in the form of the Johnson-Kendall-Roberts (JKR) model has been combined with different spring-dashpot models to determine viscoelastic properties from creep curves obtained by AFM-NI. The AFM-NI method has been compared with NI and tensile creep testing. Whereas the results of NI agreed well with the AFM-NI measurements,
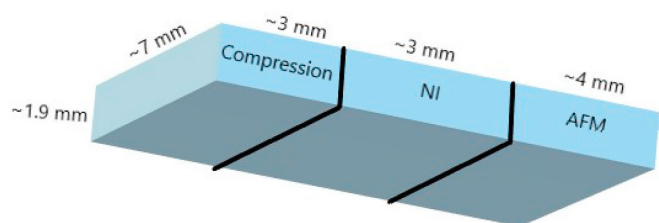

Fig. 1. Sketch of the investigated PMMA sample with marked dimensions for compression test, AFM-NI and NI.

Table 1
Dimensions of the compression test PMMA samples.

sample	length [mm]	width [mm]	height [mm]
1	6.89	2.92	1.91
2	6.81	3.68	1.91
3	6.88	2.94	1.93
4	6.68	3.37	1.93
5	6.89	2.91	1.91

the viscoelastic behavior obtained by tensile creep testing differed significantly. Furthermore, PMMA has been investigated with AFM before [9,14,30,40] and in general, AFM indentation-based studies are commonly used for a wide range of polymers [3].

In general, most experimental studies investigating creep phenomena for thermoplastic polymers with NI focused on variations in load protocols and indenter geometries. In literature, a comparison between results for the elastic modulus of thermoplastics obtained with the O&P method and viscoelastic creep experiments is scarcely mentioned. Furthermore, validation and comparison of results obtained from NI with other methods is rarely realized.

The aim of this study is to develop a method to obtain the elastic modulus of an amorphous thermoplastic polymer by NI. For this purpose PMMA was chosen, because it is isotropic, well processable to provide a flat surface and its glass transition temperature with 100–110°C is far above room temperature. To validate the applied NI methods, i.e. the O&P method and a creep experiment, the calculated elastic moduli are compared to elastic moduli obtained by AFM-NI and compression tests in contrast to tensile tests used previously. In AFM, the applied loads range from a few nN to hundreds of μN. These are by far smaller than the loads commonly applied in NI, which are in the range of μN to N. AFM-NI has already proven to perform well on PMMA surfaces [13]. Therefore, it is considered as a suitable comparison test method. Compression testing, on the other hand, is a well-established method in polymer testing. Compared to tensile testing, it has the advantage that the deformation process is more similar to NI and AFM-NI. For this reason, it is proposed here as a reference test. To the authors' knowledge there has not been a comparative study between NI, AFM-NI and compression tests for PMMA published so far.

2. Materials and methods

2.1. PMMA samples

To test the following methods, the material poly(methyl metacrylate) (PMMA) produced by McMaster-Carr was selected. The specimen was fabricated by extrusion (see Fig. 1).

For the compression test specimens, sub-samples with dimensions indicating Table 1 were cut out of the previous samples.

2.2. Nanoindentation

2.2.1. Oliver and Pharr method

The analysis of indentation curves is mostly done by the method of Oliver and Pharr as presented in Fig. 2a [24]. The unloading curve of the load penetration curve can be fitted [37] according to equation (2.1), where h_p is the permanent indentation depth, h_c is the contact depth of the indenter with the sample at the maximum force F_{max}, h_{max} is the maximum indentation depth and m is a fitting parameter. The parameters h_p, h_{max} and h_c are illustrated in Fig. 2b.

The contact stiffness S (see Fig. 2a) is the slope of the fit $S = \left(\frac{dF}{dh} \right)_{max}$ for the upper portion of the unloading curve. When $A_p = f(h)$ is the contact area of the indenter tip for a given indentation depth h and β is the geometry factor of the indenter tip, the reduced modulus E_r can be calculated [37] by equation (2.2). E_r is obtained by the slope of the
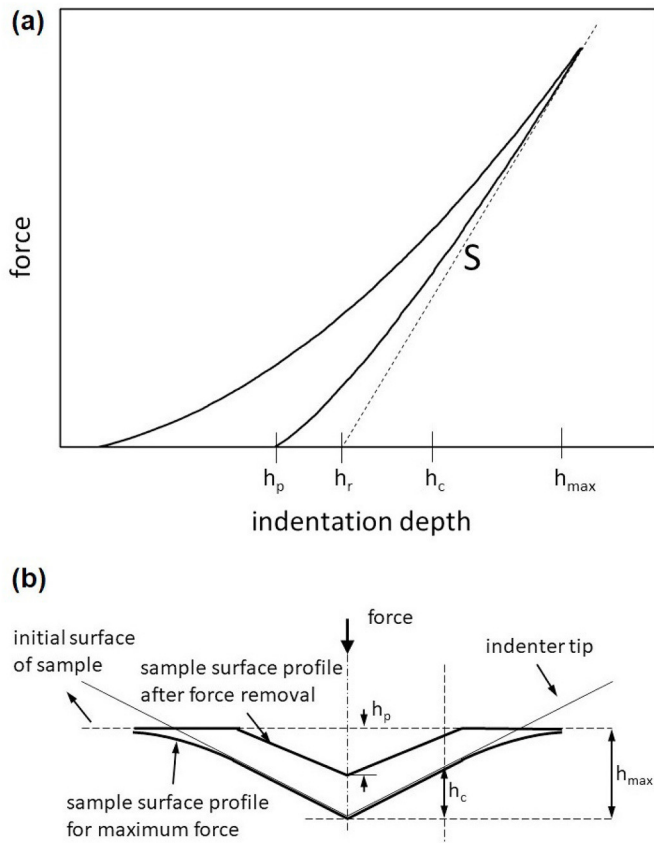
Fig. 2. Schematic indentation load-displacement curve with the slope S of the unloading curve used in the Oliver and Pharr analysis. (b) Cross section of a conical indenter tip.

$$\frac{F}{F_{max}} = \left(\frac{h - h_p}{h_{max} - h_p}\right)^m \tag{2.1}$$

unloading curve assuming that the unloading is purely elastic.

$$E_r = \frac{\pi S}{2\beta\sqrt{A_p(h_c)}} \tag{2.2}$$

Equation (2.3) defines the relationship between the elastic modulus E, the reduced modulus E_r and E_i, the elastic modulus of the indenter ($E_{diamond}$=1141 GPa). ν_i is the Poisson's ratio of the indenter tip with $\nu_{diamond} = 0.07$. For the following experiments we assumed $\nu_s = 0.35$ for PMMA.

$$\frac{1}{E_r} = \frac{(1 - \nu^2)}{E} + \frac{(1 - \nu_i^2)}{E_i} \tag{2.3}$$

For the current work, an Anton Paar *UNHT*[3] Nanoindenter (Anton Paar, Graz, Austria) was employed. The Software "Indentation 8.0.24" (Anton Paar) was used for data recording and evaluation of the data. For practical reasons, the fit of the unloading curve was performed at 75% until 95% of F_{max} of the unloading curve. All tests were performed using an Anton Paar diamond sphero-conical nanoindenter tip (SG-A59) with $\beta = 1$, a tip radius of 0.1 mm and an opening angle of 90°. Tip calibration was performed on a fused silica reference sample from Anton Paar with a thermal drift ≈ 0 $\mu m/N$ [16]. NI tests were operated on one PMMA sample under laboratory conditions of 20°C and 20% humidity in a three-by-three matrix with 100 μm distance between each indent. The loading and unloading of the sample was performed linearly with 40 mN/min and a maximum load of 5 mN, besides the constant force holding phase was 30 s.

2.2.2. Nanoindentation creep measurements

Nine nanoindentation tests were operated under laboratory conditions of 20°C and 20% humidity in a three-by-three matrix with 100 μm distance between each indent. The loading of the sample was performed linearly with 300 mN/min and a maximum load of 5 mN. The constant force holding phase was 300 s. The load schedule as well as the resulting creep curves are presented in Fig. 3.

2.3. Viscoelastic material modelling

Amorphous thermoplastics, such as PMMA, exhibit viscoelastic material properties, which means that the material behaves partly elastic and partly viscous. If the material is deformed mechanically, the elastic part of the behavior invokes a spontaneous and reversible deformation, which can also be described by a spring following Hooke's law $\sigma = E\varepsilon$, provided that the deformation is in the regime of linear elasticity. The viscous part of the deformation is time-dependent and irreversible and can be illustrated by a dashpot with a stress of $\sigma = \eta\frac{d\varepsilon}{dt}$, where η represents the viscosity [19].

Thus, for a viscoelastic material the relationship between stress and strain is time dependent and can be described by spring-dashpot models, where the standard linear solid model (SLS) offers the simplest material model describing the behavior of real solids (see also Fig. 4a). It consists of three elements, a single spring parallel to a so-called Maxwell element which combines a spring and dashpot in series [19]. The differential equation of the SLS is represented in equation (2.4) with E_∞, E_1 and the viscosity $\eta_1 = \tau_1 E_1$ with τ_1, the relaxation time. The dot above the variable is a shorthand for $\frac{d}{dt}$.

$$(E_\infty + E_1)\dot{\varepsilon} + \frac{\varepsilon E_\infty}{\tau_1} - \dot{\sigma} = \frac{\sigma}{\tau_1} \tag{2.4}$$

Applying this viscoelastic material model to experimental data of nanoindentation or AFM creep measurements [13], with indentation dept and force given, the upper and lower bound of the elastic modulus can be calculated in terms of E_∞ and E_0. An infinitely slow deformation $\frac{d\varepsilon}{dt}\rightarrow 0$, results in $\sigma_{dashpot}\rightarrow 0$, because of the relation $\sigma = \eta\frac{d\varepsilon}{dt}$. Consequently, only E_∞ remains, which exhibits the stiffness limit of the material at infinitely slow loading. On the other hand, for an infinitely fast deformation $\frac{d\varepsilon}{dt}\rightarrow\infty$ and therefore $\sigma_{dashpot}\rightarrow\infty$ – meaning that the dashpot remains stiff and only the springs are contributing – the modulus is $E_0 = E_\infty + E_1$.

Furthermore, the differential equation (2.4) is rewritten in terms of the force F(t) and the indentation depth $\delta(t)$ and is combined with JKR contact theory [28], where the average stress under a spherical indenter is given by equation (2.5), with F_{ad} the adhesion force and R the effective radius of the spherical indenter.

$$\sigma_{JKR}(t) = \frac{3}{8}\frac{\tilde{F}(t)}{R\delta(t)}\left(1 - \frac{4}{3}\sqrt{\frac{F_{ad}}{\tilde{F}(t)}}\right)^2 \tag{2.5}$$

$\tilde{F}(t)$ is expressed by $\tilde{F}(t) = F(t) + 2F_{ad} + 2(F_{ad}F(t) + F_{ad}^2)^{\frac{1}{2}}$. With $\sigma = \varepsilon E$, the average strain under the indenter can be calculated by equation (2.6).

$$\varepsilon_{JKR}(t) = \frac{1}{2}\left(\frac{\delta(t)}{R}\right)^{\frac{1}{2}}\left(1 - \frac{4}{3}\sqrt{\frac{F_{ad}}{\tilde{F}(t)}}\right)^{\frac{1}{2}} \tag{2.6}$$

Then equations (2.5) and (2.6) are substituted for σ and ε in equation (2.4), which results in an equation for F and δ. Further information on the calculations for SLS and the more generalized Maxwell model of order 2 (GM2) (see also Fig. 4b) is given in Ref. [13]. The numerical solution of the differential equation is fitted to experimental data according to Refs. [13].
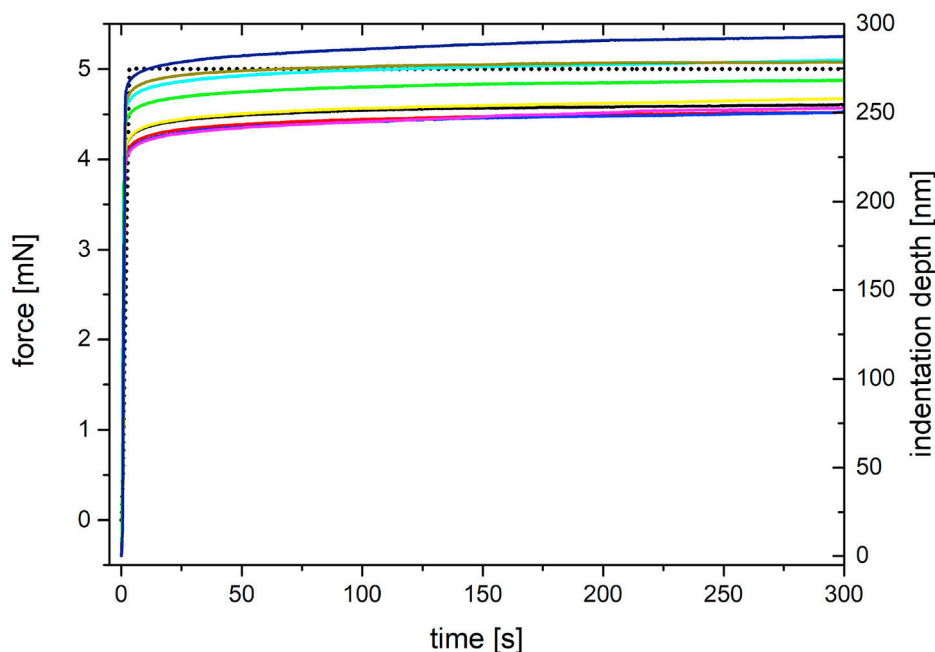
Fig. 3. Load schedule (black dashed curve - left axis) and nine creep curves (colored solid curves - right axis) for NI creep measurements of PMMA.
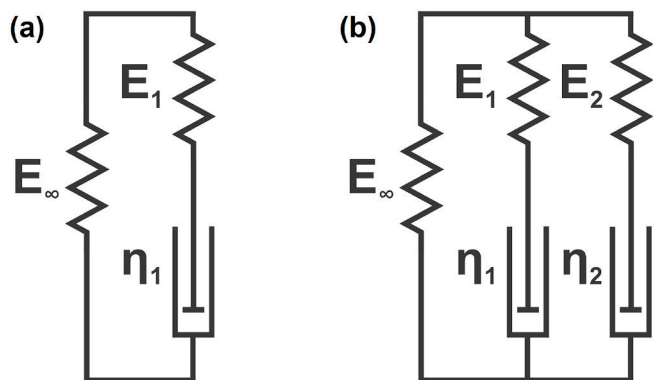

Fig. 4. Linear viscoelastic models. (a) Standard Linear Solid (SLS) model with the three parameters E_∞, E_1 and η_1. (b) Generalized Maxwell Model of order 2 (GM2) with the 5 parameters E_∞, E_1, E_2, η_1 and η_2.

2.4. Atomic force microscopy (AFM)

All AFM-based nanoindentation (AFM-NI) experiments in this work have been acquired with an Asylum Research MFP-3D AFM (Asylum Research, Santa Barbara, CA, USA) at a temperature of 23°C and a relative humidity level of 25%. The instrument is equipped with a closed-loop planar x–y-scanner with a scan range of $85 \times 85\ \mu m^2$ and a z-scanner with a range of about $15\ \mu m$. For the AFM-NI measurements, LRCH40 silicon probes (Team Nanotec, Germany) have been used. The spring constant of the cantilever in use is 56.9 N/m and has been calibrated by performing the thermal sweep method [18]. The thermal Q factor is 653 and the resonance frequency is 346.6 kHz. Since the contact area between tip and sample surface is crucial for mechanical characterization by AFM, the tip geometry of the probes was checked with a TGT01 (NT-MDT, Russia) calibration grid. Utilizing the tip-sample dilation principle [34], it is possible to image the AFM tip by scanning across a grid of sharp spikes. For the hemispherical LRCH40 probes, a tip radius of 245 nm was determined this way. For the measurement of mechanical properties by AFM, the probe needs to get in contact with the surface. To achieve this contact, the AFM tip is approached to the

surface with a velocity of $1\ \mu m/s$ until a so-called trigger point of about 100 nN is reached. From this point onward, a force-indentation curve is recorded [2]. To determine the viscoelastic properties, the load schedule presented in Fig. 5 is applied. Please note that the load schedule deviates only slightly from the one which has been already presented and thoroughly discussed elsewhere [6,13].

The AFM experiment has been done according to the load schedule presented in Fig. 5. First, a small preload is applied to determine the indentation depth due to adhesion. In the second step, the surface is on purpose plastically deformed ($F_{max} = 20\mu N$). For one, this makes it possible to obtain the reduced modulus according to the Oliver and Pharr method [24], and second, the surface roughness is reduced due to the deformation and results in a clearly defined contact area. After a 150 s time of relaxation and staying in contact with the surface at very low forces (about 500 nN), the load is increased again but to a much lower value $(5\mu)N$ and the creep experiment is performed for 300 s. Here, it should be mentioned that this AFM creep method has been developed with the measurement of wood pulp fibers in mind. Apart from
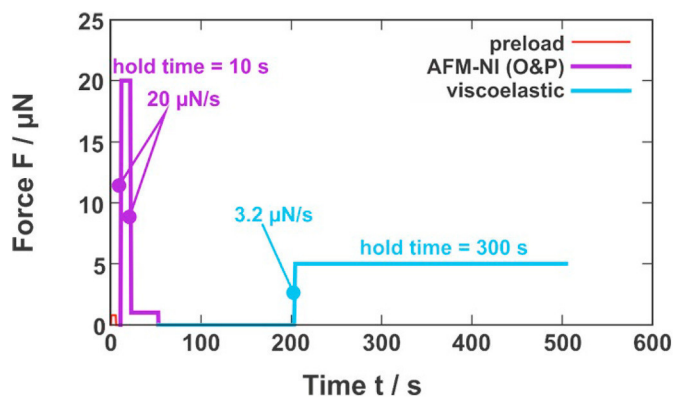

Fig. 5. AFM load schedule consisting of three different parts. After a small preload (red line), the sample surface is deformed plastically with an applied force of 20 μN (violet line). Next, the surface is relaxing for 150 s and then the viscoelastic experiment is performed with an applied force of 5 μN (blue line). (For interpretation of the references to colour in this figure legend, the reader is referred to the Web version of this article.)

anisotropic properties, the surface of the fibers is very rough which is very challenging for providing a proper tip-surface contact [6].

Any offset due to thermal drift is corrected for in the data evaluation. For the Oliver and Pharr evaluation of the AFM data, a 30 s minimal load of 1 μN has been included after the maximum load (20 μN) to correct for drift in the data (see Fig. 5). Furthermore, for the creep experiments, thermal drift has been considered by linearly fitting the last 60 s of the relaxation time and correcting the whole creep curve. Details are described in more detail in Ref. [12,13].

Here, the only difference compared to the load schedule established in Ref. [13] is that the hold time during the viscoelastic load regime is increased from 120 s to 300 s in order to match the NI experiment. The loads and load rates are identical.

The data is afterwards evaluated as described for the NI data but instead of a Standard Linear Solid (SLS) model, a Generalized Maxwell model of order 2 (GM2) has been applied (see Fig. 4).

2.5. Compression test

Compression tests were performed following the standard DIN EN ISO 604–2003 [8] with an Instron 5500 material testing system on 5 PMMA samples with dimensions indicated in Table 1. With a deformation speed of 2 mm/min, a stress strain curve for every sample could be obtained. The starting regime was corrected according to the standard DIN EN ISO 604–2003 [8] and the point of origin was adapted. Afterwards, the modulus was calculated differing to the standard DIN EN ISO 604–2003 [8] at higher strains for maximum slope, because the starting regime was very pronounced.

3. Results and discussion

3.1. NI results for the O&P method and the viscoelastic creep experiments

As already mentioned in the introduction, the commonly used O&P method for determining mechanical properties from the nano-indentation testing was initially developed for hard, linear elastic and isotropic materials. PMMA, however, is a viscoelastic thermoplastic polymer and, therefore, the O&P method should not be the first choice to gain insight on its mechanical properties.

For the investigation of the influence of the viscoelastic behavior of PMMA [1] on the O&P results, two series of NI experiments - only differing in the holding time between the loading and the unloading segment - have been applied. Without holding time, the indentation curve would form a typical nose shape because of creep during unloading [7]. A longer holding time leads to a smaller slope at the beginning of the unloading curve, because the material exhibits less creep at the beginning of the unloading curve. For higher unloading rates, this effect is decreasing. Thus, it is recommended to use a longer holding time to reduce the creep effect by reaching a mechanical equilibrium before unloading. In this work, no difference in the slope with varying holding times has been observed and a holding time of 30 s for the O&P method has been applied. The maximum applied load of 5 mN for all the NI tests in this study is rather low and, therefore, may lead to a lower dependency on holding time. As presented in Fig. 6, nine indents were evaluated with the O&P method (see also section 2.2.1). They result in a modulus of E = (3.3 ± 0.2) GPa and E_r = (3.6 ± 0.2) GPa. (The values are given as mean ± standard deviation.)

For the testing and the characterization of viscoelastic materials, however, it is preferable to apply a step strain or step stress. The response to step strain is stress relaxation, and the response to step stress is creep [19]. It is visible in Fig. 3 that, for a constant force, the indentation depth is increasing with time, i.e. PMMA is exhibiting creep with high reproducibility.

As described in section 2.3, viscoelastic material parameters such as the elastic modulus can be obtained by material modelling. Representative experimental data from the NI measurements is illustrated in
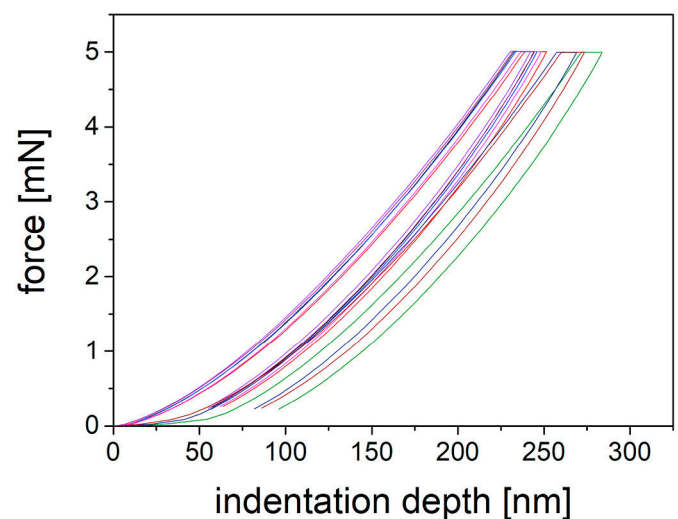

Fig. 6. Nine indentation load displacement curves on PMMA, presented in different colours. (For interpretation of the references to colour in this figure legend, the reader is referred to the Web version of this article.)

Fig. 7 together with the corresponding SLS fit. The viscoelastic fitting parameters are listed in Table 2. Two limits of the elastic modulus E_∞ and E_0 can be determined with the SLS model. The instantaneous modulus E_0 – the elastic modulus at infinitely fast loading – is most commonly used to compare to conventional elastic moduli. Here, E_0=(3.5 ± 0.3) GPa, which is in agreement to the results obtained by the O&P method. The E_∞ describing infinitely slow deformations is (2.5 ± 0.1) GPa, whereas the parameters of the Maxwell element are E_1 = (0.4 ± 0.5) GPa and τ_1 = (0.2 ± 0.1) s.

3.2. Atomic force microscopy

AFM topography scans have been recorded to characterize the roughness of the PMMA surfaces with standard silicon probes (Olympus, Japan) which have a tip radius of under 10 nm. Three independent 20 × 20 μm^2 topography regions have been investigated and their RMS roughness - as a measure for the vertical surface roughness - was calculated to be (9 ± 2) nm. Fig. 8 represents AFM topography scans recorded with the LRCH40 indenter probes before and after indentation. As can be seen in Fig. 8a, the surface is characterized by scratches which are most probably a result of the sample preparation. Since these scratches range from several hundred nm to about 1 μm in width, one can assume that the NI tests using an indenter tip radius of 0.1 mm should not be influenced too much by those surface imperfections. For the AFM indentation probe with a tip radius of 245 nm, on the other hand, an influence of the scratches to the AFM-NI measurements is possible but can be circumvented by carefully selecting measurement positions from the topography images which have areas of low surface roughness, as is indicated in Fig. 8b. It should be noted that the large tip radius of the AFM probe convolutes the surface. However, since the surface is rather smooth, the performance of a dilation with a large radius of an image, which has been recorded with a small tip radius probe, indicated that the effects are only visible for the scratches on the surface. Altogether, the viscoelastic properties of PMMA have been investigated with AFM-NI on three independent regions with all together 23 indents. As has been investigated and reported previously [13], the adhesion force F_{ad} of (264 ± 18) nN is high enough to require the use of adhesive contact mechanics in the form of the JKR model.

The evaluation of the plastic predeformation part of the AFM-NI experiment – as discussed in section 2.4 – according to the O&P method, results in a reduced modulus E_r = (2.1 ± 0.3) GPa. In contrast to the NI tests, the GM2 model resulted in a better fit with an R^2 value of
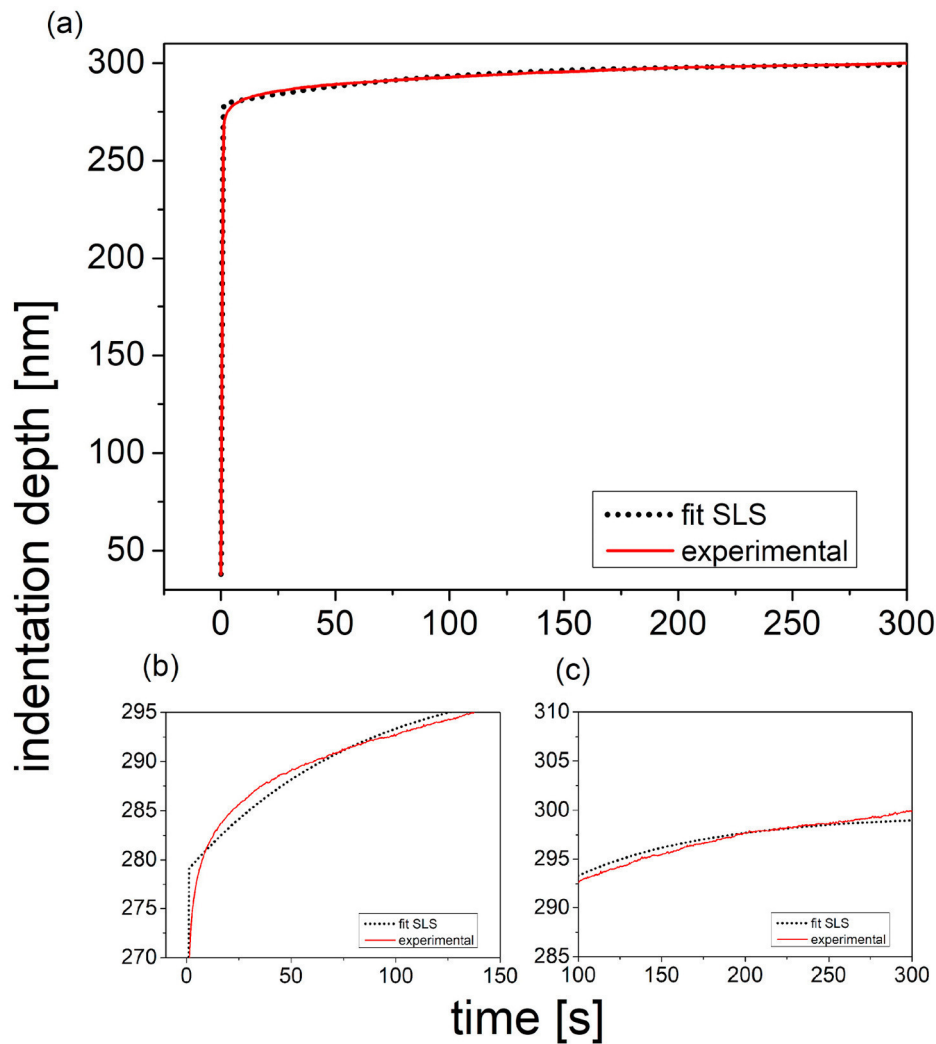
Fig. 7. (a) Representative experimental curve (solid line) obtained by NI with the corresponding SLS model fit (dashed line). The fit quality is indicated by $R^2 = 0.99$. (b), (c) Zoom-in regions of the same curve.

Table 2
Viscoelastic parameters of PMMA measured by Nanoindentation evaluated with the SLS and AFM evaluated with GM2 model; Values are given as mean and standard deviation over 9 indents; AFM-NI is averaged from 3 positions.

Model	Method	$E_\infty [GPa]$	$E_1 [GPa]$	$E_2 [GPa]$	$E_0 [GPa]$	$\tau_1 [s]$	$\tau_2 [s]$
SLS	NI	2.5±0.2	1.1±0.4	–	3.5±0.3	54±17	–
GM2	AFM-NI	1.5±0.2	1.4±0.2	0.5±0.2	3.3±0.2	2.7±0.9	11,0±17

0.99 for the AFM-NI creep experiments. In Fig. 9, a representative experimental curve for PMMA with the corresponding GM2 fit is illustrated. The resulting elastic moduli are $E_\infty = (1.5 \pm 0.1)$ GPa and $E_0 = (3.3 \pm 0.2)$ GPa. For the relaxation behavior, $\tau_1 = (2.7 \pm 0.9)$ s and $\tau_2 = (110 \pm 17)$ s were found (see also Table 2). Thus we have to note that the result for the reduced modulus from the O&P method is much lower than the elastic modulus E_0 obtained by the GM2 model.

3.3. Compression tests

Fig. 10 presents the stress-strain behavior of PMMA samples investigated by compression test. The calculation of the compression modulus following DIN EN ISO 604–2003 [8] yields (3.4 ± 0.2) GPa.

3.4. Comparison and discussion of the results

In Table 2, the results of the viscoelastic parameters are compared for NI obtained with the SLS model and AFM obtained with the GM2 model. Although, fitted with two different models, the E_0 values for NI and AFM-NI are quite comparable.

The values for the NI data calculated with the SLS model seem to match the AFM values calculated with the GM2 model. The E_0, which is an indicator for fast material deformation and mathematically expressed as $E_0 = E_\infty + \sum E_i$, is for NI data calculated with SLS material model (3.5 ± 0.3) GPa. For AFM data calculated with the GM2 material model E_0 is (3.3 ± 0.2) GPa. It is reasonable that AFM and NI need different order fitting routines, because the maximum force for NI is 5 mN, whereas the maximum force for AFM is 5 μN, i.e. three orders of magnitude smaller. As a consequence, the maximum indentation depth for NI with about
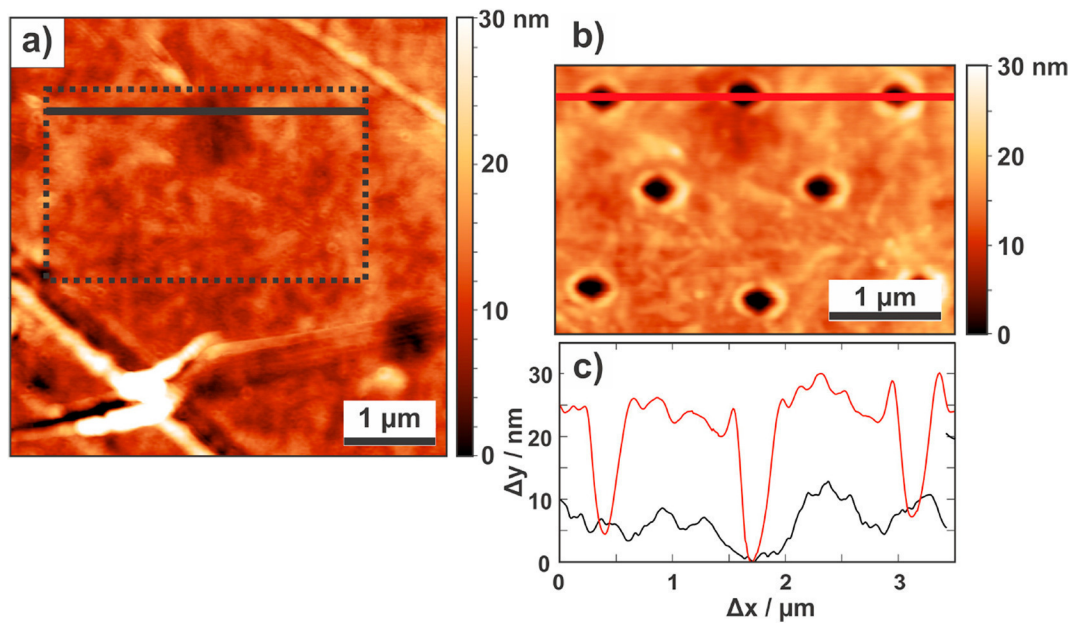
Fig. 8. (a) $5 \times 5 \ \mu m^2$ representative AFM topography image of the PMMA surface. The rectangle indicates a rather smooth topography region which has been used for AFM-NI experiments. In (b) this region is presented after the indentation experiments (approximately 2 h later) exhibiting typical indents. (c) Cross-sections of the scans before and after indentation which are indicated by the black and red line in (a) and (b), respectively. The images have been recorded with the large radius probe. (For interpretation of the references to colour in this figure legend, the reader is referred to the Web version of this article.)
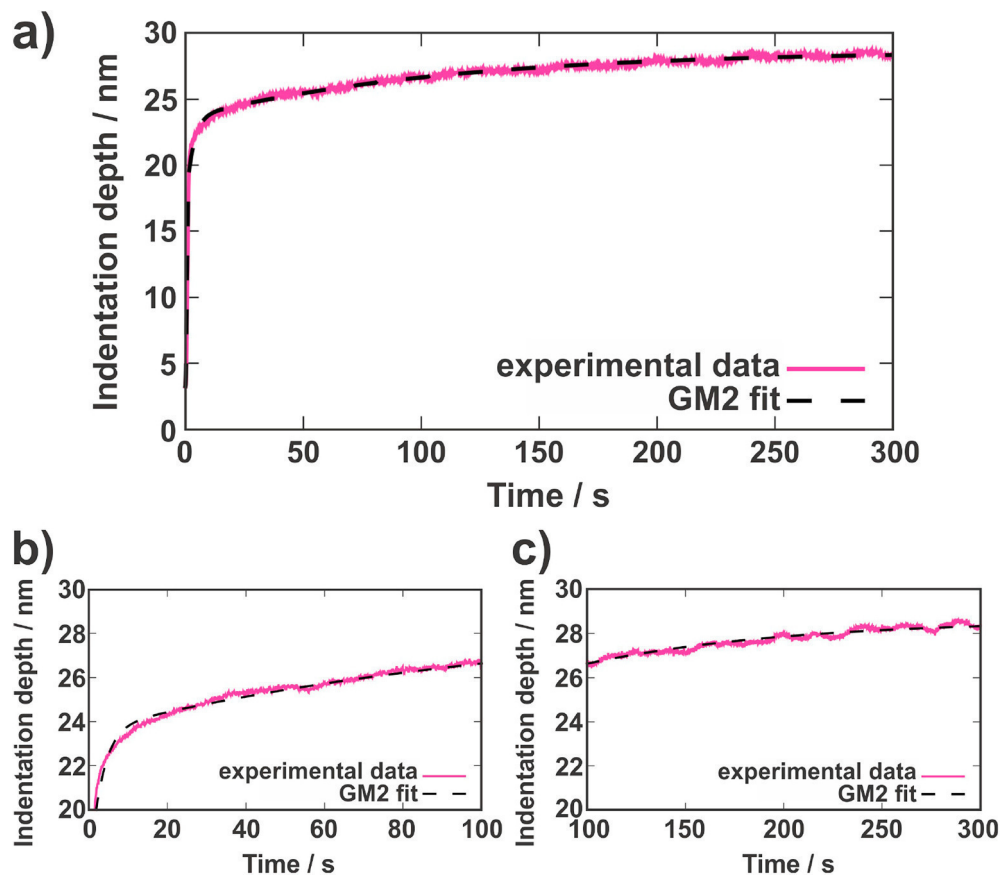

Fig. 9. AFM-NI creep results. (a) Creep curve recorded on PMMA (experimental data) with the corresponding GM2 fit (dashed line). The fit quality is indicated by R^2 = 0.99. (b, c) Zoom-in regions of the same curve.
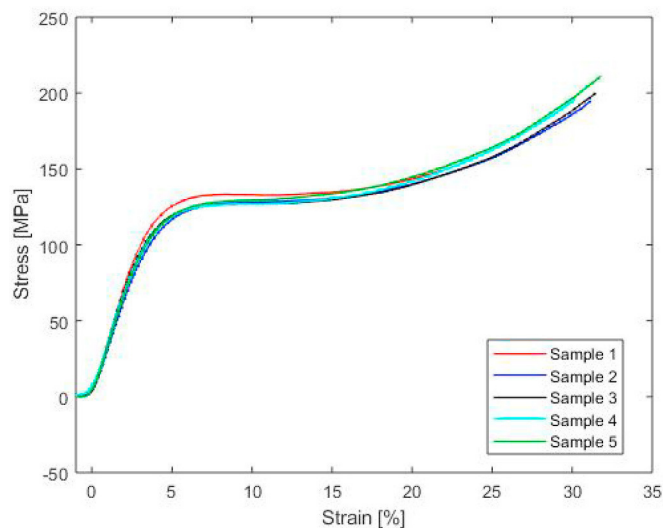
Fig. 10. Results of five compression tests of PMMA.

Fig. 11. Comparison of the elastic modulus of Nanoindentation gained by Oliver and Pharr method, the reduced modulus gained by AFM-NI with the O&P method, the E_0 of AFM and Nanoindentation creep measurements and the compression modulus investigated by compression tests. Numerical data is presented by two parts, a box and a set of whiskers. The box is drawn from the 25% percentile to the 75% percentile. The horizontal line in the middle is the median and the square presents the arithmetical mean. The whiskers are drawn with a 1.5 times length of the box length. Points drawn as crosses are outliners.

250 nm is higher than for AFM with about 30 nm.

The O&P results for both techniques vary with an $E_r = (2.1 \pm 0.3)$ GPa for AFM-NI and $E_r = (3.6 \pm 0.2)$ GPa for NI. The difference is nearly a factor of 2. A reason for the low modulus in AFM-NI could be the lateral movement of the probe during indentation due to the high applied forces. This has already been encountered previously [13].

Furthermore, the tip radius of NI is 0.1 mm in contrast to the AFM tip radius, which is 245 nm, i.e. there is factor of 400 in between. Assuming $F_{ad} = 0$ in eq. (2.6), the induced strain can be estimated with $\varepsilon = 0.17$ for AFM-NI and $\varepsilon = 0.025$ for NI. The larger tip radius induces lower strain to the material, because the increase in contact area with depth is higher. This reduces the creep rates for any force and therefor minimizes the contribution of plasticity to the materials response. Also, lower strain leads to indentation in the linear viscoelastic regime which improves the viscoelastic fit.

The common O&P method for NI yields an elastic modulus of (3.3 ± 0.2) GPa for PMMA, which is the same value as AFM-NI yields for E_0 employing GM2 material modelling. NI modelling with SLS delivers $E_0 = (3.5 \pm 0.3)$ GPa, which is also in the same range. The NI Oliver and Pharr method seems to match with creep tests for PMMA, which is also consistent with the hold time experiment at the beginning of this section, where the initial slope of the unloading curve is not changing significantly.

Compression tests - as an established material testing routine - have been used to validate the results from NI and AFM-NI. Since the method induces compressive stress, it is more appropriate for the comparison to indenting methods than tensile tests [13]. The obtained compression modulus of (3.4 ± 0.2) GPa is also in the same range as the E_0 values obtained by NI and AFM creep measurements. The comparison between NI, AFM and compression test is presented in Fig. 11 in terms of a boxplot.

4. Conclusions

Nanoindentation (NI) using an evaluation routine according to the O&P method has become a useful tool to examine modulus properties of materials. For the special case of viscoelastic materials, the *O&P* method might not be ideal due to influences of creep behavior during the unloading phase of the indentation. The investigation of creep curves gained by NI combined with material modelling indicated to use the occurrence of creep of viscoelastic materials instead of neglecting it. For that purpose, NI creep tests as well as NI O&P measurements were performed on PMMA. To validate the NI results, also AFM-NI and compression tests were performed. Comparing the moduli, it is obvious
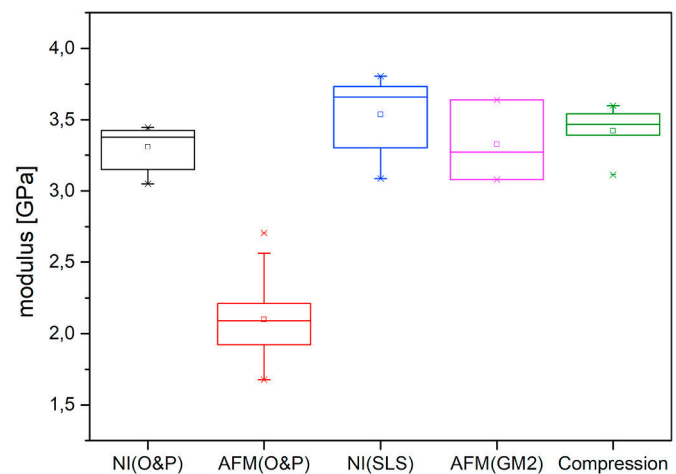
that the results from NI and AFM creep measurements are in the same range than the compression test. The O&P results from NI fits quite well too, only the O&P results obtained by AFM-NI have lower values, therefore, underestimating the elastic modulus.

Future research will focus on the determination of viscoelastic properties of semi-crystalline polymers in contrast to thermoplastics with similar methods as presented here. The influence of crystallinity to the space-resolved moduli will be investigated by AFM and NI and furthermore compared with compression test.

The method presented in this study can be applied in all the fields of research where it is important to determine changes in creep behavior due to material degradation. For instance such a future topic will be the investigation of the degradation of electrical insulating materials of photovoltaic modules, so called backsheets. The investigation of backsheets according to the presented methodology in this study will allow to distinguish viscoelastic properties of degraded in contrast to unexposed backsheets. Furthermore, the influence of degradation effects of photovoltaic backsheets on the creep behavior is of relevance because it predicts the occurrence of cracking [21].

5. Data availability

The raw (processed) data required to reproduce these findings cannot be shared at this time due to technical or time limitations.

CRediT authorship contribution statement

Petra Christöfl: Conceptualization, Methodology, Investigation, Writing - original draft. **Caterina Czibula:** Software, Formal analysis. **Michael Berer:** Validation. **Gernot Oreski:** Resources, Funding acquisition. **Christian Teichert:** Writing - review & editing. **Gerald Pinter:** Supervision.

Declaration of competing interest

The authors declare that they have no known competing financial interests or personal relationships that could have appeared to influence the work reported in this paper.

Acknowledgements

Appendix A. Supplementary data

Supplementary data to this article can be found online at https://doi.org/10.1016/j.polymertesting.2020.106978.

References

[1] B.J. Briscoe, L. Fiori, E. Pelillo, Nanoindentation of polymeric surfaces, J. Appl. Phys. 31 (1998) 2395–2405.

[2] H.J. Butt, B. Cappella, M. Kappl, Force measurements with the atomic force microscope: technique, interpretation and applications, Surf. Sci. Rep. 59 (2005) 1–152, https://doi.org/10.1016/j.surfrep.2005.08.003.

[3] B. Cappella, Mechanical Properties of Polymers Measured through AFM Force-Distance Curves, Springer, Switzerland, 2016, https://doi.org/10.1007/978-3-319-29459-9.

[4] L. Cheng, Z. Xia, W. Yu, L.E. Scriven, W. Gerberich, Flat-punch indentation of viscoelastic material, J. Polym. Sci. B Polym. Phys. 38 (2000) 10–22.

[5] T. Chudoba, F. Richter, Investigation of creep behaviour under load during indentation experiments and its influence on hardness and modulus results, Surf. Coating. Technol. 148 (2001) 191–198.

[6] C. Czibula, C. Ganser, T. Seidlhofer, C. Teichert, U. Hirn, Transverse viscoelastic properties of pulp fibers investigated with an atomic force microscopy method, J. Mater. Sci. 54 (2019) 11448–11461, https://doi.org/10.1007/s10853-019-03707-1.

[7] D. Cakmak, U, T. Schöberl, Z. Major, Nanoindentation of polymers, Meccanica 47 (2012) 707–718, https://doi.org/10.1007/s11012-011-9481-6.

[8] DIN Deutsches Institut für Normung, 12/, Bestimmung von druckeigenschaften, 2003.

[9] Y.H. Ding, X.H. Deng, X. Jiang, P. Zhang, J.R. Yin, Y. Jiang, Nanoscale mechanical characterization of PMMA by AFM nanoindentation: a theoretical study on time-dependent viscoelastic recovery, Journal of Material science 48 (2013) 3479–3485, https://doi.org/10.1007/s10853-013-7138-7.

[10] G. Feng, A. Ngan, The effects of creep on elastic modulus measurement using nanoindentation, MRS Proceedings 649 (2000) 1–6, https://doi.org/10.1557/PROC-649-Q7.1.

[11] G. Feng, A.H.W. Ngan, Effects of creep and thermal drift on modulus measurement using depth-sensing indentation, J. Mater. Res. 17 (2002) 660–668, https://doi.org/10.1557/JMR.2002.0094.

[12] C. Ganser, C. Teichert, AFM-based Nanoindentation of Cellulosic Fibers, John Wiley and Sons, Ltd, 2017, https://doi.org/10.1002/9781119084501.

[13] C. Ganser, C. Czibula, D. Tscharnuter, T. Schöberl, C. Teichert, U. Hirn, Combining adhesive contact mechanics with a viscoelastic material model to probe local material properties by afm, Soft Matter 14 (2018) 140–150, https://doi.org/10.1039/C7SM02057K.

[14] M. Griepentrog, G. Kraemer, B. Cappella, Comparision of nanoindentation and AFM methods for the determination of mechanical properties of polymers, Polym. Test. 32 (2013) 455–460, https://doi.org/10.1016/j.polymertesting.2013.01.011.

[15] H. Hertz, Über die berührung fester elastischer körper, J. für die Reine Angewandte Math. (Crelle's J.) 92 (1881) 156–171.

[16] X.D. Hou, N.M. Jennett, Defining the limits to long-term nano-indentation creep measurement of viscoelastic materials, Polym. Test. 70 (2018) 297–309, https://doi.org/10.1016/j.polymertesting.2018.07.022.

[17] G. Huang, H. Lu, Measurements of two independent viscoelastic functions by nanoindentation, Exp. Mech. 47 (2007) 87–98, https://doi.org/10.1007/s11340-006-8277-4.

[18] J.L. Hutter, J. Bechhoefer, Calibration of atomic–force microscope tips, Rev. Sci. Instrum. 64 (1993) 1868–1873, https://doi.org/10.1063/1.1143970.

[19] R.S. Lakes, Viscoelastic Materials, Cambridge University Press, Cambridge and New York, 2009, https://doi.org/10.1017/CBO9780511626722.

[20] M. Lei, B. Xu, Y. Pei, H. Lu, Y.Q. Fu, Micro-mechanics of nanostructured carbon/shape memory polymer hybrid thin film, Soft Matter 12 (2016) 106–114, https://doi.org/10.1039/c5sm01269d.

[21] D.C. Miller, M. Owen-Bellini, P.L. Hacke, Use of indentation to study the degradation of photovoltaic backsheets, Sol. Energy Mater. Sol. Cell. 201 (2019) 110082, https://doi.org/10.1016/j.solmat.2019.110082.

[23] A. Ngan, H.T. Wang, B. Tang, K.Y. Sze, Correcting power-law viscoelastic effects in elastic modulus measurement using depth-sensing indentation, Int. J. Solid Struct. 42 (2005) 1831–1846, https://doi.org/10.1016/j.ijsolstr.2004.07.018.

[24] W.C. Oliver, G.M. Pharr, An improved technique for determining hardness and elastic modulus using load and displacement sensing indentation experiments, J. Mater. Res. 7 (1992) 1564–1583, https://doi.org/10.1557/JMR.1992.1564.

[25] M.L. Oyen, Spherical indentation creep following ramp loading, J. Mater. Res. 20 (2005) 2094–2100, https://doi.org/10.1557/JMR.2005.0259.

[26] M.L. Oyen, Analytical techniques for indentation of viscoelastic materials, Phil. Mag. 86 (2006) 5625–5641, https://doi.org/10.1080/14786430600740666.

[27] M.L. Oyen, Sensitivity of polymer nanoindentation creep measurements to experimental variables, Acta Mater. 55 (2007) 3633–3639, https://doi.org/10.1016/j.actamat.2006.12.031.

[28] V.L. Popov, Contact Mechanics and Friction, Springer, Berlin, Heidelberg, 2017, https://doi.org/10.1007/978-3-662-53081-8.

[29] B. Tang, A.H.W. Ngan, A rate-jump method for characterization of soft tissues using nanoindentation techniques, Soft Matter 8 (2012) 5974–5979, https://doi.org/10.1039/c2sm25227a.

[30] D. Tranchida, S. Piccarolo, M. Soliman, Nanoscale mechanical characterization of polymers by AFM nanoindentation: critical approach to the elastic characterization, Macromolecules 39 (2006) 4547–4556, https://doi.org/10.1021/ma052727j.

[31] C.A. Tweedie, K.J. van Vliet, Contact creep compliance of viscoelastic materials via nanoindentation, J. Mater. Res. 21 (2006) 1576–1589, https://doi.org/10.1557/jmr.2006.0197.

[32] M.R. VanLandingham, N.K. Chang, P.L. Drzal, C.C. White, S.H. Chang, Viscoelastic characterization of polymers using instrumented indentation. i. quasi-static testing, J. Polym. Sci. B Polym. Phys. 43 (2005) 1794–1811, https://doi.org/10.1002/polb.20454.

[33] M.R. VanLandingham, J.S. Villarrubia, W.F. Guthrie, G.F. Meyers, Nanoindentation of polymers: an overview, Macromol. Symp. 167 (2001) 15–44.

[34] J.S. Villarrubia, Morphological estimation of tip geometry for scanned probe microscopy, Surf. Sci. 321 (1994) 287–300, https://doi.org/10.1016/0039-6028(94)90194-5.

[35] G.Z. Voyiadjis, A.H. Almasri, T. Park, Experimental nanoindentation of bcc metals, Mech. Res. Commun. 37 (2010) 307–314, https://doi.org/10.1016/j.mechrescom.2010.02.001.

[36] Y. Wang, L. Shang, P. Zhang, X. Yan, K. Zhang, S. Dou, J. Zhao, Y. Li, Measurement of viscoelastic properties for polymers by nanoindentation, Polym. Test. 83 (2020) 1–6, https://doi.org/10.1016/j.polymertesting.2020.106353.

[37] J. Woirgard, J.C. Dargenton, C. Tromas, V. Audurier, A new technology for nanohardness measurements: principle and applications, Surf. Coating. Technol. 100–101 (1998) 103–109.

[38] Y.Z. Xia, H. Bei, Y.F. Gao, D. Catoor, E.P. George, Synthesis, characterization, and nanoindentation response of single crystal fe–cr–ni alloys with fcc and bcc structures, Mater. Sci. Eng. 611 (2014) 177–187, https://doi.org/10.1016/j.msea.2014.05.079.

[39] C.Y. Zhang, Y.W. Zhang, K.Y. Zeng, L. Shen, Nanoindentation of polymers with a sharp indenter, J. Mater. Res. 20 (2005) 1597–1605, https://doi.org/10.1557/JMR.2005.0200.

[40] L. Zheng, X. Jiang, X.H. Deng, J.R. Yin, Y. Jiang, P. Zhang, Y.H. Ding, Mechanical characterization of PMMA by AFM nanoindentation and finite element simulation, Mater. Res. Express 3 (2016) 6, https://doi.org/10.1088/2053-1591/3/11/115302.

II.   Paper 2: Morphological characterization of semi-crystalline POM using NI

Petra Christöfl[a], Caterina Czibula[b,c,d], Tristan Seidlhofer[c,d], Michael Berer[a], Astrid Macher[a], Eric Helfer[a], Theresia Schrank[a], Gernot Oreski[a], Christian Teichert[b], Gerald Pinter[e]

[a]Polymer Competence Center Leoben, Leoben, Austria
[b]Insitute of Physics, Montanuniversität Leoben, Leoben, Austria;
[c]Christian Doppler Laboratory for fiber Swelling, Graz University of Technology, Graz, Austria;
[d]Institute of Bioproducts and Paper Technology, Graz University of Technology, Graz, Austria;
[e]Materials Science and Testing of Polymers, Montanuniversität Leoben, Leoben, Austria

Petra Christöfl authorship contribution:

Conceptualization: definition of the goals of the scientific work, selection of the used methods

Methodology: design of experiments

Investigation: implementation of NI measurements including evaluation

Writing: original draft

Morphological characterization of semi-crystalline POM using nanoindentation

Petra Christöfl, Caterina Czibula, Tristan Seidlhofer, Michael Berer, Astrid Macher, Eric Helfer, Theresia Schrank, Gernot Oreski, Christian Teichert & Gerald Pinter

Taylor & Francis
Taylor & Francis Group

Morphological characterization of semi-crystalline POM using nanoindentation

Petra Christöfl[a] (iD), Caterina Czibula[b,c,d], Tristan Seidlhofer[c,d], Michael Berer[a], Astrid Macher[a], Eric Helfer[a], Theresia Schrank[a], Gernot Oreski[a], Christian Teichert[b], and Gerald Pinter[e]

[a]Polymer Competence Center Leoben, Leoben, Austria; [b]Insitute of Physics, Montanuniversität Leoben, Leoben, Austria; [c]Christian Doppler Laboratory for Fiber Swelling, Graz University of Technology, Graz, Austria; [d]Institute of Bioproducts and Paper Technology, Graz University of Technology, Graz, Austria; [e]Materials Science and Testing of Polymers, Montanuniversität Leoben, Leoben, Austria

ABSTRACT

Nanoindentation (NI) is a contact method to investigate localized micromechanical properties of materials, whereby NI of semi-crystalline polymers is challenging. The influence of morphological structures such as spherulites or crystal-lamellae on localized NI depth-force behavior is discussed controversially in literature. Hence, the main objective of this study is to determine the influence of crystalline zones on NI results.

Polyoxymethylene (POM) exhibits high crystallinity with the spherulitic structure on the micrometer scale and was therefore chosen to proof the influence of spherulite distribution on NI results concerning modulus. Furthermore, the correspondence between the mean elastic modulus from different NI experiments and macroscopic compression tests will be demonstrated.

A POM tensile bar was investigated by NI with a large sphero-conical and a Berkovich indenter tip at different positions of its cross-section. Here, it was found that regions at the edge of the sample have a lower elastic modulus than regions in the middle of the cross-section. This agrees well with polarized light microscopy results, which reveal a skin layer with less crystallinity close to the sample edge. Therefore, the NI measurements in this edge zone result in a lower elastic modulus compared to the more crystalline middle of the cross-section.

In summary, semi-crystallinity influences the NI results obtained for POM and the mean of the elastic modulus distribution over the cross-section of the POM sample is in good agreement with macroscopic compression test results.

Introduction

Nanoindentation (NI) has developed into the standard depth-sensing technique over the last two decades to probe mechanical properties of materials locally. The most common used Oliver and Pharr (O&P)[1] method determines mechanical properties from force-displacement curves continuously controlled over time. As the O&P method was developed for hard, linear elastic and isotropic materials based on Hertzian[2] theory with frictionless and non-conforming surfaces, it is nowadays primarily used in the fields of metals,[3,4] and ceramics,[5] but also polymers are tested with the O&P method.[6]

In contrast to the elastic-plastic behavior of metals, polymers exhibit pronounced viscoelasticity at ambient conditions. This means in terms of NI that the response to a loading force from a polymer is not only dependent on force but also on time. The time dependency cannot be neglected but minimized by approximating with a step-like stress input in a creep (compliance) test. Recently, the creep response of poly(methyl methacrylate) (PMMA) has been extensively studied as an excellent example of an amorphous material.[7] PMMA as an amorphous polymer can be considered quite homogeneous and isotropic. Therefore, macroscopic compression tests, NI and Atomic Force Microscopy (AFM) yielded very comparable results.[8] However, most polymers do not exhibit a homogeneous and amorphous structure. In the class of thermoplastic polymers, semi-crystallinity is very common.

Here, polyoxymethylene (POM) has been chosen as a semi-crystalline thermoplastic material model due to its high degree of crystallinity[9] which origins from its spherulitic structure on the micrometer scale. POM crystallizes from the solution under a broad range of conditions into the superlattice of round shaped spherulites, which contain lamellar and amorphous regions in a star-shaped manner.[10] The parallel ordered lamellae originating from the center of a spherulite lead to a harder material region, whereas in the amorphous phases in between the lammelae behave softer. In the present study the highly complex morphology of melt crystallized POM was interpreted in relation to the degree of crystallinity, long period, lamellae thickness, spherulite size and spherulite size distribution, as well as to the skin-core layer structure of the cross-section. The expansion of crystallites follows the maximum temperature gradient, which leads to a skin-core layer composition for injection molded POM crystallizing from outside to inside.

The influence of semi-crystallinity on NI measurements is still a subject of research. Bedoui et al. examined semi-crystalline Polyamid 6 to characterize the influence of nanoscale heterogeneity on NI with a sharp Berkovich indenter tip.[11] They figured out that the mean modulus obtained by a bunch of NI measurements agrees with literature and associated the heterogeneous force-displacement curves of the indents to the lamellar structure of the semi-crystalline material. Also force discontinuities in the loading phase of NI were seen by them in context with the lamellar structure of the polymer. Iqbal et al.[12] proposed a so-called "bimodal behavior" of semi-crystalline poly(ether ether) ketone (PEEK), when indenting with a Berkovich indenter. After a large number of indentations, two groups of indents were visible in a load-displacement view. For the same indentation depth, a high and a low force indentation curve group appeared, which were associated with crystalline and amorphous regions. They also stated, that NI is a method to estimate the degree of crystallinity by doing a large indentation matrix over the sample and then quantify the indentation groups. Voiyiadjis et al.[13] picked up the idea of a "bimodal behavior" of semi-crystalline PEEK. They suggested that the bimodal behavior observed by Iqbal et al. could also be a reason of surface inhomogeneities such as scratches, because the indentation area of the Berkovich tip is not in the range of the spherulite size of PEEK. It is still an open question, if the "bimodal behavior" in[12] was a result of semi-crystallinity or surface roughness. Furthermore it is not clear in which way size and form of indenter tips as well as spherulites influence NI results. Mapping of the storage modulus[14–16] over a spherulite showed a correspondence with the lamellar structure gained by AFM and Optical Microscopy. Lamellae and amorphous structures in between revealed relevant differences.

The goal of this work is first of all to demonstrate that NI is a reliable method to get reproducible viscoelastic properties of semi-crystalline polymers such as POM. To the author's knowledge, the literature regarding the influence of morphology of semi-crystalline polymers to NI results is ambiguous.[11–13] Whether and how semi-crystallinity influences NI is still controversial, especially since also surface roughness affects the NI measurements to a certain degree. Within this work, it will be demonstrated that morphology influences local nanoindentation measurements significantly which leads to a distribution of the modulus across the investigated POM

sample. The calculation of a mean modulus value for the NI data across the sample yields a value which is comparable to macroscopic compression test results.

Materials and methods

POM samples

Polyoxymethylene (POM) Delrin 500 was chosen as a role material for a semi-crystalline polymer. This is a POM homopolymer resin from DuPont (E. I. du Pont de Nemours and Company, Wilmington Delaware, United States). For the present study, injection-molded tensile bars according to EN ISO 3167 (2003) (type A) were used. Details on processing conditions and further background are described in.[17] A $10 \times 4 \times 10$ mm sample was cut from a tensile bar (Figure 1) and embedded in epoxy resin. Afterwards it was grinded with silicon carbon up to a grain size of 2400 and polished with 3, 1, and 0.25 μm polish paste.

NI measurements were performed on the polished surface in 5×9 matrices over the sample with 5 indents in x direction to get statistics over a sample area with similar crystallinity and 9 indents in y direction across the cross section for four different measuring approaches (Table 1): O&P method with sphero-conical indenter tip at 15 as well as 20 mN maximum force, O&P method with Berkovich indenter tip and a maximum force of 20 mN and creep method with sphero-conical indenter tip and a maximum force of 15 mN. These four measuring approaches were set next to each other as illustrated in Figure 1.

Atomic Force Microscope (AFM) measurements were performed on the polished surface at the center and at the edge of the sample. Next, the embedded POM sample was etched in hydrochloric acid for 200 s and rinsed with isopropyl alcohol and distilled water.

For the investigation with polarized light microscopy, a 10 μm thick sample was cut from the embedded and etched sample with a microtome cutting device (Microtome Reichert Jung, Reichert Jung, Heidelberg, Germany). Afterwards, the thin section of POM was placed on a microscope slide and sealed with oil and a thin glass plate.
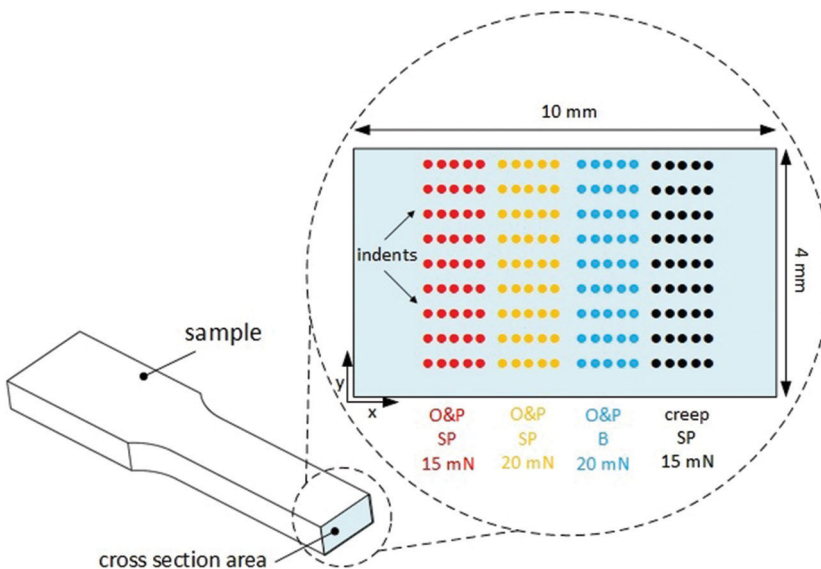

Figure 1. Tensile bar of POM (left) and embedded cross section of POM (right) with suggested indents marked as colored dots according to the measuring approaches from Table 1. SP: sphero-conical indenter tip; B: Berkovich indenter tip.

Table 1. Comparison of surface roughness taken from 20 μm AFM images and maximum indentation depth.

Method	Tip	F_{max} [mN]	h_{skin} [nm]	h_{core} [nm]	σ_{skin} [% h_{skin}]	σ_{core} [% h_{core}]
O&P	sp	15	640 ± 20	600 ± 50	3 ± 1	7 ± 1
creep	sp	15	450 ± 20	400 ± 30	4 ± 1	10 ± 1
O&P	B	20	2270 ± 40	2140 ± 90	1 ± 0.2	2 ± 0.3
O&P	sp	20	720 ± 30	700 ± 50	3 ± 1	6 ± 1

sp: sphero conical indenter tip; B: Berkovich indenter tip.

For the DSC measurements, 200–300 µm thick samples were cut from the POM tensile bar with the same microtome as used for the polarized light microscopy study. From this, 5–6 mm diameter disks were punched and put into a standard aluminum crucible with a perforated lid.

For Small Angle X-ray Scattering (SAXS) and Wide Angle X-ray Diffraction (WAXD) measurements, a whole tensile bar was used.

Nanoindentation

Oliver and Pharr method

The analysis of indentation curves is mostly done by the method of Oliver and Pharr.[1] The fitting of the unloading curve of the load penetration curve can be done by Equation (2.1), with h_p, the permanent indentation depth, h_{max}, the contact depth of the indenter at the maximum force F_{max} and a fitting parameter m.[18]

$$\frac{F}{F_{max}} = \left(\frac{h - h_p}{h_{max} - h_p} \right)^m \tag{2.1}$$

The contact stiffness S is the slope of the fit $S = \left(\frac{dF}{dh} \right)_{max}$ for the upper portion of the unloading curve. With $A_p = f(h_{max})$, the contact area of the indenter tip for h_{max} and β, the geometry factor of the indenter tip, the reduced modulus E_r is calculated by Equation (2.2).[18] E_r is hereby obtained with the assumption that the unloading is purely elastic.

$$E_r = \frac{\pi S}{2\beta \sqrt{A_p(h_{max})}} \tag{2.2}$$

The contact area at maximum load $A_p = f(h_{max})$ is determined by the indenter tip geometry and the depth of contact.[1] The functional form of f(h) was computed in a calibration process on a fused silica reference sample from Anton Paar with a thermal drift <0.2 pm/s.[19] Equation (2.3) defines the relationship between the elastic modulus E, the reduced modulus E_r and E_i, the elastic modulus of the indenter ($E_{diamond} = 1141$ GPa). ν_i is the Poisson's ratio of the indenter tip with $\nu_{diamond} = 0.07$. For the following experiments we defined $\nu = 0.42$ for POM.[20,21] Poisson's ratio is dependent on the degree of crystallinity. Therefore, a location dependent Poisson's ratio would lead to a more exact modulus result. Due to a lack in literature of such a value, it was decided to use a constant value.

More details about the used method can be found in our previous work.[9]

$$\frac{1}{E_r} = \frac{(1 - \nu^2)}{E} + \frac{(1 - \nu_i^2)}{E_i} \tag{2.3}$$

For the current work, an Anton Paar UNHT^3 Nanoindenter (Anton Paar, Graz, Austria) was employed. The Software "Indentation 8.0.24" (Anton Paar) was used for data recording and evaluation of the data. For practical reasons, the fit of the unloading curve was performed between 75 and 95% of F_{max} of the unloading curve. Tests were performed using an Anton Paar diamond sphero-conical nanoindenter tip (SG-A59) with $\beta = 1$, a tip radius of 0.1 mm and an opening

angle of 90° and an Anton Paar diamond three sided pyramidal Berkovich tip (B-V 31) with an opening angle of 142.3°. NI tests were operated on one embedded POM sample under laboratory conditions of 20 °C and 30% relative humidity in a matrix according to Figure 1 with 100 μm distance in x direction and 350 μm distance in y direction between each indent. Overall, indents were performed in a 5 × 9 matrix over the sample with 5 indents in x direction and 9 indents in y direction. The loading and unloading of the sample was performed linearly with 30 mN/min load rate and a maximum load of 15 mN with the sphero-conical indenter and 40 mN/min load rate and a maximum load of 20 mN with the Berkovich indenter. The constant force holding phase was 30 s. Before unloading, these were in both cases a constant-force holding phase of 30 s.

Nanoindentation creep measurements and parameter evaluation

Considering a rigid sphere in contact with an elastic plane to describe an indentation procedure, the relationship between force F and indentation depth h can be described according to [Equation 5.25],[22] as

$$F = \frac{4}{3}E^*R^{1/2}h^{3/2} \tag{2.4}$$

where R is the indenter tip radius and E^* the plane strain modulus. E^* is related to the Young's modulus E and Poisson's ratio as $E^*=E/(1-\nu^2)$. According to [Section 6.5][23] for a linear viscoelastic solid the superposition principle can be applied if Equation (2.4) is rearranged as:

$$(hR)^{3/2} = \frac{1}{E}\frac{3(1-\nu^2)}{4}RF \tag{2.5}$$

Substituting $\varepsilon = (h\ R)^{3/2}$ and $\sigma = \frac{3(1-\nu^2)}{4}RF$ in Equation (2.5) reveals the linear relationship $\varepsilon = \frac{1}{E}\sigma$. Obviously ε and σ do not represent physically stress and strain, but due to mathematical equivalence to Hooke's law the same linear viscoelastic theory can be applied. Therefore, an arbitrary creep response can be computed by introducing the compliance J with the convolution integral [Equation 2.3][23,24]

$$\varepsilon(t) = \int_0^t J(t-\tau)\dot{\sigma}(\tau)d\tau \tag{2.6}$$

Both, the creep compliance $J(t)$ and the relaxation modulus $E(t)$ are represented with a so-called Prony series, which makes an efficient interconversion possible.[25] This interconversion is necessary since with Equation (2.6) – as an intermediate step – $J(t)$ is estimated from the fitting procedure, not $E(t)$. After the conversion, the Prony series of the relaxation modulus[26]

$$E(t) = E_\infty + \sum_{i=1}^n E_i e^{(-t/\tau_i)} \tag{2.7}$$

is found. This series is parameterized with the infinity modulus E_∞ – characterizing the response at infinite time – and n pairs of relaxation times τ_i and moduli E_i. Alternatively, the instantaneous modulus $E_0 = E_\infty + \sum_{i=1}^n E_i$ is defined which characterizes the response at instant loading. Since the Prony series representation of $E(t)$ is equivalent to $E(t)$ of the generalized Maxwell model,[27] the parameters can be visualized as presented in Figure 2. Accordingly to $n = 2$ two Maxwell elements (GM2) are used.

The parameter evaluation of the creep curves was done by fitting Equation (2.6) to the converted creep experiments, i.e. σ, ε, respectively. To keep the amount of parameters low, two Prony series terms ($n = 2$) were used, which turned out to be a sufficient approximation. Besides, the Poisson's ratio was assumed as $\nu = 0.42$ according to.[20,21]
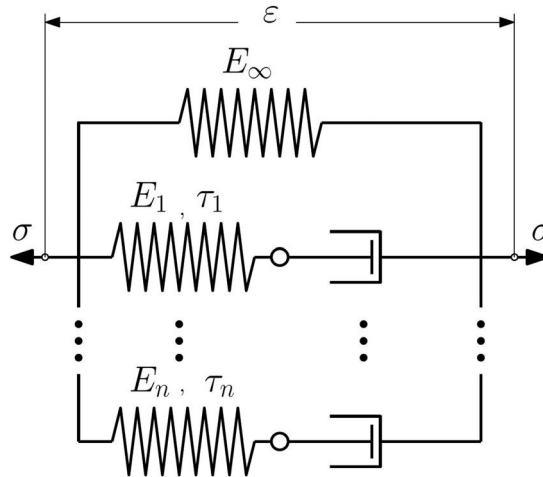
Figure 2. Generalized Maxwell model (GM) with a spring in parallel with n Maxwell bodies, consisting of a spring and a dashpot in series.

NI creep tests were operated under laboratory conditions of 20 °C and 20% humidity in a matrix according to Figure 1 with 100 μm distance between each indent in the x direction and 350 μm distance between each indent in the y direction with the sphero-conical indenter tip. The loading of the sample was performed linearly with 250 mN/min load rate up to a maximum load of 15 mN. The constant force holding phase was 300 s. Overall indents were performed in a 5 × 9 matrix.

Atomic force microscopy (AFM)

All Atomic Force Microscopy (AFM) experiments in this work have been acquired with an Asylum Research MFP-3D AFM (Asylum Research, Santa Barbara, CA, USA) at a temperature of 23 °C and a relative humidity level of 25%. The instrument is equipped with a closed-loop planar x–y-scanner with a scan range of $85 \times 85\ \mu m^2$ and a z-scanner with a range of about 15 μm. AFM topography scans have been recorded to characterize the roughness of the polished POM surfaces with standard silicon probes (Olympus, Japan) which have a tip radius of under 10 nm. Three independent $20 \times 20\ \mu m^2$ topography regions have been investigated for the center as well as for the edge of the sample. All the AFM images and corresponding data analysis were processed in the open-source software Gwyddion.[28] The RMS roughness σ corresponds to the standard deviation of the height values z as a measure of the vertical roughness:

$$\sigma = \sqrt{\frac{1}{N} \sum_{n=1}^{N} (z_n - \overline{z})^2} \qquad (2.8)$$

with z_n being the height value of pixel n, $\overline{z}$ the average image height, and N the pixel number of the image.

Polarized light microscopy (PLM) and light optical microscope (LOM)

For polarized light microscopy (PLM) investigations, the instrument Zeiss Axioscope 7 (Carl Zeiss Microscopy GmbH, Jena, Germany) with polarized light was used. The preparated thin-section POM samples (see section POM samples) were examined in transmitted light mode.

For Light optical microscope (LOM) investigations the Olympus SZX 12 was used and the thin section POM samples were examined with reflected light.

Small angle X-ray scattering (SAXS) & wide angle X-ray diffraction (WAXD)

The SAXS and WAXD measurements were performed with the Bruker Nanostar (Bruker Corporation, Massachusetts, USA) X-ray diffraction device. As the radiation source, an Iμ X-ray Source (Incoatec GmbH, Geesthacht, Germany) with monochromatic Cu Kα radiation and a wavelength of 1.5418 $\mathring{A}$ was used. The focusing was conducted by scatter-free circular slits with a diameter of 300 μm. A VÅNTEC-2000 2 D MicroGap detector (Bruker Corporation, Massachusetts, USA) was used for SAXS with a sample-detector distance of approximately 1096 mm. The calibration for the exact distance was obtained by measurement with a silver behanate standard for SAXS and aluminum oxide for WAXD. An image plate with a central hole was mounted around 40 mm behind the sample for simultaneous SAXS and WAXD measurements. In total, three tensile bars were examined using SAXS and WAXD. For each of them, three different measurement positions, located around the center of the tensile bar (where also the sample for the NI was cut out) were analyzed. Hence, the presented values are average values of in total 9 SAXS and WAXD measurements, respectively. The measurements were conducted along the thickness (4 mm direction) of the tensile bars. Both, the SAXS scattering patterns and the WAXD diffraction patterns were analyzed and radially integrated using Fit2D.[29] The morphological evaluation of the radially integrated SAXS patterns was done by "1D correlation"[30–32] with MATLAB (MathWorks Inc., Natick, Massachusetts, USA) scripts developed in.[9] The "plateau method" as further specified in[9] was used for the parameter calculation. The radially integrated WAXD patterns were peak-fitted in Origin (Origin, 9.0, OriginLab Corporation, Northampton, MA, USA) according to the procedure described in.[9] The determination of the amorphous phase was done by fitting the amorphous halo according to.[33] Miller indices of the corresponding crystal planes were correlated to the peaks according to.[34] Using the total area of crystalline and amorphous peaks, the degree of crystallinty $X_{C,WAXD}$ was calculated according to[9] in Equation (2.9), where a_c is the area under the crystalline peak and a_a is the area of the amorphous halo:

$$X_{C,WAXD} = \frac{a_c}{a_c + a_a} \tag{2.9}$$

Differential scanning calorimetry (DSC)

The Differential Scanning Calorimetry (DSC) measurements were performed with a DSC 4000 (Perkin Elmer, Waltham, USA), calibrated with indium for heatflow and temperature and zinc for temperature according to standard DIN EN ISO 11357 (2016).[35] The DSC measurements were conducted on circular punched microtome slices with a respective weight of (5.0 ± 0.5) mg. Three samples were subjected to a temperature program with a heating step from −75 to 230 °C with 10 °C/min and a cooling step from 230 to −75 °C with 10 °C/min after holding for one minute at 230 °C. The specific melting enthalpy was calculated from the area of the peak of the first heating (ΔH_m). The degree of crystallinity ($X_{C,DSC}$) was calculated according to equation (2.10) with ΔH_m^0, the specific melting enthalpy of 100% crystalline POM, which is 250 J/g according to:[36]
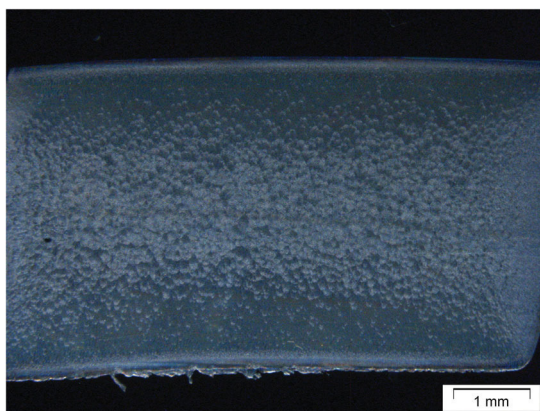
$$X_{C,DSC} = \frac{\Delta H_m}{\Delta H_m^0} \tag{2.10}$$

Figure 3. Light optical microscope image of cross sectional POM.

Results and discussion

Structural, morphological and surface characterization of POM

The POM tensile bar sample was produced by injection molding from the melt.[17] Due to the temperature gradient during cooling, the sample crystallized in a layered structure (Figures 3 and 4) with an outer skin layer and an inner core (bulk) layer. The shear layer is a transition zone between skin and core and is identified by high shear deformations near the mold wall. The skin layer is identified by a less crystalline and more amorphous zone than the bulk layer, where a lower cooling rate leads to better relaxation of the polymer chains and growth of the spherulites.[37] Moreover it seems that the spherulites in the shear layer show a predominant direction with a surface near nucleus. The size of the spherulites can be estimated with about (20 ± 5) μm in diameter in the shear and core layer (Figure 4).

DSC examinations show a crystallinity of (69 ± 1) %, whereas WAXD leads to crystallinity of (67 ± 1) %. These results are in good accordance with past examinations from[38] for POM Delrin 100 with a $X_{C,DSC}$ of (65 ± 1) % and $X_{C,WAXD}$ of (61 ± 1) % and an estimated spherulite size of 10–40 μm in diameter. Also Delrin 100 shows a differing spherulite distribution at the center and the edge of the sample.

Results from SAXS measurements reveal that the average long period along the thickness of the used POM Delrin 500 samples is (12.89 ± 0.06) nm and the average lamellar thickness amounts to (9.61 ± 0.04) nm. The semi-crystalline POM morphology in proportion to Berkovich and sphero-conical indenter tip is illustrated in Figure 5, whereupon the sphero-conical indenter tip is larger than the Berkovich indenter tip and the contact area is in the range of the spherulite size.

After the preparation of cross-sections and polishing routines, the surface of the POM sample has been investigated with AFM to characterize the surface roughness. The RMS roughness σ – as a measure for the vertical surface roughness – averaging over three $20 \times 20 \, \mu m^2$ AFM topography scans was calculated to be (18 ± 5) nm for the skin layer and (39.5 ± 5.5) nm for the core layer of the sample.

As can be seen in Figure 6, the surface of the whole sample shows scratches, which are most probably a result of the sample preparation.

Morphology and topography in context to NI

Both, surface roughness and semi-crystallinity are influencing NI measurements significantly. Surface roughness has an impact on the NI contact point detection between the indenter tip and

Figure 4. Polarized light microscope pictures of POM. (a) Edge of the unetched POM sample (b) edge of the etched POM sample with marked spherulites and zones.
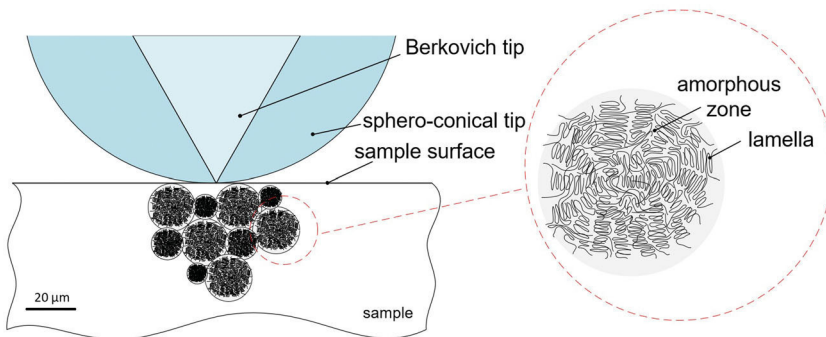

Figure 5. Sketch of the indentation process of sphero-conical and Berkovich indenter on a semi-crystalline polymer.

the material's surface.[39] Here, variations of the contact point lead to higher standard deviations for the obtained elastic modulus. Semi-crystallinity on the other hand, influences the NI results due to the difference in mechanical response of crystalline and amorphous phases, which are distributed throughout the sample. As expected, polymers with high crystallinity tend to exhibit a higher elastic modulus than low-crystalline polymers.[40] Here, the influence of the surface roughness and semi-crystallinity is investigated and discussed in more detail. Table 1 shows the relation between indenter tip, method, maximum force, indentation depth and surface roughness. The indentation depth at the edge of the sample (skin layer) is consistently higher than in the core layer. The surface roughness is smaller or even to 10% of the indentation depth for all methods and positions, although it is higher for the core layer. The surface roughness influences the creep tests more than the O&P tests, when using the sphero-conical indenter due to the lower
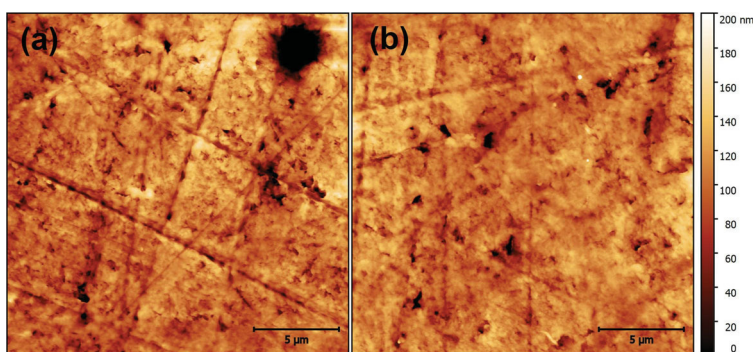
Figure 6. AFM topography image from the core layer (a) and the skin layer (b).

maximum indentation depth. For O&P tests with the Berkovich indenter, the indentation depth is much higher and the roughness is only 1% of h_{skin} and 2% of h_{core}. The influence of the surface roughness on the result of the NI tests is higher for the sphero-conical indenter than for the Berkovich indenter, and in general the influence of the surface roughness on NI results is higher at the center of the sample. However, concerning the contact point detection between tip and sample surface, it should be considered that the sharper Berkovich indenter tip will be more influenced by the surface roughness than the large sphero-conical indenter tip does.

Figure 7 shows the dependence of the diameter of the sphero-conical (+) and the Berkovich (*) indenter contact area A_p on the edge distance (y direction in Figure 1) for O&P indents with $F_{max}=20$ mN. Preliminary tests showed that in the force regime of 15–20 mN the indenter contact area A_p with sphero-conical indenter tip is in the size range of the spherulites of POM. Hence, we chose that force range to investigate the influence of spherulitic distribution to modulus results.

In Figure 7, the diameter of the contact area varies between 15 and 25 μm over the whole sample for the sphero-conical indenter tip and thus A_p is in the range of the size of the spherulites. For the Berkovich indenter tip, the diameter of the contact area is also constant over the whole sample, but in the range of 10 μm. The lamellae thickness, in contrast, is on the nanometer scale and therefore not in the range of the indenter contact area. This leads to the assumption that the distribution of the spherulites influences the results of NI with a spherical or Berkovich indenter tip. Proportions of indenter tips and spherulites are illustrated in Figure 5.

Comparing the modulus acquired by the O&P method with Berkovich (*) and sphero-conical (+) indenter in Figure 8, it is obvious that the modulus is lower at the edge of the sample and higher in the bulk sample. A comparison with the macroscopical compression test[17] reveals that O&P method with sphero-conical indenter better matches the compression test results. On the contrary, the moduli obtained with O&P method and Berkovich indenter overestimate the values obtained by O&P method with sphero-conical indenter and compression test. The smaller tip radius of the Berkovich indenter induces higher strain to the material[41] because the increase of the contact area with depth is smaller. This results in a more plastic and less elastic response of the material deformed with a sharp indenter tip. For the subsequent recovery of the material, the O&P method only takes the elastic response into account. More elastic recovery leads to a less steep unloading curve with a smaller S in equation (2.2) and therefore a smaller modulus. Indentation with Berkovich indenter tip leads to overestimation of modulus values, because more information is lost due to plastic deformation.

NI results for the O&P method and the viscoelastic creep experiments

Figure 9 exemplarily presents a GM2 simulation (dots) as described in section Materials and Methods and experimental data (line) for a creep indent in the center of the sample (red) in
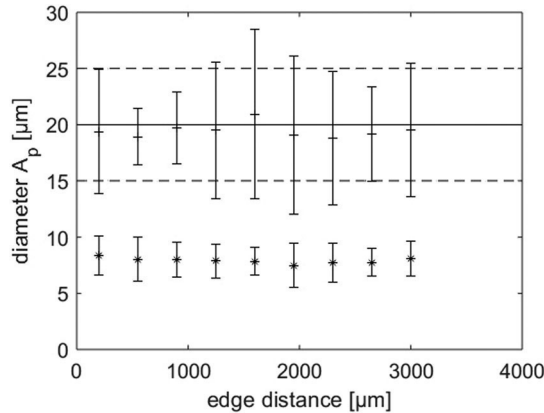
Figure 7. Diameter of the indenter contact area A_p in dependence of the edge distance of the POM sample with $F_{max}=20$ mN: sphero-conical intenter tip (+), Berkovich indenter tip (*). The line indicates the mean spherulite size. A_p values are expressed as mean and standard deviation calculated from five measurements in x direction.
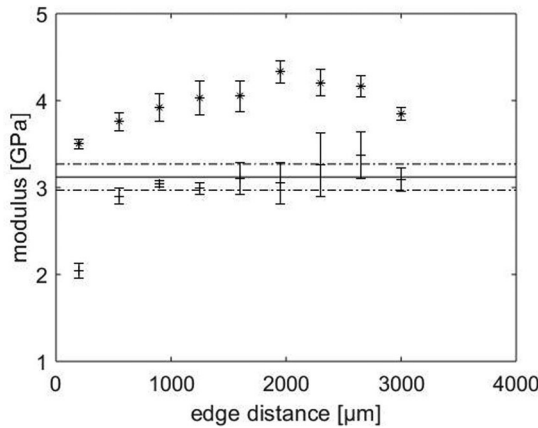

Figure 8. Elastic modulus results from the O&P method with sphero-conical indenter (+) and Berkovich indenter (*) in dependence on the distance from the edge of the POM sample (20 mN load) and comparison with macroscopic compression test results (line) from.[17] Nanoindentation values are expressed as mean and standard deviation calculated from five measurements in x direction.

contrast to an indent at the edge (black). Apart from a small kink at the beginning part of the curve, the simulation is in accordance with experimental data. Normalizing the data (c,d) reveals more creep at the less crystalline edge zone than at the more crystalline bulk zone. Also[26] reported for bulk POM that higher crystallinity in POM leads to less creep.

Calculating the complex modulus $E^*=E'+iE''$ to allow spectral representation of the viscoelastic parameters (Figure 10) as demonstrated by,[42] the storage modulus (E') differs for the edge (black) and the center (red) of the POM sample, whereas the loss modulus (E'') does not differ significantly. The differences of the elastic modulus from the center and the edge originate from the storage modulus and thus from the elastic contribution of the viscoelastic material. The results of O&P (*) and creep measurements in combination with GM2 modeling (+) are compared to macroscopic compression test data (line) and shown in Figure 11. Values are expressed as mean and standard deviation calculated from five measurements in x direction. The macroscopic compression tests were performed on the same material series in another work.[17] The elastic modulus gained by the O&P method is lower at the edge of the sample than in the center. It is also obvious that the standard deviation is smaller at the edge of the sample in contrast to higher standard deviations in the center. The modulus values from the O&P method are in good
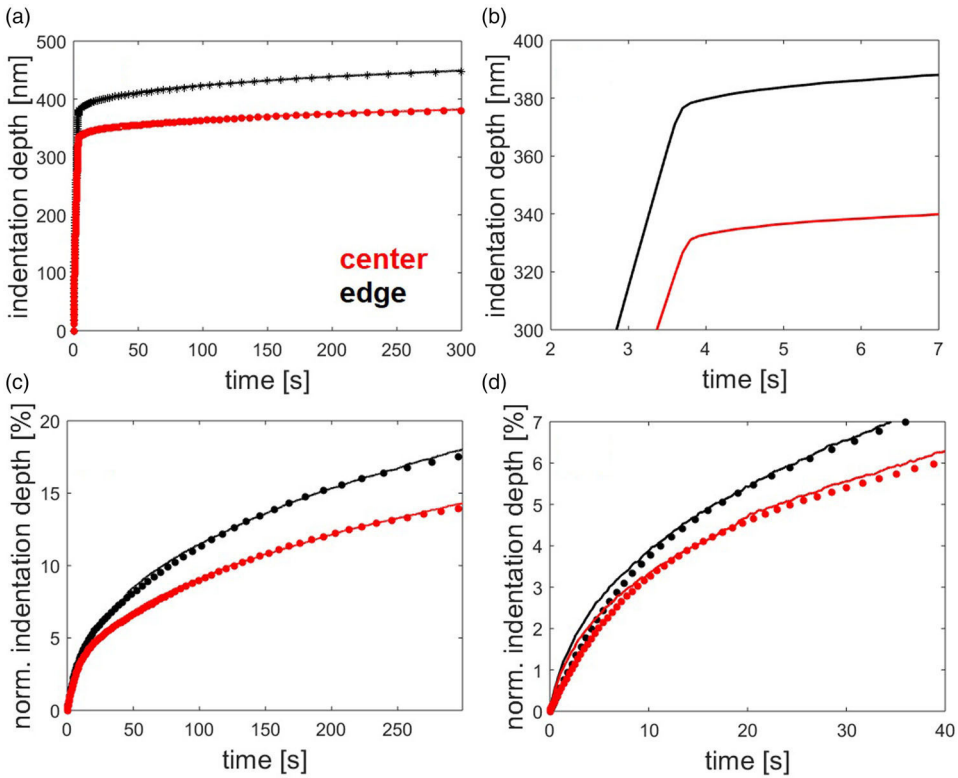
Figure 9. Experimental data (line) and GM2 simulation (dots) of creep experiments on POM at 15 mN at the edge of the sample (black) and at the the center of the sample (red): (a) creep curves from the center of the sample (red) in contrast to the edge of the sample (black) with GM2 simulations as dots, (b) detail view of (a), (c) normalized representation of (a), (d) detail view of (c).
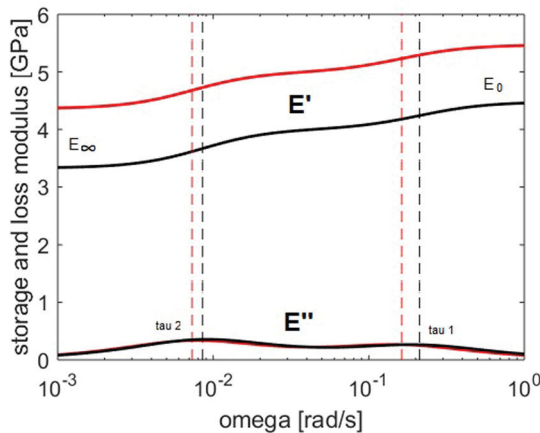
Figure 10. Complex modulus spectrum of GM2 simulation on POM at 15 mN at the edge of the sample (black) and at the center of the sample (red).

agreement with the macroscopic compression test results. On the other hand, the elastic modulus E_0 obtained by the creep test in combination with GM2 modeling overestimates the values from the O&P method and those from the macroscopic compression tests. Nevertheless, both, the O&P results and the creep results show the same modulus trend along the specimen thickness with a lower modulus at the edge of the sample and a higher modulus in the center. Also for the

Figure 11. Elastic modulus results from the O&P method (*) and E_0 results from GM2 modeling (+) in dependence on the distance from the edge of the POM sample (sphero-conical indenter, 15 mN load) and comparison with macroscopic compression test results (line) from.[17]

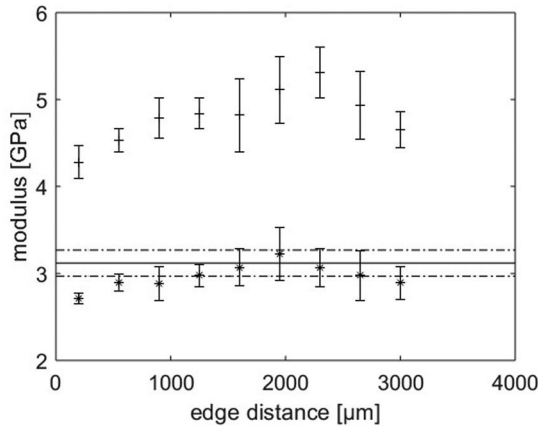creep tests, the standard deviation is smaller for the edge of the sample and higher for the bulk sample. Here, the GM2 simulation overestimates the O&P and compression values because the experiments were performed with different loading rates which leads to different deformation mechanisms. Furthermore, E_0 represents the modulus for instantaneous loading and can therefore be seen as an upper modulus.

Conclusion and outlook

NI of semi-crystalline POM delivers representative results for the elastic modulus, especially the O&P method with a big sphero-conical indenter tip is in good agreement with the macroscopic compression test for the investigated loading regime and can be taken into consideration for a straightforward and comprehensive mechanical testing of POM components. Lower modulus in the less crystalline skin layer and higher modulus for the more crystalline core layer can be observed for all methods, which is a result of the stiffer response of the crystalline phase in contrast to the amorphous phase of the material. The size of the POM spherulites are in the range of the indenter contact area (about 20 μm), meaning that the spherulitic distribution is influencing the NI results in the bulk crystalline zone of the sample in terms of higher modulus values with higher standard deviation. Higher crystallinity leads to higher elastic moduli, however, it was not possible to estimate the degree of crystallinity with NI as proposed by.[12]

Although the present POM sample was polished as a whole, it exhibits an about two times higher surface roughness in the core layer compared to the skin layer due to morphological differences. However, since the roughness values are in the nanometer range, the influence of the roughness on the standard deviation of the modulus is rather low with the large indenter tip used in this work. Therefore, the higher standard deviation for the modulus values in the core layer are caused by the spherulites in the crystalline zone.

Furthermore, creep response in the higher crystalline core layer is lower than in the skin layer – as one would expect – and a spectral representation of the creep modeling results demonstrates that the most prominent differences between skin and core layer originate from the elastic contribution of the viscoelastic POM. Comparing the instantaneous elastic modulus E_0 from the creep modeling with the elastic modulus obtained by the O&P method, the same trend across the cross section of POM is found.

The production process of melt crystallized POM leads to residual stresses in the skin-core layer construction. Within this work, it was not investigated in which way those stresses influence

NI results. Furthermore, the investigation of a low crystalline polymer like PP with bigger spherulites would be of scientific interest for comparison and will be investigated in future research.

Acknowledgements

Disclosure statement

No potential conflict of interest was reported by the author(s).

ORCID

Petra Christöfl http://orcid.org/0000-0003-4378-9534

References

[1] Oliver, W. C., and G. M. Pharr. 1992. An improved technique for determining hardness and elastic modulus using load and displacement sensing indentation experiments. *J. Mater. Res.* 7:1564–1583.
[2] Hertz, H. 1881. Über die berührung fester elastischer körper. *Journal Für Reine Und Angewandte Mathematik.* 92:156–171.
[3] Wurmshuber, M., D. Frazer, M. Balooch, I. Issa, A. Bachmaier, P. Hosemann, and D. Kiener. 2021. The effect of grain size on bubble formation and evolution in helium-irradiated Cu-Fe-Ag. *Materi. Charact.* 171: 110822.
[4] Wijaya, A., B. Eichinger, F. F. Chamasemani, B. Sartory, P. Hammer, V. Maier-Kiener, D. Kiener, M. Mischitz, and R. Brunner. 2021. Multi-method characterization approach to facilitate a strategy to design mechanical and electrical properties of sintered copper. *Mater. Des.* 197:109188.
[5] Zhu, T. T., A. J. Bushby, and D. J. Dunstan. 2008. Size effect in the initiation of plasticity for ceramics in nanoindentation. *J. Mech. Phys. Solids.* 56:1170–1185.
[6] Wang, J. H., J. H. Kim, H. J. Kang, and F. E. Talke. 2008. Influence of uniaxial extension on the mechanical properties of PET and PEN films. *Int. Polym. Process.* 23:17–23.
[7] Christöfl, P., C. Czibula, M. Berer, G. Oreski, C. Teichert, and G. Pinter. 2021. Comprehensive investigation of the viscoelastic properties of PMMA by nanoindentation. *Polym. Test.* 93:106978.
[8] Ganser, C., C. Czibula, D. Tscharnuter, T. Schöberl, C. Teichert, and U. Hirn. 2018. Combining adhesive contact mechanics with a viscoelastic material model to probe local material properties by AFM. *Soft Matter.* 14:140–150.
[9] Berer, M., M. Halb, M. Feuchter, G. Pacher, and G. Pinter. 2018. Fatigue fracture properties and morphology of polyoxymethylene (POM) plates produced under moderate processing conditions. *Int. J. Polym. Sci.* 7410925.
[10] Geil, P. H. 1967. Morphology of polyoxymethylene. *J. Macromol. Sci. Part A Chem. Pure Appl. Chem.* 1: 325–337.
[11] Bedoui, F., F. Sansoz, and N. S. Murthy. 2008. Incidence of nanoscale heterogeneity on the nanoindentation of a semicrystalline polymer: experiments and modeling. *Acta Mater.* 56:2296–2306.
[12] Iqbal, T., B. J. Briscoe, S. Yasin, and P. F. Luckham. 2013. Nanoindentation response of poly(ether ether ketone) surfaces: a semicrystalline bimodal behaviour. *J. Appl. Polym. Sci.* 130:4401–4409.
[13] Voyiadjis, G. Z., A. Samadi-Dooki, and L. Malekmotiei. 2017. Nanoindentation of high performance semicrystalline polymers: a case study on PEEK. *Polym. Test.* 61:57–64.
[14] Enrique-Jimenez, P., J. Vega, J. Martínez-Salazar, F. Ania, and A. Flores. 2016. Mapping the mechanical properties of poly(3- hydroxybutyrate-co-3-hydroxyvalerate) banded spherulites by nanoindentation. *Polymers.* 8:358.

[15] Butt, H. J., B. Cappella, and M. Kappl. 2005. Force measurements with the atomic force microscope: technique, interpretation and applications. *Surf. Sci. Rep.* 59:1–152.

[16] Magonov, S. 2011. High-Resolution visualization and compositional analysis of polymers with atomic force microscopy. *Int. J. Polym. Anal. Charact.* 16: 505–518.

[17] Usman, K. 2019. Mechanical behaviour of POM in dependence on molar mass, temperature and loading regime. Master Thesis, Technische Universitaet Chemnitz.

[18] Woirgard, J., J. C. Dargenton, C. Tromas, and V. Audurier. 1998. A new technology for nanohardness measurements: principle and applications. *Surf. Coat. Technol.* 100–101:103–109.

[19] Hou, X. D., and N. M. Jennett. 2018. Defining the limits to long-term nanoindentation creep measurement of viscoelastic materials. *Polym. Test.* 70:297–309.

[20] Tscharnuter, D., S. Gastl, and G. Pinter. 2012. Modeling of the nonlinear viscoelasticity of polyoxymethylene in tension and compression. *Int. J. Eng. Sci.* 60:37–52.

[21] Schrader, P., A. Gosch, M. Berer, and S. Marzi. 2020. Fracture of thin-walled polyoxymethylene bulk specimens in modes I and III. *Materials.* 13:5096.

[22] Popov, V. L. 2017. *Contact Mechanics and Friction.* Berlin, Heidelberg: Springer.

[23] Johnson, K. L. 1985. *Contact Mechanics.* Cambridge: Cambridge University Press.

[24] Tschoegl, N. W. 1989. *The Phenomenological Theory of Linear Viscoelastic Behavior.* Berlin, Heidelberg: Springer.

[25] Schapery, R. A., and S. W. Park. 1999. Methods of interconversion between linear viscoelastic material functions. Part I – a numerical method based on prony series. *Int. J. Solids Struct.* 36:1677–1675.

[26] Somiya, S.,. K. Yamada, and T. Sakai. 2011. Study on crystallinity dependency of creep deformation on GFRTP of polyoxythlene (POM). *Mech. Time Depend. Mater. Process. Conven. Multifunct. Mater.* 3: 275–282.

[27] Renaud, F., J.-L. Dion, G. Chevallier, I. Tawfiq, and R. Lemaire. 2011. A new identification method of viscoelastic behavior: application to the generalized maxwell model. *Mech. Syst. Signal Process.* 25:991–1010.

[28] Necas, D., and P. Klapetek. 2012. Gwyddion:an open-source software for SPM data analysis. *Open Phys.* 10: 181–188.

[29] Hammersley, A. 2016. FIT2D: a multi-purpose data reduction, analysis and visualization program. *J. Appl. Crystallogr.* 49:646–652.

[30] Strobl, G., and M. Schneider. 1980. Direct evaluation of the electron density correlation function of partially crystalline polymers. *J. Polym. Sci. Polym. Phys. Ed.* 18:1343–1359.

[31] Vonk, C. G., and G. Kortleve. 1967. X-ray small-angle scattering of bulk polyethylene. *Kolloid-Zuzpolymere.* 220:19–24.

[32] Goderis, B., H. Reynaers, M. H. J. Koch, and V. B. F. Mathot. 1999. Use of SAXS and linear correlation functions for the determination of the crystallinity and morphology of semi-crystalline polymers. Application to linear polyethylene. *J. Polym. Sci. B Polym. Phys.* 37:1715–1738.

[33] Zhao, X., and L. Ye. 2011. Structure and properties of highly oriented polyoxymethylene produced by hot stretching. *Mater. Sci. Eng.* 528:4585–4591.

[34] Shimomura, M. 1993. *Morphology Dependence of Vibrational Spectra of Polyoxymethylene and Poly(Ethylene Oxide) Crystals.* Doctoral Thesis, Osaka University.

[35] International Organisation for Standardisation, ISO 11357-1:3, 2016. Plastics - differential scanning calorimetry (DSC). 11357.

[36] Plummer, C. J. G., P. Bèguelin, and H. Kausch. 1995. The temperature and strain-rate dependence of mechanical properties in polyoxymethylene. *Polym. Eng. Sci.* 35:1300–1312.

[37] Liu, G., P. Zhu, and G. Edward. 2002. Morphology distribution and processing history of injection moulded polypropylenes. *Macromol. Symp.* 185:327–340.

[38] Berer, M., G. Pinter, and M. Feuchter. 2014. Fracture mechanical analysis of two commercial polyoxymethylene homopolymer resins. *Appl. Polym.* 131:19.

[39] Chen, Z., and S. Diebels. 2012. Modelling and parameter reidentification of nanoindentation of soft polymers taking into account effects of surface roughness. *Comput Math. Applic.* 64:2775–2786.

[40] Baur, E., J. G. Brinkmann, T. A. Osswald, and E. Schmachtenberg. 2007. *Saechtling Kunststoff Taschenbuch.* Munich, Germany: Carl Hanser Verlag GmbH & Co. KG.

[41] Cook, R. F., and M. L. Oyen. 2007. Nanoindentation behaviour and mechanical properties measurement of polymeric materials. *Int. J. Mater. Res.* 98:370–378.

[42] Seidlhofer, T., C. Czibula, C. Teichert, C. Payerl, U. Hirn, and M. H. Ulz. 2019. A minimum continuum representation of a transverse isotropic viscoelastic pulp fibre based on micromechanical measurements. *Mech. Mater.* 135:149–161.

III.   Paper 3: NI for fast investigation of PET film degradation

Petra Christöfl[a], Bettina Ottersböck[a], Caterina Czibula[b], Astrid Macher[a], Christian Teichert[c], Gerald Pinter[d], Gernot Oreski[a]

[a]Polymer Competence Center Leoben, Leoben, Austria;
[b]Institute of Bioproducts and Paper Technology, Graz University of Technology, Graz, Austria;
[c]Insitute of Physics, Montanuniversität Leoben, Leoben, Austria;
[d]Materials Science and Testing of Polymers, Montanuniversität Leoben, Leoben, Austria

Petra Christöfl authorship contribution:

Conceptualization: definition of the goals of the scientific work, selection of the used methods

Methodology: design of experiments

Investigation: implementation of NI measurements including evaluation

Writing: original draft

Nanoindentation for Fast Investigation of PET Film Degradation

PETRA CHRISTÖFL [1,4,5] BETTINA OTTERSBÖCK,[1]
CATERINA CZIBULA,[2] ASTRID MACHER,[1] CHRISTIAN TEICHERT,[3]
GERALD PINTER,[4] and GERNOT ORESKI[1]

1.—Polymer Competence Center Leoben, Leoben, Austria. 2.—Institute of Bioproducts and Paper Technology, Graz University of Technology, Graz, Austria. 3.—Insitute of Physics, Montanuniversität Leoben, Leoben, Austria. 4.—Materials Science and Testing of Polymers, Montanuniversität Leoben, Leoben, Austria. 5.—e-mail: petra.christoefl@pccl.at

The lifetime of industrial polymer products is in many cases limited by aging. Therefore, it is necessary to develop a fast and sensitive method to detect polymer aging at an early stage. A commercially available 50-μm-thick and transparent polyethylene terephtalate (PET) film was aged under different artificial conditions, and the evolution of mechanical properties with increasing aging time was investigated via nanoindentation (NI) and tensile testing. Chemical aging was studied with gel permeation chromatography (GPC), and physical aging was monitored by the first heating of differential scanning calorimetry. NI data evaluated with the method of Oliver and Pharr was compared to tensile test data with good agreement between the results on the macro- and nanoscales. Furthermore, a correlation between NI creep data and GPC data was obtained, which indicates that the aging of the PET films primarily originated from chemical aging. This study states that NI is an appropriate method to determine degradation of PET at an early stage.

INTRODUCTION

Polymers like polyethylene terephtalate (PET) are used in different fields of industry ranging from applications in the packaging[1] and fiber sectors[2] to the utilization as backsheets in photovoltaic modules.[3,4] One big issue of polymers applied in demanding applications is degradation, especially when they are exposed over time to elevated temperatures and humidity. The sum of all the physical and chemical changes of a polymer during application time is defined as aging. To make polymers more sustainable and reliable regarding their area of application, it is essential to understand their mechanical behaviour before and after the degradation processes. Nanoindentation (NI), a standard depth-sensing technique for testing the local mechanical properties of materials, holds a good possibility to investigate aged polymers. The Oliver and Pharr (O&P)[5] method was established to identify mechanical properties from NI tests. It was primarily developed for linear elastic, hard, and isotropic materials, based on the theory of Hertz,[6] with frictionless surfaces in non-conforming contact.[7] Although mostly applied to metals, NI studies for polymers have been gaining interest in recent times.[8–11] Yet, it needs to be considered that polymers are—in contrast to metals—viscoelastic materials which exhibit a time-dependent mechanical behavior. Therefore, several limitations need to be considered when applying the O&P method to polymers.[12–14]

PET is a commonly used thermoplastic polymer,[15] which is known to hydrolyse above its glass transition temperature,[16] leading to significantly shorter molecular chains and lower molecular mass.[15] In addition to this irreversible chemical aging due to hydrolysis, PET also shows reversible physical aging in terms of the reorientation and recrystallization of the molecular fragments.[17] There have been reports on the influence of aging on the mechanical properties of semi-crystalline PET.[17–21] However, to the authors' knowledge, there is no study on the correlation of bulk- and nanomechanical properties with the chemical aging effects of PET under aging conditions.

The main goal of this work is to demonstrate that NI is capable of determining the mechanical properties of aged PET by analyzing the change of the elastic modulus, similar to a tensile test. The aging effect is further demonstrated by comparison with an unaged PET sample. Furthermore, it will be pointed out that, with the method of NI, the elastic modulus of severely degraded (embrittled) materials can also be distinguished, which is hardly possible with tensile testing due to the impeded sample preparation. A further important goal is to prove that NI in the creep mode correlates with the loss in molecular weight of PET, and therefore to chemical aging. This NI creep method is presented as a quick and sensitive method to detect the degradation of PET, as well as mechanical changes of PET at an early stage of aging.

MATERIALS AND METHODS

PET Samples

For the following study, a commercially available 50-μm-thick and transparent PET film was investigated. The film was manufactured by co-extrusion, where it was biaxially drawn in a 3-layer construction. These films are widely used as a component in backsheets for photovoltaic (PV) modules; further details about the PET samples are provided in Ref. 22. Seven batches of PET were chosen for our investigations. The aging of each of the batches with sample numbers 1–6 was performed, according to the scheme in Table I, in the climate chamber WLK 64-40 (Weiss Umwelttechnik, Vienna, Austria) with 85% RH. An unaged PET sample served as a reference (sample number 7).

For NI, each sample (as presented in Table I) was cut into a 50 μm × 1.5 cm × 1 cm piece which had been embedded separately in epoxy resin. Then, they were ground with silicon carbide up to a grain size of 4000, and polished with 3-μm and 1-μm diamond polishing paste.

NI tests were performed on the polished surface of each sample according to the measurement scheme in Fig. 1. For each sample, 20 measurements were performed in the position "edge", and 20 measurements were performed in the position "middle" for the O&P measuring approach (see "Nanoindentation Oliver & Pharr" section). Furthermore, 20 measurements were performed in the position "edge" and 20 measurements were performed in the position "middle" for the nanoindentation creep mode (see "Nanoindentation Creep" section). For the tensile tests, rectangular samples with a size of 15 mm × 100 mm were cut out.

Nanoindentation Oliver & Pharr

Nanoindentation curves were evaluated by the O&P method.[5] The fitting of the unloading curve of the indentation load penetration curve was executed by Eq. 1:

$$\frac{F}{F_{max}} = \left(\frac{h - h_{p}}{h_{max} - h_{p}}\right)^{m} \tag{1}$$

Here, h_{max} is the contact depth of the indenter at the maximum force F_{max}, h_{p} is the permanent indentation depth, and m is the fitting parameter.[23] The slope of the fit $S = \left(\frac{dF}{dh}\right)_{max}$ is the contact stiffness for the upper portion of the unloading curve. The contact area of the indenter tip for h_{max} is $A_{p} = f(h_{max})$. The reduced modulus, $E_{r,}$ is calculated by Eq. 2:[23]

$$E_{r} = \frac{\pi S}{2\beta\sqrt{A_{p}(h_{max})}} \tag{2}$$

E_{r} is thereby obtained assuming that the unloading is purely elastic. The geometry factor, β, equals 1 for a circular sphero-conical indenter tip. The contact area at maximum load $A_{p} = f(h_{max})$ is determined by the depth of the contact and the indenter tip geometry.[5]

For calibration, the functional form of $f(h)$ was computed on a fused silica reference sample from Anton Paar, with a thermal drift < 0.2 pm/s.[24] Equation 3 defines the relationship between E_{i} the elastic modulus of the indenter ($E_{diamond}$ = 1141 GPa), the elastic modulus E, and the reduced modulus E_{r}:

$$\frac{1}{E_{r}} = \frac{\left(1 - v^2\right)}{E} + \frac{\left(1 - v_{i}^2\right)}{E_{i}} \tag{3}$$

v_{i} is the Poisson's ratio of the indenter tip with $v_{diamond}$ = 0.07. For the following experiments, we defined v = 0.3 for PET.[25] Further details about the applied method can be found in our previous works.[8,9]

For the current study, an Anton Paar UNHT[3] Nanoindenter (Anton Paar, Graz, Austria) was employed. For practical reasons, the fit of the unloading curve was performed between 75% and 95% of F_{max}. Tests were performed using an Anton Paar diamond sphero-conical nanoindenter tip (SD-C06), with a tip radius of 10 μm and an opening angle of 90°. NI tests were performed on the embedded PET samples under the laboratory conditions of 22°C temperature and 30% RH in a matrix according to Fig. 1, with a distance of 20 μm between each indent in the x direction at two positions in the middle and on the edge of the sample. The loading and unloading ramps during the experiment were performed linearly with a load rate of 30 mN/min and a maximum load of 15 mN. The holding phase at constant force was 30 s. The software "Indentation 8.0.24" (Anton Paar) was employed for recording and evaluation of the data. The elastic modulus was calculated from 20 measurements for each position, and the results are given in terms of mean ± standard deviation.

Table I. Climate chamber aging parameters of the PET samples at a relative humidity of 85%

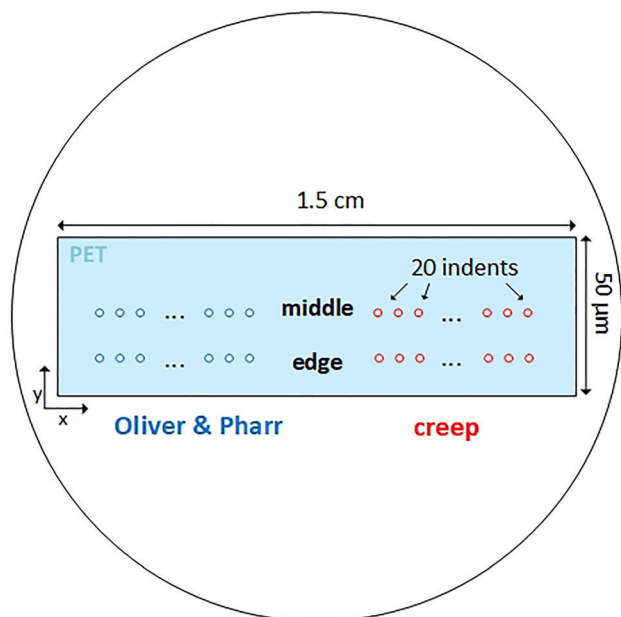| Sample number	Aging time (h)	Aging temperature (°C)
1	1000	85
2	2000	85
3	3000	85
4	1000	95
5	2000	95
6	3000	95
7	Unaged	

Fig 1. The embedded cross-section of PET samples with exemplary indents marked as coloured circles: Oliver & Pharr approach (blue) and creep measurement (red) each in the positions middle and edge (Color figure online).

Nanoindentation Creep

NI creep tests were performed with the spheroconical indenter under laboratory conditions of 22°C temperature and 30% relative humidity (RH), according to Fig. 1. The distance between each indent in the x direction was 20 μm for each position in the middle and on the edge of the sample. The loading of the samples was performed linearly with a 250-mN/min load rate up to a maximum load of 15 mN. The holding phase at constant force was 300 s, when the creep of the PET samples was recorded. To compare the creep behavior of differently aged PET samples, mean creep curves from 20 measurements for the positions middle and edge were calculated and normalized.

Tensile Tests

Tensile tests were carried out with a Zwick Roell Z001 testing device (Ulm, Germany) at ambient conditions according to EN ISO 527-3,[26] with a testing speed of 50 mm/min and a gauge length of 50 mm. The elastic modulus was determined for at least 7 samples per test series.

Gel Permeation Chromatography (GPC)

An Agilent Technologies GPC 50 (Santa Clara, USA) device with two detectors (one recording the refractive index and a 4-capillary viscosity detector) was used along with two PSS SDV analytical linear M columns (8 × 50 mm and 8 × 300 mm) having a particle size of 5 μm. A universal calibration with polystyrol (PS) (K = 1.91 10^{-4} dl g^{-1} and α = 0.693) and a detector calibration with PS standard 133,000 Da was carried out to provide proper calculation of the molecular weight.[27] The samples were dissolved in pure hexafluoroisopropanol (HFIP), with subsequent slow dilution with chloroform (CHCl$_3$) to reach a final concentration of around 2.5 mg ml^{-1} in a CHCl$_3$:HFIP mixture (98:2 vol%). A stable temperature of 40°C at the beginning of the experiment was chosen in order to prevent early precipitation of the samples. The amount of the injected sample was 100 μl.

Differential Scanning Calorimetry (DSC)

DSC was performed with a Perkin Elmer DSC 4000 (Waltham, USA) to determine the thermal behaviour of PET in the range of 23–270°C with a heating rate of 10 K min^{-1}. About 10 mg of the samples were cut and put into 50-μl pans with perforated lids. To prevent a further oxidation process, the measurements were performed in a nitrogen atmosphere. Peak temperatures and enthalpies for melting and crystallization were evaluated according to ISO 11357-3,[28] with three samples to obtain an average.

RESULTS AND DISCUSSION

Aging-Induced Molecular Changes

The main mechanisms in polymer aging studied within this report are physical (reversible) and chemical (irreversible). Physical aging processes effect changes in physical properties with the main phenomena of relaxation and post-crystallization. Chemical aging affects the chemical composition and molecular structure and the weight of a

polymer.[29] The influence of chemical aging on the entire aging process can be observed by measuring the molecular weight by GPC. Figure 2a shows the evolution of molecular mass with aging time gained by GPC measurements for the temperatures 85°C and 95°C, both with 85% RH.

The molecular mass decreases from approximately 26,300 g mol^{-1} to values below 10,000 g mol^{-1} for samples aged at 85°C as well as at 95°C. The decrease is more dominant for the 95°C aged samples. Humidity and elevated temperature lead to chemical aging of PET by hydrolysis. Here, chain scission takes place at ester linkages where water molecules break down ester bonds. Such reverse esterification leads to smaller chain fragments of the main chains of PET, and therefore to a decline of molecular weight.[30,31]

Physical aging is a reversible and temperature-induced process and can be observed in the first heating curve of DSC. Figure 2b shows DSC curves for the first heating of PET aged at 85% RH for 0 h, 1000 h, 2000 h, and 3000 h at 85°C and 95°C. The first DSC heating of the samples aged at 85°C shows no significant differences in crystalline structures, as indicated by Fig. 2b. For samples aged at 95°C, slight changes of the melting peak with further aging time were detected. An alteration of the peak shape for 95°C-aged PET samples indicates that the crystal heterogeneity was increased during degradation, which leads to slight recrystallization and reorientation processes of the molecular chains.[32] In addition, there was no sign of physical aging. Looking at Fig. 2, chemical aging does not seem to be the only triggering factor for physical aging. The glass transition of the unaged PET is in the range of 70–115°C with the peak temperature at 106°C, whereas for aged PET (85°C, 85% RH and 95°C, 85% RH) the glass transition temperature peak (Tg) is above 110°C.[22] Aging at temperatures in the range of its glass transition provides physical aging,[33] and leads to recrystallization and reorientation, as seen in the first heating of DSC. Samples aged at 95°C are more affected by this process than the 85°C-aged samples, because of the proximity to Tg.

Evolution of the Elastic Modulus from PET Aging

There is evidence in the literature that the aging of PET influences its mechanical properties.[17,29,34,35] Figure 3 shows the elastic modulus depending on aging time of the PET samples gained by the NI O&P method, as well as the tensile testing results for the aging conditions 85°C (Fig. 3a) and 95°C (Fig. 3b) accompanied by the results of the unaged samples.

Moduli from the tensile tests match the NI results quite well, except for the samples aged for 3000 h at 85°C, where the samples were strongly embrittled. Fractures of the tensile test specimens during the tensile tests start at a defect which acts as a notch.

Compared to low embrittled (unaged) material, sample preparation on highly embrittled material is likely to cause more defects in the test specimens, which disproportionately influences the tensile test results. Samples from 2000 h and 3000 h with 95°C aging were too brittle for tensile testing, and therefore those samples were investigated only by NI (see Fig. 3b).

Although there is a slight trend towards higher elastic moduli with higher aging time for 85°C (Fig. 3a), the modulus determined by both methods does not change significantly. However, for PET samples aged at 95°C (Fig. 3b), the elastic modulus obtained by both methods increases significantly. As already observed in Fig. 2a, aging leads to a reduction of molecular weight caused by chain scission. This is followed by a decrease of the macromolecule concentration and interlamellar spacing, both leading to embrittlement and an increasing elastic modulus of PET with aging.[29,34] The molecular mass reduction is more pronounced for samples degraded at 95°C, hence the aging effect is also more visible in terms of elastic modulus. Furthermore, previous investigations detected a rising elastic modulus gained by the NI O&P method from degradation,[36,37] which is in good accordance with the findings of this work.

The difference in the elastic moduli of NI in the positions middle and edge of the unaged sample is remarkable, which may be caused by the semi-crystalline structure of PET. In a previous publication,[9] we have shown that semi-crystalline polyoxymethylene (POM) exhibits a layered morphological structure leading to different elastic moduli for the middle and edge of the cross-sectional sample. Investigations of a cross-sectional tensile bar of injection-molded POM by NI revealed that a less semi-crystalline skin layer, originating from the production process, leads to lower elastic moduli, whereas the more semi-crystalline core layer leads to significantly higher elastic moduli.[9] As for POM, PET also shows a lower modulus at the edge of the sample and a higher modulus in the middle (Fig. 3). Also[38] discovered, from indentation experiments on PET foils, that amorphous layers of PET show lower elastic moduli in contrast to crystalline layers with higher elastic moduli.

Nevertheless, the embedding material (epoxy resin) also influences the NI results at the edge of the sample. Since the indentation depth is about 1–2 μm, as presented in Figure S1 in the Supplementary Material, the stress field of indentation is rather small. The influence of the embedding material on the NI results of the PET samples is assumed to be minor. For quantitative analysis of the elastic modulus over aging time, the influence of the embedding material stays the same for all the sample and is therefore neglectable.
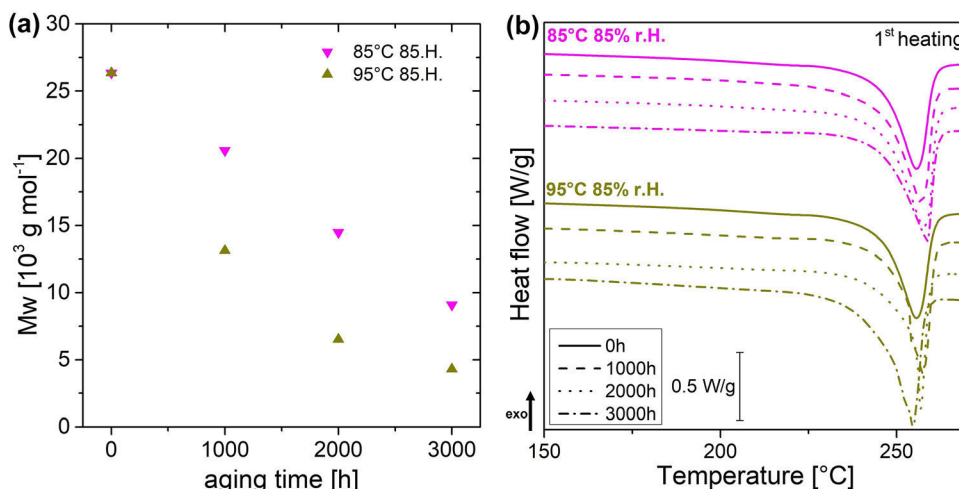
Fig 2. (a) Molecular weight over aging time for 85°C at 85% RH and 95°C at 85% RH, and (b) DSC curves for the first heating of PET aged for 0 h, 1000 h, 2000 h, and 3000 h with conditions of 85°C at 85% RH and 95°C at 85% RH.
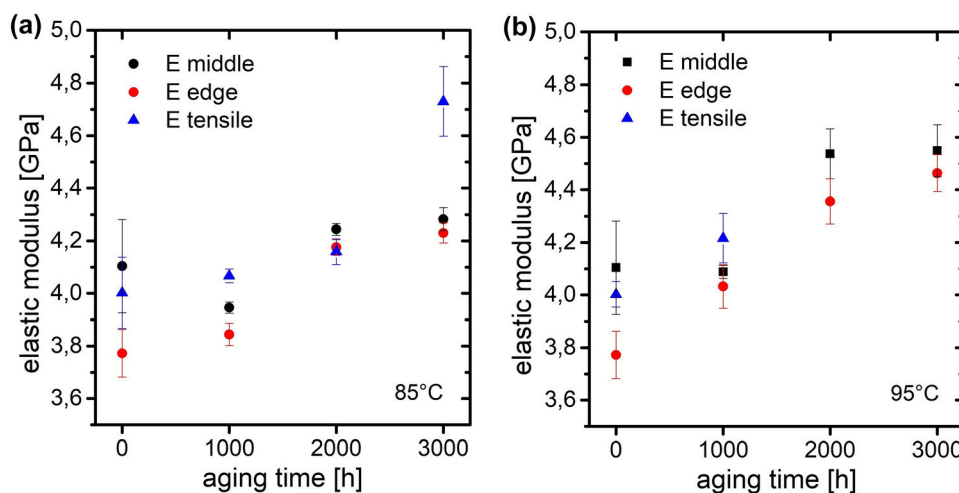

Fig 3. Development of the elastic modulus from NI (black dots-middle, red dots-edge) and tensile test (blue triangles) over aging time with 85°C and 85% RH (a), and 95°C and 85% RH (b). The elastic modulus was calculated in terms of mean and standard deviation (Color figure online).

NI Creep in Context to Molecular Weight

Representative data of creep curves obtained by NI are presented in Fig. 4 for each aging condition and position, where the normalized indentation depth correlates with the aging time. The unaged sample exhibits the highest creep, followed by samples aged at 85°C with ascending aging times from 1000 h to 3000 h. Samples aged with 3000-h aging time indicate the lowest creep. The same trend was recognized for samples aged at 95°C. Such a decrease in the creep behavior with increasing aging time for PET was also observed for NI studies.[39]

When comparing NI creep at the positions at the middle and edge of the sample, it should be noticed that PET reveals more creep at the edge for the unaged sample. The reason for this may originate from the layered structure of semi-crystalline PET, with more amorphous phases at the edge of the

sample and more crystalline phases in the center. A detailed investigation of this behavior has been published in Ref. 9 for POM. For longer aging times, the difference between the middle and the edge decreases by means of the creep behavior. The DSC results indicate minor recrystallization processes for the aged samples, which may lead to a more homogenized morphology throughout the sample, and a more homogeneous creep behavior in the middle and edge of the samples.

The maximum of the normalized indentation depth (from Fig. 4) correlates clearly with the molecular weight (M_w), which is depicted in Fig. 5. Here, the results for the M_W obtained from the GPC measurements, which are presented in Fig. 2a, are plotted logarithmically. For PET samples aged with 85°C (Fig. 5a), the logarithmic correlation between the molecular weight and the indentation depth follows a polynomial fit for the position middle ($R = 0.99$) and a linear fit ($R = 0.90$) for the position
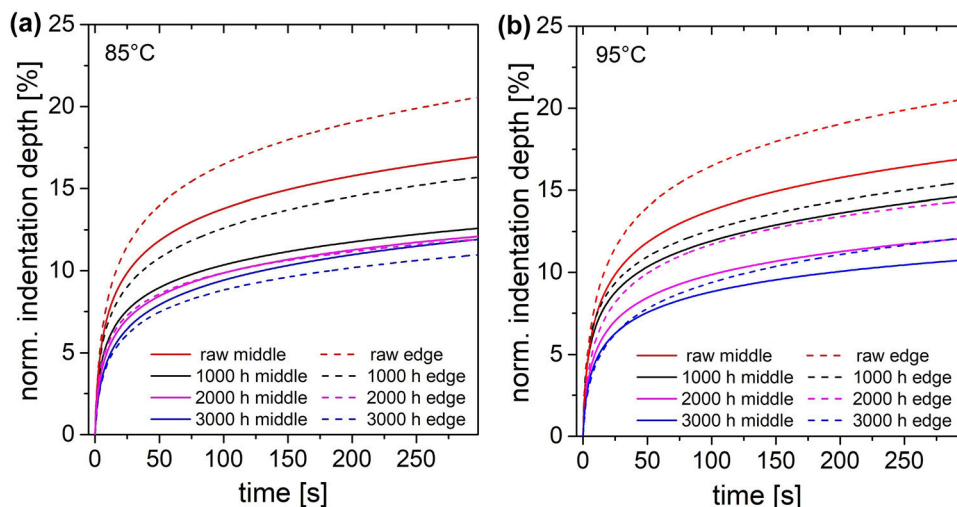
Fig 4. Normalized mean creep curves obtained from 20 individual curves for different aging (0 h, 1000 h, 2000 h, 3000 h) at (a) 85°C and 85% RH, and (b) 95°C and 85% RH. The positions middle and edge of the indents are indicated with a solid and dashed line, respectively.

edge. The logarithmic correlation in the position middle (R = 0.99) and edge (R = 0.98) between the maximum normalized indentation depth and the molecular weight of the PET samples aged with 95°C is linear (Fig. 5b).

The influence of molecular weight on NI creep compliance has previously been extensively investigated.[40] That work revealed that increasing molecular weight makes a polymer more creep-resistant. This observation was made, e.g., for injection-molded semi-crystalline polyethylene and polypropylene. It was stated that the application of a constant load during creep experiments results in intramolecular tensions. To decrease these tensions, a polymer with a high M_W can push low-strained molecule parts to highly-strained regions of the contact zone, and vice versa. This way, strains can be well distributed due to the high structural connectivity.

Here, this model is applied to unaged PET with its higher molecular weight in contrast to the lower molecular weight-aged PET. For unaged PET, the higher molecular weight with longer main chains exhibits higher connectivity between the high- and low-strain zones, which decreases the resistance to further indenter penetration and enlarges the creep. Regions with higher intramolecular tensions cause continued molecular displacement to reduce internal strain. Regarding aged PET, chain scission leads to shorter chained molecules,[29] and therefore the material exhibits a lower driving force to reduce intramolecular strain, because of the lack of connectivity between high- and low-strained regions of a molecule. Hence, aged samples offer higher resistance to indentation penetration at constant force, because of weak intramolecular tension and consequent low molecular displacement (see Fig. 6), which is revealed by lower creep. Longer aging times causes lower creep, because the molecular

weight reduction due to aging leads to lower intramolecular tension and therefore to a lower driving force for creep.

The linear correlation between molecular weight and maximum normalized indentation depth for 95°C aging shown in Fig. 5b indicates that chemical aging is the main aging mechanism in this temperature regime. Physical aging plays a minor role for 95°C-aged samples according the first heating of DSC (Fig. 2b). Also, the aging affects the middle and the edge of the sample in the same way. For samples aged with 85°C (Fig. 5a), the edge results lead to linear correlation between the molecular weight and the maximum normalized indentation depth in the double logarithmic presentation. The creep results from the position middle seem to stagnate for longer aging times. Chemical aging of PET is caused by hydrolysis,[29] which means that reactions occur of the ester linkages and the water molecules. We assume that this mechanism happens primarily at the edge of the PET sample, because the crystalline part of PET is impermeable to water, and hydrolysis occurs in the amorphous phase of PET,[29,30] which corresponds to the edge of the sample. The samples aged at 95°C show more signs of physical aging than the 85°C-aged samples, which means that reorientation and recrystallization took place, and that the amorphous and crystalline phases are more homogeneous and spread all over the sample. Thus, water molecules are able to penetrate the whole sample and hydrolysis can take place in the middle and at the edge of the sample.

CONCLUSION AND OUTLOOK

The aging behavior of thin PET films depends on temperature and humidity levels as well as on the duration of the aging. Here, an unaged PET film
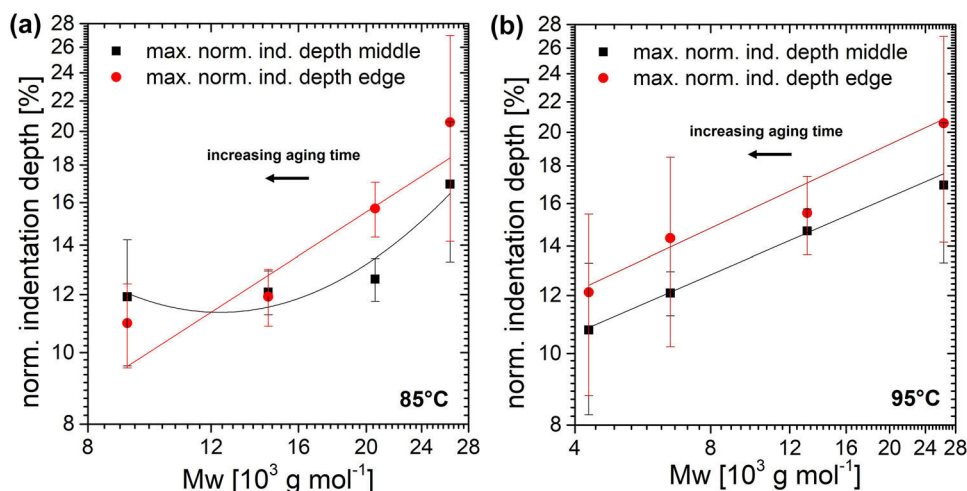
Fig 5. Maximum normalized indentation depth from NI creep tests in the middle of the (a) 85°C and 85% RH and (b) 95°C 85%RH-aged PET samples in comparison with the molecular weight (M_w) at 0 h, 1000 h, 2000 h, and 3000 h aging time in double logarithmic presentation. Black squares indicate the indents obtained from the middle of the sample and red dots the indents from the edge of the sample (Color figure online).
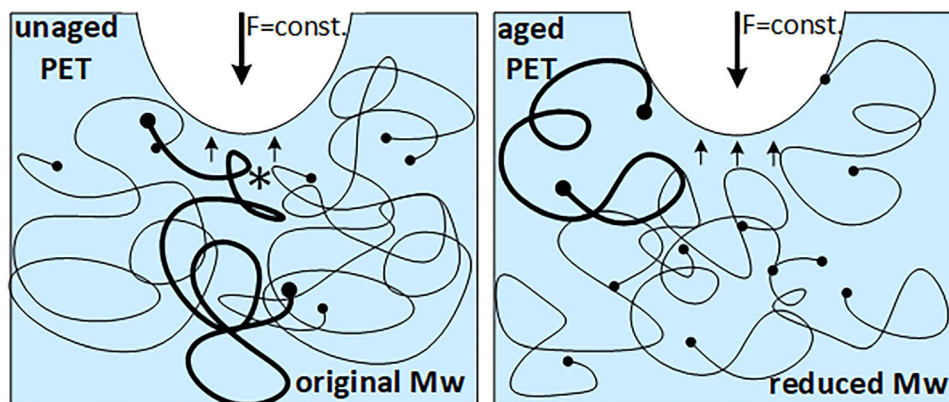

Fig 6. Cross-section of schematic indentation of unaged and aged PET samples by constant force, F: * indicates intramolecular stresses that will lead to more creep of the unaged PET in contrast to the aged PET (adapted from Ref. 40); small arrows indicate pushback forces of the PET.

was investigated to be compared with differently aged PET films in order to detect changes of its mechanical properties.

The main outcome of this investigation is the possibility to determine precise and local elastic moduli of thin PET films with NI comparable to tensile tests. Furthermore, the elastic modulus of highly-embrittled samples can also be determined. NI creep measurements are able to detect degradation with the same sensitivity as GPC measurements in less time. Thus, they provide fast, reliable, and locally resolved information about the early aging of PET.

Future experiments will cover aging behavior of thin films aged by natural weathering as well as by artificial aging. Furthermore, investigations of cross-sections of samples will give more space-resolved information of aging.

CONFLICT OF INTEREST

On behalf of all authors, the corresponding author states that there is no conflict of interest.

OPEN ACCESS

SUPPLEMENTARY INFORMATION

The online version contains supplementary material available at https://doi.org/10.1007/s11837-022-05278-0.

REFERENCES

1. R. Nisticò, *Polym. Test.* https://doi.org/10.1016/j.polymertesting.2020.106707 (2020).
2. R.P. Borg, O. Baldacchino, and L. Ferrara, *Constr. Build. Mater.* https://doi.org/10.1016/j.conbuildmat.2016.01.029 (2016).
3. G. Oreski and G.M. Wallner, *Sol. Energy.* https://doi.org/10.1016/j.solener.2005.02.008 (2005).
4. A. Omazic, G. Oreski, M. Halwachs, G.C. Eder, C. Hirschl, L. Neumaier, G. Pinter, and M. Erceg, *Sol. Energy Mater. Sol. Cells.* https://doi.org/10.1016/j.solmat.2018.12.027 (2019).
5. W.C. Oliver and G.M. Pharr, *J. Mater. Res.* 7, 1564 (1992).
6. H. Hertz, *Journal für reine und angewandte Mathematik* 92, 156 (1881).
7. V.L. Popov, *Contact Mechanics and Friction* (Springer, Berlin, 2017).
8. P. Christöfl, C. Czibula, M. Berer, G. Oreski, C. Teichert, and G. Pinter, *Polym. Test.* https://doi.org/10.1016/j.polymertesting.2020.106978 (2021).
9. P. Christöfl, C. Czibula, T. Seidlhofer, M. Berer, A. Macher, E. Helfer, T. Schrank, G. Oreski, C. Teichert, and G. Pinter, *Int. J. Polym. Anal. Charact.* https://doi.org/10.1080/1023666X.2021.1968122 (2021).
10. C. Ganser, C. Czibula, D. Tscharnuter, T. Schöberl, C. Teichert, and U. Hirn, *Soft Matter.* https://doi.org/10.1039/C7SM02057K (2018).
11. G.M. Odegard, T.S. Gates, and H.M. Herring, *Exp. Mech.* https://doi.org/10.1007/BF02428185 (2005).
12. S.R. Cohen, and E. Kalfon-Cohen, *Beilstein J. Nanotechnol.* https://doi.org/10.3762/bjnano.4.93 (2013).
13. M.R. VanLandingham, N.K. Chang, P.L. Drzal, C.C. White, and S.H. Chang, *J. Polym. Sci.* 43(14), 1794. (2005).
14. S. Yang and Y. Zhang, *J. Appl. Phys.* https://doi.org/10.1063/1.1651341 (2004).
15. N.S. Allen, M. Edge, M. Mohammadian, and K. Jones, *Polym. Degrad. Stab.* https://doi.org/10.1016/0141-3910(94)90074-4 (2016).
16. K. Looney and B. Brennan, *EU PVSEC.* https://doi.org/10.4229/EUPVSEC20142014-5DO.10.5 (2014).
17. K. Aljoumaa and M. Abboudi, *Appl. Phys.* https://doi.org/10.1007/s00339-015-9518-0 (2016).
18. H. Zhou, E.A. Lofgren, and S.A. Jabarin, *J. Appl. Polym. Sci.* 112(5), 2906 (2009).
19. D.E. Mansour, F. Swientek, I. Kaaya, D. Philipp, and L. Pitta Bauermann, *EU PVSEC.* https://doi.org/10.4229/35thEUPVSEC20182018-5CV.3.28 (2018).
20. B. Ottersböck, G. Oreski, and G. Pinter, *J. Appl. Polym. Sci.* https://doi.org/10.1002/app.44230 (2016).
21. A. Flores, F. Ania, and F.J. Baltà-Calleja, *Polymer.* https://doi.org/10.1016/j.polymer.2008.11.037 (2009).
22. B. Ottersböck, *Natural and artificial weathering tests of polymer films used in solar applications* (Doctoral dissertation, Montanuniversität Leoben, Leoben, Austria, 2017).
23. J. Woirgard, J.C. Dargenton, C. Tromas, and V. Audurier, *Surf. Coat. Technol.* 100–101, 103. (1998).
24. X.D. Hou and N.M. Jennett, *Polym. Test.* 70, 297 (2018).
25. S.L. Zhang and J.C.M. Li, *J. Polym. Sci.-Part B.* https://doi.org/10.1002/polb.10542 (2004).
26. International Organisation for Standardisation, ISO 527-3. 1995. Plastics - Determination of tensile properties: Part 3: Test conditions for films and sheets, 527-3.
27. K. Weisskopf, *J. Polym. Sci.* 26, 1919 (1988).
28. International Organisation for Standardisation, ISO 11357-3. 1999. Plastics – Differential scanning calorimetry (DSC) Part 3: Determination of temperature and enthalpy of melting and crystallization, 11357-3.
29. G.W. Ehrenstein and S. Pongratz, *Beständigkeit von Kunststoffen* (Carl Hanser Verlag, Munich, 2007).
30. S.S. Hosseini, S. Taheri, A. Zadhoush, and A. Mehrabani-Zeinabad, *J. Appl. Polym. Sci.* 103(4), 2304 (2007).
31. M. Edge, M. Hayes, M. Mohammadian, N.S. Allen, T.S. Jewitt, K. Brems, and K. Jones, *Polym. Degrad. Stab.* 32(2), 131 (1991).
32. H. Hagihara, A. Oishi, M. Funabashi, M. Kunioka, and H. Suda, *Polym. Degrad. Stab.* 110, 389 (2014).
33. L.C.E. Struick, *Polym. Eng. Sci.* 17, 3 (1977).
34. B. Fayolle, E. Richaud, and X. Colin, *J. Mater. Sci.* 43, 6999 (2008).
35. A. Flores and F.J. Baltá-Calleja, *Philos. Mag. A.* https://doi.org/10.1080/01418619808239987 (1998).
36. T. Pertin, G. Minatchy, M. Adoue, A. Flory, and L. Romana, *Polym. Test.* https://doi.org/10.1016/j.polymertesting.2019.106194 (2020).
37. C. Andreia, J.V. Tavares, C.M. Gulminea, and L.A. Lepienski, *Polym. Degrad. Stab.* https://doi.org/10.1016/S0141-3910(03)00108-3 (2003).
38. A. Flores and F.J. Baltà-Calleja, *J. Appl. Phys.* https://doi.org/10.1063/1.1418000 (2001).
39. D.C. Miller, M. Owen-Bellini, and P.L. Hacke, *Sol. Energy Mater. Sol. Cells.* https://doi.org/10.1016/j.solmat.2019.110082 (2016).
40. C. Tweedie and K. Van Vliet, *J. Mater. Res.* https://doi.org/10.1557/jmr.2006.0197 (2006).

IV. Paper 4: Improved NI methods for polymer based multilayer film cross-sections

P. Christoefl[1], J. E. Jakes[2], J. Geier[1], G. Pinter[3], G. Oreski[1], D. Stone[4], C. Teichert[5]

[1]Polymer Competence Center Leoben GmbH, Roseggerstrasse 12, 8700 Leoben, Austria

[2]USDA Forest Service, Forest Product Laboratory, One Gifford Pinchot Drive Madison, WI 53726, United States.

[3]Montanuniversitaet Leoben, Materials Science and Testing of Polymers, Otto Glöckel-Straße 2/II, 8700 Leoben, Austria

[4]University of Wisconsin-Madison, 1509 University Ave, Madison, WI 53706, United States

[5]Montanuniversitaet Leoben, Chair of Physics, Dept. Physics, Mechanics, and Electrical Engineering, Franz Josef-Strasse 18, 8700 Leoben, Austria

Petra Christöfl authorship contribution:

Conceptualization: definition of the goals of the scientific work, selection of the used methods

Methodology: design of experiments

Investigation: evaluation of the NI measurements

Writing: original draft

Improved nanoindentation methods for polymer based multilayer film cross-sections

P. Christoefl[1], J. E. Jakes[2], J. Geier[1], G. Pinter[3], G. Oreski[1], D. Stone[4], C. Teichert[5]

[1]Polymer Competence Center Leoben GmbH
Roseggerstrasse 12, 8700 Leoben, Austria
petra.christoefl@pccl.at
[2]USDA Forest Service, Forest Product Laboratory
One Gifford Pinchot Drive Madison, WI 53726, United States.
[3]Montanuniversitaet Leoben, Materials Science and Testing of Polymers
Otto Glöckel-Straße 2/II, 8700 Leoben, Austria
[4]University of Wisconsin-Madison
1509 University Ave, Madison, WI 53706, United States
[5]Montanuniversitaet Leoben, Chair of Physics, Dept. Physics, Mechanics, and Electrical Engineering
Franz Josef-Strasse 18, 8700 Leoben, Austria

Abstract

Nanoindentation (NI) is capable to investigate mechanical properties on a small scale and is also suitable to examine cross-sections of co-extruded or laminated multilayer films with thicknesses in the μm-regime. The standard Oliver-Pharr (O&P) NI method [1] is typically employed to measure the elastic modulus and hardness. However, this standard method assumes a homogeneous and semi-infinite sample that is rigidly supported. NI on thin, multilayer film cross-sections violate these assumptions because nanoindentations are always near free edges and heterophase interfaces. The structural compliance method was developed by Jakes et al. to correct NI results for edge effects and specimen-scale flexing [2]. The method is based on the discovery, that the effect of both edges and specimen-scale flexing is to introduce a structural compliance (Cs) into the measurement. Applied to a multilayer, the Cs showed a strong position dependence, i.e., the effect was larger near the edges and layer interfaces. The Cs correction had little effect on the hardness values; however, the influence on measured elastic modulus was significant. There, the corrected modulus values tended to be higher than the uncorrected ones in the stiff layers. After the Cs correction, the position dependence of the elastic modulus within a given layer was not observed within experimental uncertainties.

1. Introduction

In certain situations, a single polymer cannot fulfil all requirements needed for a special application. A backsheet (BS) film for photovoltaic application, which is used as a reference sample in this work, should for example provide mechanical stability and electrical isolation for PV modules [3, 4]. Generally, multilayer films of three or more layers are used to engineer a BS with those characteristics and offer a good mixture of required properties. The outer layers have to resist weathering factors such as moisture exposure and high or low temperatures. As outer layers often polyvinylflouride (PVF), polyvinylidene fluoride, or polyethylene terephthalate (PET) are used. In the past also many other materials have been used, amongst others polyamide (PA) [5] and other fluoropolymers [6].The inner layer is furthermore equipped with an adhesion layer or a functionalized surface to get a good connection to the encapsulant of the PV module. The main task of the core layer is to provide mechanical stability, which is crucial for lifetime. PET is the most used polymer for this purpose. [7]

Currently, the mechanical properties of multilayer BS are probed by tensile tests mostly [8], which gives good mechanical property measurements of the whole polymeric film. There have also been some approaches of testing multilayers by NI. In [9] a multilayer thin film polymer was investigated. In order to get the elastic modulus of the single films by NI, specimen for every single layer were produced and measured. In [10] a multilayer BS was embedded in epoxy resin and the modulus of the different layers was gained by NI.

So far it was not possible to investigate the mechanical properties of single BS films as part of a multilayer in cross-section without embedding of the sample. Embedding and grinding of samples is the most common way to examine cross-sections. But it is unclear if the surrounding embedding material such as epoxy resin, and grinding process influences the multilayer sample either chemically or also mechanically. In this work we will introduce a method to characterize polymeric multilayer film cross-sections mechanically without embedding or grinding. Jakes et. al. [2, 11] developed an NI method to investigate unembedded wood cells in cross-section by preparing surfaces using diamond knives and structural compliance method to consider specimen scale flexing and edge effect in the NI analysis. Wood cell walls are similar to multilayer BS with both systems consisting of multiple polymer films with thicknesses in the μm regime. The structural compliance method is based on the discovery, that the effect of both, edges and specimen scale flexing is to introduce a structural compliance (Cs) into the measurement. The Cs is like the machine compliance in that it is independent of NI size and adds to the total measured compliance.

Wood is mechanically comparable to thermoplastic polymers, as it also behaves viscoelastically under deformation. Therefore, the method of Jakes [2] served as reference for this work.

NI was originally developed to test hard, rigid and homogeneous materials such as metals and ceramics in a bulk. The O&P [1] method to gain the elastic modulus assumes an elastic relaxation after deformation of the material. In both, wood cell walls and BS, the relaxation of polymers is conversely time-dependent, subsequently viscoelastic, which makes the interpretation of the NI O&P data difficult. Nevertheless, there have been some efforts comparing viscoelastic NI data from creep tests with NI O&P data on thermoplastic PMMA [12]. With a well-considered experimental setup, viscoelastic modulus from creep test and elastic modulus from O&P method are comparable for thermoplastic PMMA.

When using a Berkovich indenter tip, the representative strain of the indentation is about 8% [13], meaning in the transition between viscoelastic and viscoplastic deformation, which complicates the interpretation of modulus data. Simpler indenter tip geometries like a spherical indenter would be more suitable for interpretation of polymers NI data, because here the representative strain is lower than the elastic strain limit [12, 14]. There are two reasons why Berkovich indenter tip has been chosen within this work: First of all, Berkovich indenter tip can probe small volume by simply controlling the load, and small volume is needed for the thin layers. Secondly a self - similar indenter geometry such as Berkovich is needed to employ the Cs method to correct for specimen scale flexing and edge effect [2, 15]. Fortunately there has been some progress in comparison of Berkovich NI data with traditional mechanical tests recently [16–19].

Main goal of this work is to show that the Cs method is suitable to isolate and remove Cs effects for NI measurements in polymeric multilayer material cross-sections. Thus, it is possible to get position independent results for hardness and elastic modulus for every layer of a multilayer photovoltaic BS by NI, which is necessary for further development and lifetime prediction of BS.

2. Materials and Methods

Multilayer sample

Polymeric BS were chosen to be investigated as a reference sample for a thin multilayer system (see *Figure 1*).
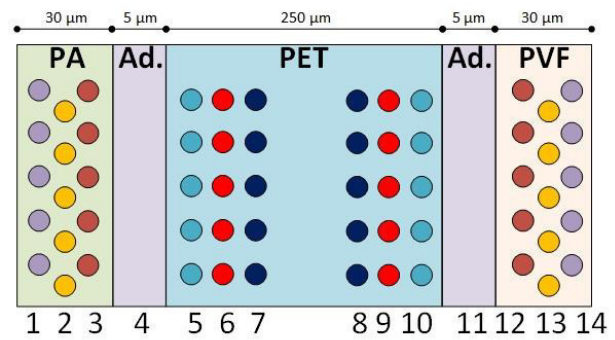
Figure 1: Polymeric multilayer in cross-section: PA- Polyamide, Ad.- Adhesive, PET- Polyethylene terephthalate, PVF- Polyvinyl fluoride with the associated column number for NI, dots symbolize NI imprints.

The multilayer consists of layers from PA (Polyamide), PET (Polyethylene terephthalate), PVF (Polyvinyl fluoride), and an adhesive. In previous works, samples were embedded, ground and polished to investigate the cross-section [14, 20], which could lead to mechanical damage of the samples or chemical changes due to the epoxy or the polishing paste. To overcome these circumstances, Jakes et.al. [2] developed a method to prepare thin multilayer films for NI without embedding the sample. An obviously non-damaged 1x1 cm sample of the multilayer was chosen to be investigated and glued with 5-minute epoxy adhesive to a steel slug sample holder (Figure 2). Then the sample holder was adapted to fit into a Leica EM UC7 ultramicrotome (Wetzlar, Germany) equipped with a diamond knife. An apex of 15° was cut using a hand razor. Then, with a diamond knife, the apex was cut off using progressively thinner sections from 2 μm

to 200 nm until an ultrasmooth flat surface of suitable size was prepared for NI.
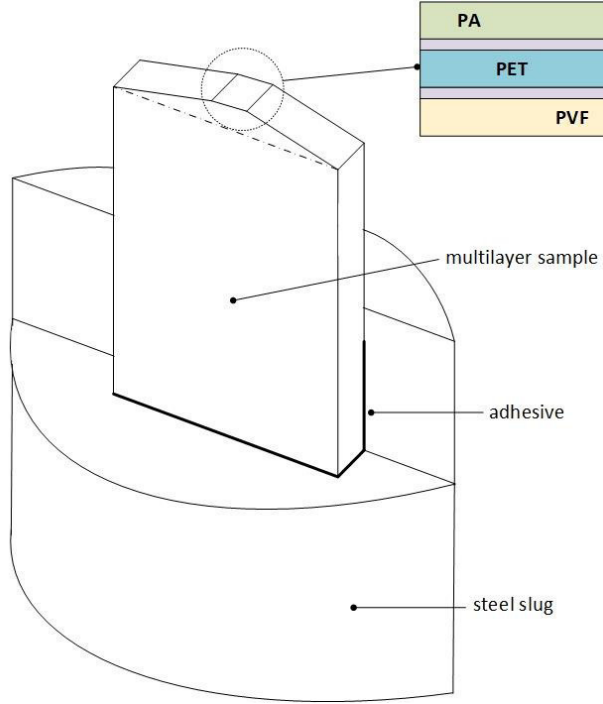

Figure 2: Sample preparation method for NI following [21].

Nanoindentation

For NI, a hard indenter tip is pressed into a material to measure mechanical properties like the elastic modulus or hardness. Here, a diamond Berkovich indenter tip is used. The loading, hold at maximum load, and unloading segments are pre-defined in a force and time load function while the indentation depth is recorded accordingly. The Meyer's hardness H is defined as:

$$H = \frac{F_{max}}{A_0}$$

with the maximum force F_{max} and the contact area A_0. A_0 is calculated with the area calibration function of the Berkovich probe as a function of the indentation contact depth h_c with $A_0 = f(h_c)$ [22].

The elastic properties are calculated by fitting the unloading curve of the load (F)- penetration (h) curve to

$$F = A(h - h_f)^m$$

where A, h_f and m are fitting parameters [1]. Then the contact stiffness S at the start of the unloading curve is calculated by differentiating F and substituting h_0, the indentation depth at the beginning of the unloading curve, for h.

$$S = \frac{dF}{dh} = mA(h_0 - h_f)^{m-1}$$

Hereby it is assumed that the unloading segment is an elastic deformation in contrast to the load and hold segment, which is (visco-) elastic and plastic. It is assumed that some unavoidable plasticity also occurs at the beginning of the unloading curve and therefore the fit of

the unloading curve usually is executed without the first 5 % of the unloading curve. Then the elastic properties are calculated using the contact compliance Cp, the inverse of S:

$$C_p = \frac{1}{S} = \frac{1}{E_{eff} A_0^{1/2}}$$

with the effective modulus of contact E_{eff}. The Young's modulus E_s can then be calculated

$$\frac{1}{E_{eff}} = \frac{\pi^{\frac{1}{2}}}{2\beta}\left(\frac{1 - v_s^2}{E_s} + \frac{1 - v_d^2}{E_d}\right)$$

with E_d, the Elastic modulus of the diamond tip (1137 GPa) and v_d, the Poisson's ratio of the diamond (0.07) and v_s, the Poisson's ratio of the sample. In this work, v_s is assumed to be 0.35 for all polymer films as supposed for hard thermoplastics [23]. The numerical factor β is assumed to be one in this work, although there are some debates about it [24].

The NI machine compliance evaluation according to [25] resulted in Cm= 2.9 µm/N which was anticipated regarding prior measurements and leading to size independent hardness (H) and elastic modulus (E) on the fused silica reference sample meaning that the calibration worked out well.

Basic NI description relies on testing a homogeneous sample, which is a rigidly supported half-space. For the multilayer sample, the rigid support cannot be assumed, as the sample may flex, when the indenter tip is pressed into the sample. Specimen may flex near free edges or near neighboring layers of the multilayer and lead to an overestimated indentation depth and therefore to an underestimation of the elastic modulus. NI next to a stiffer layer will on the other side lead to an underestimation of the indentation depth and an overestimation of E_s. As a further consequence this will also lead to an error in H. Jakes et.al. developed a method to correct load-depth traces for specimen scale flexing and edge effects. [2, 15, 26]. Although it was first developed to investigate wood cell walls, it is applied here for polymeric multilayers. They introduced the structural compliance Cs to describe NI near a free edge or a layer interface. Cs is independent of NI size and adds to the total compliance Ct together with the machine compliance Cm. The property Cm is a constant machine property, which can be calculated during a calibration process. [25] Cs is highly location dependent and needs to be measured for every single NI. In this work quasistatic NI is used in terms of multiload NI to get Ct as a function of F_{max}. Then the modified Stone-Yoder-Sproul (SYS) equation is used [27]:

$$C_t F_{max}^{1/2} = C_s F_{max}^{1/2} + J_0^{1/2}$$

where $J_0^{1/2} = H^{1/2} E_{eff}$ is the square root of the Joslin-Oliver parameter [28]. Now $C_t F_{max}^{1/2}$ is plotted against $F_{max}^{1/2}$ which forms a straight line with slope equal to Cs when H and E_{eff} can be assumed to be independent of NI size. Cs can now be used to correct the load-depth trace in the same way that Cm correction is applied. The corrected H and E_s can then be recalculated as described above.

Multiload experiments were performed with a Bruker-Hysitron TI 950 TriboIndenter (Minneapolis, Minnesota, USA) with a load profile according to Figure 3 with partial loads from 40 µN up to 1 mN. All NI were immediately preceded by a liftoff, offset, and reapproach to an undeformed surface location to minimize surface detection errors. NI was performed in five positions in the y axis for calculation of a mean with standard deviation for every x axis position (index). The indentation scheme is described in Figure 1. For evaluation the smallest two indents were excluded because of accumulation of liquid observed over part of the surface. Displacement drift was measured by fitting the last 30 s of the depth time trace to a straight line. The slope of the straight line corresponds to the displacement rate. After that the whole depth time profile was corrected by the displacement drift rate [11].
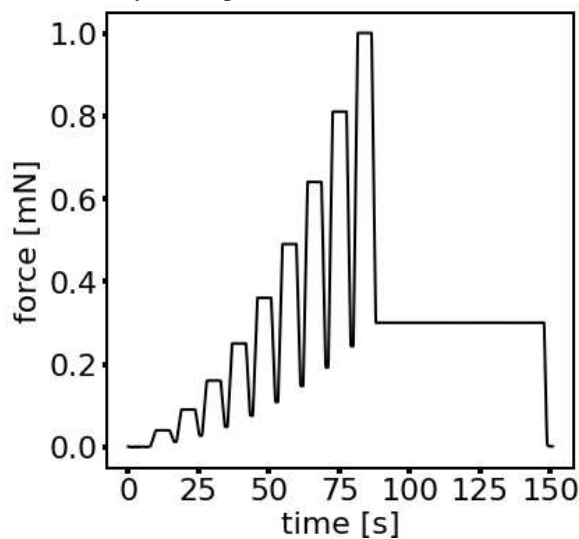

Figure 3:Load profile for measurements on the polymeric multilayer.

The surface was investigated by Scanning Probe Microscopy (SPM) imaging before and after indentation (see *Figure 4*).
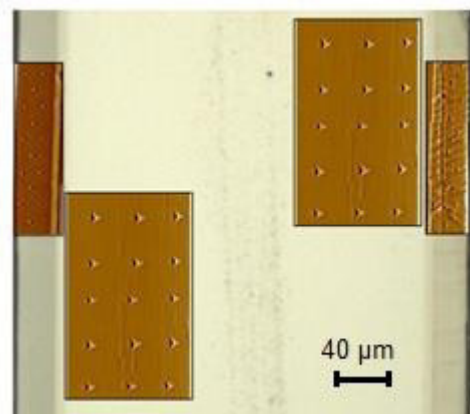

Figure 4:SPM images according to their specific locations on the multilayer after indentation.

Fourier transform infrared spectroscopy (FTIR)

Fourier Transform Infrared (FT-IR) spectroscopy measurements were performed to investigate the composition of the film. Both sides of the film were measured using a SpectrumTwo (PerkinElmer, Inc., USA) in attenuated total reflectance (ATR) mode using a Quest ATR unit (Specac Ltd., United Kingdom) equipped with a diamond crystal. The spectra were recorded over a range from 4000 to 650 cm^{-1}, averaging four scans with a resolution of 4 cm^{-1}.

Differential scanning calorimetry (DSC)

DSC was carried out with a Perkin Elmer DSC 4000 (Waltham, USA) to explore the thermal behavior of the multilayer in the temperature range of 23°C - 280°C with a heating rate of 10 K/min. Here 6.7 mg of the sample were cut and put in a 50 µl pan with perforated lid. Measurements were carried out in nitrogen atmosphere to prevent oxidation processes. Enthalpies and peak temperatures for melting and crystallization were evaluated according to ISO 11357-3 [29].

3. Results and Discussion

FTIR measurements confirmed, that the outer layers of the multilayer consist of PA and PVF [30]. It was neither possible to detect the middle layer nor the adhesive of the multilayer with FTIR. That is why DSC measurements were performed additionally, showing endothermic melting peaks at 176°C, 192°C and 254°C which are typical peaks for PA12, PVF and PET, respectively. This indicates, that the middle layer consists of PET.

For NI results, after subtracting C_m, C_s can be presented as a function of position of the sample (index) as mean and standard deviation (Figure 5a).
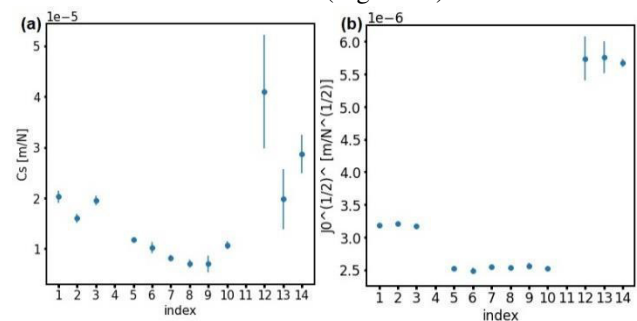
Figure 5: C_s as a function of the position of the indents for the layers PA (1-3), PET (5-10) and PVF (12-14) (a), J_0 as a function of the position of the indents for the layers PA (1-3), PET (5-10) and PVF (12-14) (b): C_s and J_0 are calculated in terms of mean and standard deviation from five measurements in column (compare Figure 1).

From Figure 5a it is obvious that C_s is higher at the edge of the sample (index 1 and 14) but also near the adhesive (index 3, 5, 10 and 12), which means that the adhesive is so soft and basically behaves like a free edge. The standard deviation of C_s from PVF is higher than for PET and PA, because NI on PVF appears to have some imperfections and microcracks (see Figure 4). A microcrack would

behave like a free edge, so a NI near a microcrack in the center of the film would also have a higher Cs. The increased Cs variability demonstrates the importance of assessing Cs at each NI location. The Cs of the PET layer is also higher near the adhesive layer (index 5 and 10) and lower for regions more distant to the adhesive.

The Joslin-Oliver parameter J_0 is shown as a function of the position of the indents for the different layers in Figure 5b. J_0 is an area independent material parameter corresponding to $\frac{H}{E_{eff}^2}$. When J_0 is assessed from a SYS plot, it is also independent of Cs. The observation that J_0 is position independent for every layer suggests that material properties are not varying across the thickness. The different values of J_0 indicate that each layer has different mechanical properties.
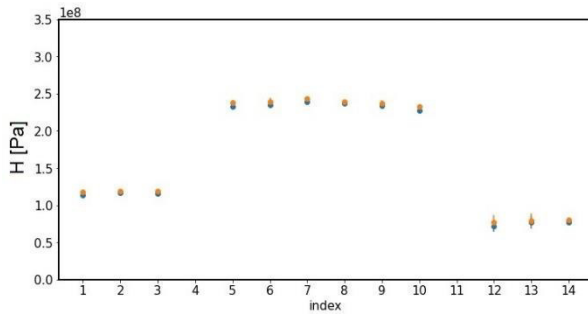

Figure 6: Uncorrected H (blue) and Cs corrected H (orange) as a function of the position of the indents for the multilayer: H is calculated in terms of mean and standard deviation from five measurements in column (compare Figure 1).

The analysis for the Cs has usually only little effect on the hardness calculation [26]. Therefore in Figure 6 small difference between the uncorrected (blue) and the Cs corrected (orange) H is expected. PET as the core layer exhibits the highest hardness of the multilayer.
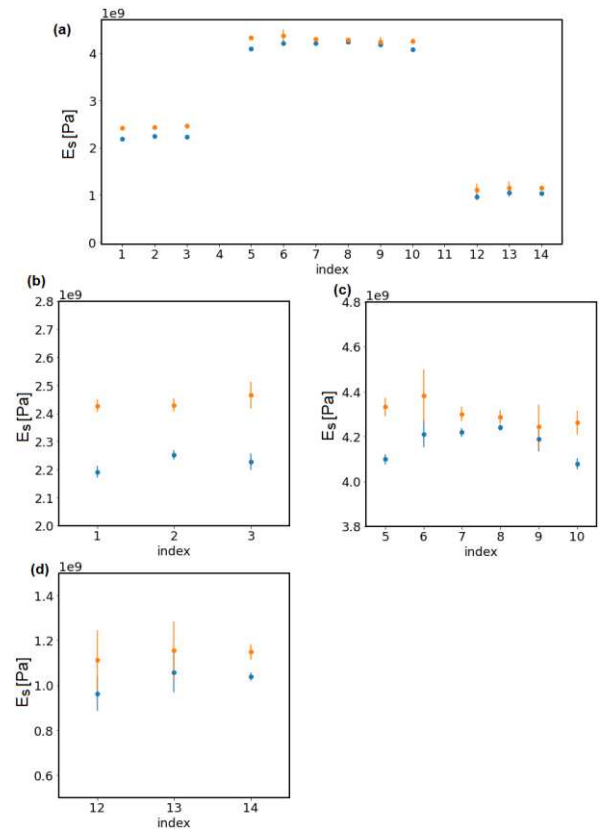
Figure 7: Uncorrected E_s (blue) and Cs corrected E_s (orange) as a function of the position on the multilayer (a), as zoom in for PA (b), PET (c) and PVF (d).

In Figure 7 uncorrected (blue) and Cs corrected (orange) E_s is shown as a function of the indent position (index) on the multilayer. The Cs corrected E_s is significantly higher for the layers PA, PET and PVF than the uncorrected E_s. This confirms that specimen flexing led to an underestimation of E_s. In Figure 7b and c the E_s of the PA and the PET is shown. Here, the uncorrected E_s is lower near the free edge (index 1) and near the interface to the adhesive (index 3 and 5) which indicates that the adhesive is so soft, that it behaves like a free edge from mechanical point of view. After correction for the Cs, there is no significant difference in Es between the position with index 1, 2 and 3. The same behavior can be seen in Figure 7c. The uncorrected E_s is lower near the interface to the adhesive (index 5 and 10) and higher in the bulk region (index 6-9). In Figure 7d there is no significant difference between E_s in the bulk or on the edges of PVF. The observation that the adhesive layer behaves like a free edge clearly demonstrates that when testing BS cross-sections the structural compliance method needs to be used even if the specimen is embedded in epoxy to minimize specimen scale flexing.

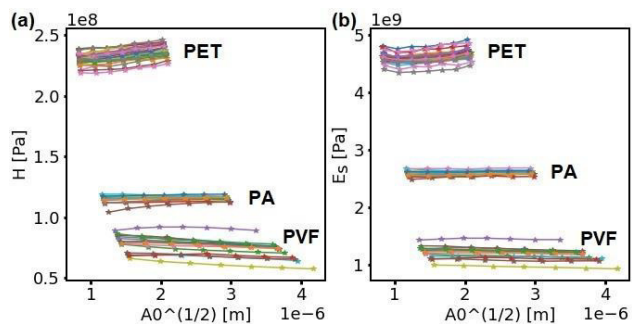*Figure 8: H (a) and Eₛ (b) as a function of indentation area for the layers PET, PA and PVF.*

In Figure 8, H and E_s are given as a function of the area of indentation. While for the layers PA and PVF H and E_s are independent from A_0 and therefore also from indentation depth, there seems to be a size dependency for PET, as H and E_s tend to rise with growing A_0. The first data points with low indentation depth for every layer were eliminated because of surface uncertainties. Further information about the indentation size effect (ISE) is given in [31]. ISE in H leads to a small artefact in terms of an overestimation in the calculation of the Cs. Future work carefully measuring residual contact areas using high resolution imaging [18, 19] would be useful for better understanding the ISE in the PET H.

4. Conclusions

Multilayers are often used in packaging [32] as well as in PV industry [7] to combine certain advantages of different layers. Mechanical characterization of such multilayers is important in order to make statements about their performance and also for further lifetime predictions. At the moment it is state of the art to characterize a multilayer mechanically by tensile test [33], whereby it is only possible to get mechanical properties of the composite. With NI it is possible to investigate single layers of a multilayer mechanically, but artefacts in the measurements arising from sample preparation techniques, specimen scale flexing and edge effects must be considered. In this work it could be clearly demonstrated,

that ultrasmooth surfaces can be prepared using a diamond knife and the structural compliance method can be used to account for specimen scale flexing and edge effect. The Cs was higher at the specimen edges as well as at the boundaries to the adhesive in comparison to the layer bulk. The influence of the Cs to the hardness is not as high as to the modulus. Here specimen scale flexing and edge effect leaves the modulus underestimated in the stiffer polymer layers. Cs correction leads to a more position independent modulus for every layer. Investigations on a multilayer sample cross-section glued on a sample holder and cut with microtomy like described in this article are more reliable than examinations on embedded cross-sections [10] because there are no mechanical or chemical consequences from embedding procedure or grinding. Extracting one layer from a multilayer with further investigations [9] also does not give reliable properties, because the contributions from neighboring layers and potential processing effects are neglected. Multilayer investigations by NI from the top [34] will give information of the top layer with unknown influence of the underneath layers.

In future, cross-sectional investigations of multi layers will give the opportunity to map polymer degradation in different layers and allow predictions about the lifetime of multilayers such as BS.

References

1. Oliver, W.C., Pharr, G.M.: An improved technique for determining hardness and elastic modulus using load and displacement sensing indentation experiments. J. Mater. Res. **7**(6), 1564–1583 (1992). doi: 10.1557/JMR.1992.1564

2. Jakes, J.E., Frihart, C.R., Beecher, J.F., Moon, R.J., Stone, D.S.: Experimental method to account for structural compliance in nanoindentation measurements. J. Mater. Res. **23**(4), 1113–1127 (2008). doi: 10.1557/jmr.2008.0131

3. Oreski, G., Eder, G.C., Voronko, Y., Omazic, A., Neumaier, L., Mühleisen, W., Ujvari, G., Ebner, R., Edler, M.: Performance of PV modules using co-extruded backsheets based on polypropylene. Solar Energy Materials and Solar Cells **223**, 110976 (2021). doi: 10.1016/j.solmat.2021.110976

4. Omazic, A., Oreski, G., Halwachs, M., Eder, G.C., Hirschl, C., Neumaier, L., Pinter, G., Erceg, M.: Relation between degradation of polymeric components in crystalline silicon PV module and climatic conditions: A literature review. Solar Energy Materials and Solar Cells **192**, 123–133 (2019). doi: 10.1016/j.solmat.2018.12.027

5. Eder, G.C., Voronko, Y., Oreski, G., Mühleisen, W., Knausz, M., Omazic, A., Rainer, A., Hirschl, C., Sonnleitner, H.: Error analysis of aged modules with cracked polyamide backsheets. Solar Energy Materials and Solar Cells **203**, 110194 (2019)

6. Geretschläger, K.J., Wallner, G.M., Fischer, J.: Structure and basic properties of photovoltaic module backsheet films. Solar Energy Materials

and Solar Cells **144**, 451–456 (2016). doi: 10.1016/j.solmat.2015.09.060

7. Knausz, M., Oreski, G., Eder, G.C., Voronko, Y., Duscher, B., Koch, T., Pinter, G., Berger, K.A.: Degradation of photovoltaic backsheets: Comparison of the aging induced changes on module and component level. J. Appl. Polym. Sci. **132**(24), n/a-n/a (2015). doi: 10.1002/app.42093

8. Oreski, G., Pinter, G.: Aging Characterization of Multi-Layer Films Used as Photovoltaic Module Blacksheets. 5 pages / 28th European Photovoltaic Solar Energy Conference and Exhibition; 3050-3054 (2013). doi: 10.4229/28thEUPVSEC2013-4AV.4.13

9. INOUE, K., TRIAWAN, F., INABA, K., KISHIMOTO, K., NISHI, M., SEKIYA, M., SEKIDO, K., SAITOH, A.: Evaluation of interfacial strength of multilayer thin films polymer by nanoindentation technique. Mechanical Engineering Journal **6**(1), 18-00326-18-00326 (2019). doi: 10.1299/mej.18-00326

10. IEEE Photovoltaic Specialists Conference; Institute of Electrical and Electronics Engineers; IEEE Electron Devices Society: Mapping chemical and mechanical property degradation in photovoltaic modules. Colorado Convention Center, Denver, Colorado, 8-13 June 2014. 2014 IEEE 40th Photovoltaic Specialists Conference (PVSC), Denver, CO, USA, 6/8/2014 - 6/13/2014. IEEE, Piscataway, NJ (2014)

11. Jakes, J.E., Stone, D.S.: Best Practices for Quasistatic Berkovich Nanoindentation of Wood Cell Walls. Forests **12**(12), 1696 (2021). doi: 10.3390/f12121696

12. Christöfl, P., Czibula, C., Berer, M., Oreski, G., Teichert, C., Pinter, G.: Comprehensive investigation of the viscoelastic properties of PMMA by nanoindentation. Polymer Testing **93**, 106978 (2021). doi: 10.1016/j.polymertesting.2020.106978

13. Fischer-Cripps, A.C., Nicholson, D.W.: Nanoindentation. Mechanical Engineering Series. Applied Mechanics Reviews **57**(2), B12-B12 (2004). doi: 10.1115/1.1704625

14. Christöfl, P., Czibula, C., Seidlhofer, T., Berer, M., Macher, A., Helfer, E., Schrank, T., Oreski, G., Teichert, C., Pinter, G.: Morphological characterization of semi-crystalline POM using nanoindentation. International Journal of Polymer Analysis and Characterization **26**(8), 692–706 (2021). doi: 10.1080/1023666X.2021.1968122

15. Jakes, J.E., Frihart, C.R., Beecher, J.F., Moon, R.J., Resto, P.J., Melgarejo, Z.H., Suárez, O.M., Baumgart, H., Elmustafa, A.A., Stone, D.S.: Nanoindentation near the edge. J. Mater. Res.

24(3), 1016–1031 (2009). doi: 10.1557/jmr.2009.0076

16. Odegard, G.M., Gates, T.S., Herring, H.M.: Characterization of viscoelastic properties of polymeric materials through nanoindentation. Experimental Mechanics **45**(2), 130–136 (2005). doi: 10.1007/BF02428185

17. VanLandingham, M.R., Chang, N.-K., Drzal, P.L., White, C.C., Chang, S.-H.: Viscoelastic characterization of polymers using instrumented indentation. I. Quasi-static testing. J. Polym. Sci. B Polym. Phys. **43**(14), 1794–1811 (2005). doi: 10.1002/polb.20454

18. Jakes, J.E., Lakes, R.S., Stone, D.S.: Broadband nanoindentation of glassy polymers: Part I. Viscoelasticity. J. Mater. Res. **27**(2), 463–474 (2012). doi: 10.1557/jmr.2011.363

19. Jakes, J.E., Lakes, R.S., Stone, D.S.: Broadband nanoindentation of glassy polymers: Part II. Viscoplasticity. J. Mater. Res. **27**(2), 475–484 (2012). doi: 10.1557/jmr.2011.364

20. Christöfl, P., Ottersböck, B., Czibula, C., Macher, A., Teichert, C., Pinter, G., Oreski, G.: Nanoindentation for Fast Investigation of PET Film Degradation. JOM **74**(6), 2287–2294 (2022). doi: 10.1007/s11837-022-05278-0

21. Paredes, J.J., Shaler, S., Howell, C., Jakes, J.: Influence of hot water extraction on cell wall and OSB strand mechanics. Wood Sci Technol **51**(6), 1307–1319 (2017). doi: 10.1007/s00226-017-0951-4

22. Oliver, W.C., Pharr, G.M.: Measurement of hardness and elastic modulus by instrumented indentation: Advances in understanding and refinements to methodology. J. Mater. Res. **19**(1), 3–20 (2004)

23. Domininghaus, H., Eyerer, P., Hirth, T.: Domininghaus - Kunststoffe. Eigenschaften Und Anwendungen, 7th edn. VDI-Buch. Springer, Dordrecht (2008)

24. Strader, J.H., Shim, S., Bei, H., Oliver, W.C., Pharr, G.M.: An Experimental Evaluation of the Constant β Relating the Contact Stiffness to the Contact Area in Nanoindentation. MRS Proceedings **841** (2006). doi: 10.1557/PROC-841-R1.4

25. Jakes, J.E.: Improved methods for nanoindentation Berkovich probe calibrations using fused silica. J Mater Sci **53**(7), 4814–4827 (2018). doi: 10.1007/s10853-017-1922-8

26. Jakes, J.E., Stone, D.S.: The edge effect in nanoindentation. Philosophical Magazine **91**(7-9), 1387–1399 (2011). doi: 10.1080/14786435.2010.495360

27. Stone, D.S., Yoder, K.B., Sproul, W. d.: Hardness and elastic modulus of TiN based on continuous indentation technique and new correlation. Journal of Vacuum Science & Technology A:

Vacuum, Surfaces, and Films **9**(4), 2543–2547 (1991). doi: 10.1116/1.577270

28. Joslin, D.L., Oliver, W.C.: A new method for analyzing data from continuous depth-sensing microindentation tests. J. Mater. Res. **5**(1), 123–126 (1990). doi: 10.1557/JMR.1990.0123

29. International Organisation for Standardisation: Plastics – Differential scanning calorimetry (DSC) Part 3: Determination of temperature and enthalpy of melting and crystallization. ISO 11357-3 (1999)

30. Socrates, G.: Infrared and Raman characteristic group frequencies. Tables and charts, 3rd edn. John Wiley & Sons LTD, Chichester [etc.] (2015)

31. Nix, W.D., Gao, H.: Indentation size effects in crystalline materials: A law for strain gradient plasticity. Journal of the Mechanics and Physics of Solids **46**(3), 411–425 (1998)

32. Koinig, G., Grath, E., Barretta, C., Friedrich, K., Vollprecht, D., Oreski, G.: Lifecycle Assessment for Recycling Processes of Monolayer and Multilayer Films: A Comparison. Polymers **14**(17) (2022). doi: 10.3390/polym14173620

33. Kim, Y., Kim, J., Kim, C.Y., Kim, T., Lee, C., Jeong, K., Jo, W., Yoo, S., Kim, T.-S., Choi, K.C., Im, S.G.: A modulus-engineered multi-layer polymer film with mechanical robustness for the application to highly deformable substrate platform in stretchable electronics. Chemical Engineering Journal **431**, 134074 (2022). doi: 10.1016/j.cej.2021.134074

34. Miller, D.C., Owen-Bellini, M., Hacke, P.L.: Use of indentation to study the degradation of photovoltaic backsheets. Solar Energy Materials and Solar Cells **201**, 110082 (2019). doi: 10.1016/j.solmat.2019.110082

2. SUMMARY AND CONCLUSION

NI of polymers is not trivial. This is mainly because the most used method is the O&P method originally developed to investigate hard and isotropic materials such as metals with primarily elastic-plastic behaviour when being deformed by an external force. When a polymer is deformed by NI, it acts viscoelastic meaning that also the viscous part of the deformation has to be considered in the analysis of the NI curve. In this work, thermoplastic polymers were investigated by NI and also by common macroscopic tests to validate the applicability of different NI measurement methods on viscoelastic polymers.

NI O&P measurements as well as NI creep tests were performed on PMMA, which served as model system for an amorphous thermoplastic polymer. The implementation of creep curves gained by NI combined with material modelling here gave rise to use the occurrence of creep of viscoelastic materials instead of neglecting it. To validate the NI results, also AFM-NI and macroscopic compression tests were performed. Here the moduli results from NI and AFM-NI creep measurements were in the same range as the compression test. The O&P results from NI fitted fairly well too, but the O&P results obtained by AFM-NI showed lower values and therefore, underestimated the elastic modulus.

In addition to the time-delayed balancing of the macromolecules causing viscoelasticity, also the morphology of a polymer influences the results of NI. For this purpose, a semi-crystalline POM sample was investigated space-resolved with NI in cross-section, where indents were performed near the edge of the sample as well as in the middle of the sample. The crystallinity of the POM specimen was varying for the center and the edge of the sample due to the production process. The crystalline phase of POM consists of spherulites, which themselves consist of amorphous phases and radially ordered lamellae. NI experiments were performed in such a way that the size of the spherulites is in the range of the indenter imprint size. The spherulite size and distribution influenced the modulus gained by NI and also its standard deviation. Higher crystallinity led to higher modulus, but also to higher standard deviation due to inhomogeneities caused by the spherulites. A comparison of the mean modulus over the cross-section showed good accordance with the macroscopic compression tests. NI creep tests demonstrated that POM has a more pronounced creep behaviour at the edge zone than at the bulk zone. The spectral representation of creep curves in the experimental window of the NI measurements stated clearly that it is the storage modulus (elastic contribution) that leads to the difference. The loss modulus did not differ significantly, indicating no viscous contribution to the modulus difference between the bulk zone and the edge zone.

For NI experiments on semi-crystalline and amorphous thermoplastics, big -100 µm radius- sphero-conical indenter tips have been used. Polymers exhibiting time-dependent behaviour act linear viscoelastic for low strains. Therefore stress (strain) induced by NI should be decreased by lowering the force or/and by increasing the contact area between the indenter and the polymer. The employment of a large sphero-conical indenter, causing maximum strain which is smaller than the material-dependent elastic strain limit, is suggested. The implementation of time-consuming creep measurements on (semi-crystalline) thermoplastic polymers is not necessarily recommended for investigations of the elastic modulus. Here, the O&P method with appropriate holding time before the unloading phase is sufficient. The creep method in combination with a big sphero-conical indenter tip and material modelling should be used to examine the time-dependent properties like storage and loss modulus.

Polymers applied in demanding applications are degrading sometimes, especially when they are exposed to elevated temperatures and humidity over time. All physical and chemical changes of a polymer summarized during application time are defined as aging. With the knowledge of NI on amorphous and semi-crystalline thermoplastics in the background, the aging behaviour of a thin PET film was investigated by NI and macroscopic tensile tests. This investigation showed that it is possible to determine precise and local elastic moduli of thin PET films with NI comparable to the results of a

tensile test. Also, the elastic modulus of highly-embrittled samples can be determined by NI, which is not possible by tensile test. Degradation is also detectable by NI creep measurements with the same sensitivity as GPC measurements in less effort of time. Thus, they provide fast, reliable and locally resolved information about the early aging of PET. Here, the PET films were embedded in epoxy resin, ground and polished as sample preparation for NI. The influence of the resin on the NI results could not be excluded, but the quantitative analysis of the differently aged samples was meaningful.

To exclude the influence of an embedding material, NI was performed on a cross-section multilayer sample with a special sample holder, where no embedding is needed. Here, the sample was glued to a steel slug and cut with an ultramicrotome equipped with a diamond knife to get an ultrasmooth surface. With NI it was now possible to investigate the single layers of the multilayer mechanically, but artefacts in the measurements arising from specimen scale flexing, edge effects and sample preparation techniques, had to be accounted for in terms of the structural compliance Cs. In the case of a multilayer consisting of three layers glued together with adhesive from photovoltaic application, the Cs was higher at the sample edges and the boundaries to the adhesive in comparison to the bulk layer. The correction of the modulus and the hardness for the Cs resulted in a position-independent modulus and hardness for every layer of the multilayer. Investigations on a multilayer sample cross-section glued on a sample holder and cut with microtomy are more reliable than examinations on embedded cross-sections because there are no mechanical or chemical consequences from the embedding procedure or grinding.

3. OUTLOOK

Dynamic NI methods with a frequency overlay on indentation are explicitly not part of this work and will play a role in further investigations. The comparability of dynamic NI to macroscopic DMA should be part of future experimental work. Here NI could broaden the field of possible studies regarding viscoelastic properties of small, multilayer or multicomponent samples or it could simply play a role as an alternative to DMA.

The mechanical behaviour of multilayers especially near the layer boundaries will also be part of future studies. With the rise of applications, such as additive manufacturing or added spatial functionality, the use of multilayers is expected to increase significantly shortly. Macroscopic properties of layered polymers are already a topic of investigation for several years, but the local mechanical behaviour at the interface between two materials could also play a decisive role about the final properties and should therefore be part of future research.

Another future research topic will be temperature-dependent NI on polymers. Here dynamic NI gives rise to determine a localized Tg with a temperature sweep. The focus of this study will be the validation of NI results by comparison with macroscopic tests like DMA, where a comprehensive investigation regarding different polymeric material classes is still missing.

References

[1]   Baltá-Calleja, F. J., Cagiao, M. E., Adhikari, R., and Michler, G. H. 2004. Relating microhardness to morphology in styrene butadiene block copolymer polystyrene blends. *Polymer* 45, 1, 247–254.

[2]   Baltá-Calleja, F. J. and Kilian, H. G. 1988. New aspects of yielding in semicrystalline polymers related to microstructure: Branched polyethylene. *Colloid & Polymer Sci* 266, 1, 29–34.

[3]   Baur, Brinkmann, Osswald, Rudolph, and Schmachtenberg. 2013. *Saechtling Kunststoff Taschenbuch*. Hanser, Carl, München.

[4]   Bhushan, B. and Koinkar, V. N. 1994. Nanoindentation hardness measurements using atomic force microscopy. *Applied Physics Letters* 64, 13, 1653–1655.

[5]   Binnig, G., Quate, C. F., and Gerber, C. 1986. Atomic force microscope. *Phys. Rev. Lett.* 56, 9, 930–933.

[6]   Briscoe, B. J., Fiori, L., and Pelillo, E. 1998. Nanoindentation of polymeric surfaces. *Journal of Physics D: Applied Physics* 31, 19, 2395.

[7]   Chen, Z. and Diebels, S. 2012. Modelling and parameter re-identification of nanoindentation of soft polymers taking into account effects of surface roughness. *Computers & Mathematics with Applications* 64, 9, 2775–2786.

[8]   Chen, Z. and Diebels, S. 2014. Nanoindentation of Soft Polymers: Modeling, Experiments and Parameter Identification. *Technische Mechanik* 34, 3-4, 166–189.

[9]   Cheng, L., Xia, X., Scriven, L. E., and Gerberich, W. W. 2005. Spherical-tip indentation of viscoelastic material. *Mechanics of Materials* 37, 1, 213–226.

[10]   Cheng, L., Xia, X., Yu, W., Scriven, L. E., and Gerberich, W. W. 2000. Flat-punch indentation of viscoelastic material. *Journal of Polymer Science Part B: Polymer Physics* 38, 1, 10–22.

[11]   Cheng, Y.-T. and Cheng, C.-M. 2005. Relationships between initial unloading slope, contact depth, and mechanical properties for conical indentation in linear viscoelastic solids. *Journal of Materials Research* 20, 4, 1046–1053.

[12]   Christöfl, P., Czibula, C., Berer, M., Oreski, G., Teichert, C., and Pinter, G. 2021. Comprehensive investigation of the viscoelastic properties of PMMA by nanoindentation. *Polymer Testing* 93, 106978.

[13]   Cook, R. F. and Oyen, M. L. 2007. Nanoindentation behavior and mechanical properties measurement of polymeric materials. *International Journal of Materials Research* 98, 5, 370–378.

[14]   Dao, M., Chollacoop, N., van Vliet, K. J., Venkatesh, T. A., and Suresh, S. 2001. Computational modeling of the forward and reverse problems in instrumented sharp indentation. *Acta Materialia* 49, 19, 3899–3918.

[15]   Deslandes, Y., Rosa, E. A., Brisse, F., and Meneghini, T. 1991. Correlation of microhardness and morphology of poly(ether-ether-ketone) films. *Journal of Materials Science* 26, 10, 2769–2777.

[16]   Díez-Pascual, A. M., Gómez-Fatou, M. A., Ania, F., and Flores, A. 2015. Nanoindentation in polymer nanocomposites. *Progress in Materials Science* 67, 1–94.

[17]   Doerner, M. F. and Nix, W. D. 1986. A method for interpreting the data from depth-sensing indentation instruments. *Journal of Materials Research* 1, 4, 601–609.

[18]   Domininghaus, H., Eyerer, P., and Hirth, T. 2008. *Domininghaus - Kunststoffe*. *Eigenschaften Und Anwendungen*. VDI-Buch. Springer, Dordrecht.

[19]   Eaton, P. J. and West, P. 2019. *Atomic force microscopy*. Oxford University Press, Oxford.

[20]   Ehrenstein, G. W. and Pongratz, S. 2013. *Resistance and stability of polymers*. Hanser Publishers, Munich.

[21]   Feng, G. and Ngan, A. H. W. 2002. Effects of Creep and Thermal Drift on Modulus Measurement Using Depth-sensing Indentation. *Journal of Materials Research* 17, 3, 660–668.

[22]   Fischer-Cripps, A. C. 2004. A simple phenomenological approach to nanoindentation creep. *Materials Science and Engineering: A* 385, 1-2, 74–82.

[23]   Fischer-Cripps, A. C. 2011. *Nanoindentation*. Mechanical Engineering Ser. Springer New York, New York, NY.

[24]   Fischer-Cripps, A. C. and Nicholson, D. W. 2004. Nanoindentation. Mechanical Engineering Series. *Applied Mechanics Reviews* 57, 2, B12.

[25]   Flores, A., Ania, F., and Baltá-Calleja, F. J. 2009. From the glassy state to ordered polymer structures: A microhardness study. *Polymer* 50, 3, 729–746.

[26]   Flores, A., Baltá Calleja, F. J., and Asano, T. 2001. Creep behavior and elastic properties of annealed cold-drawn poly(ethylene terephthalate): The role of the smectic structure as a precursor of crystallization. *Journal of Applied Physics* 90, 12, 6006–6010.

[27] Flores, A. and Calleja, F. J. B. 1998. Mechanical properties of poly(ethylene terephthalate) at the near surface from depth-sensing experiments. *Philosophical Magazine A* 78, 6, 1283–1297.

[28] Flores, A., Pieruccini, M., Stribeck, N., Funari, S. S., Bosch, E., and Baltá-Calleja, F. J. 2005. Structure formation in poly(ethylene terephthalate) upon annealing as revealed by microindentation hardness and X-ray scattering. *Polymer* 46, 22, 9404–9410.

[29] Ganser, C. 2014. *Influence of water on mechanical properties of cellulosic materials studied by AFM based methods*. doctoral thesis, Leoben.

[30] Ganser, C., Czibula, C., Tscharnuter, D., Schöberl, T., Teichert, C., and Hirn, U. 2017. Combining adhesive contact mechanics with a viscoelastic material model to probe local material properties by AFM. *Soft matter* 14, 1, 140–150.

[31] García, R. 2002. Dynamic atomic force microscopy methods. *Surface Science Reports* 47, 6-8, 197–301.

[32] Grellmann, W. 2011. *Kunststoffprüfung*. Hanser, Carl, München.

[33] Halalay, I. C., Lukitsch, M. J., Balogh, M. P., and Wong, C. A. 2013. Nanoindentation testing of separators for lithium-ion batteries. *Journal of Power Sources* 238, 469–477.

[34] Hardiman, M., Vaughan, T. J., and McCarthy, C. T. 2016. The effects of pile-up, viscoelasticity and hydrostatic stress on polymer matrix nanoindentation. *Polymer Testing* 52, 157–166.

[35] Hayes, S. A., Goruppa, A. A., and Jones, F. R. 2004. Dynamic nanoindentation as a tool for the examination of polymeric materials. *Journal of Materials Research* 19, 11, 3298–3306.

[36] Herbert, E. G., Oliver, W. C., Lumsdaine, A., and Pharr, G. M. 2009. Measuring the constitutive behavior of viscoelastic solids in the time and frequency domain using flat punch nanoindentation. *Journal of Materials Research* 24, 3, 626–637.

[37] Herbert, E. G., Oliver, W. C., and Pharr, G. M. 2008. Nanoindentation and the dynamic characterization of viscoelastic solids. *Journal of Physics D: Applied Physics* 41, 7, 74021.

[38] Hertz, H. 1882. Ueber die Berührung fester elastischer Körper. *Journal für die reine und angewandte Mathematik* 1435-5345, 92, 156–171.

[39] Hou, X. D. and Jennett, N. M. 2018. Defining the limits to long-term nano-indentation creep measurement of viscoelastic materials. *Polymer Testing* 70, 297–309.

[40] Jakes, J. E. and Stone, D. S. 2011. The edge effect in nanoindentation. *Philosophical Magazine* 91, 7-9, 1387–1399.

[41] Jalili, N. and Laxminarayana, K. 2004. A review of atomic force microscopy imaging systems: application to molecular metrology and biological sciences. *Mechatronics* 14, 8, 907–945.

[42] Jiang, W.-G., Su, J.-J., and Feng, X.-Q. 2008. Effect of surface roughness on nanoindentation test of thin films. *Engineering Fracture Mechanics* 75, 17, 4965–4972.

[43] Lakes, R. 2009. *Viscoelastic Materials*. Cambridge University Press, Cambridge.

[44] Li, H., Ghosh, A., Han, Y. H., and Bradt, R. C. 1993. The frictional component of the indentation size effect in low load microhardness testing. *Journal of Materials Research* 8, 5, 1028–1032.

[45] Lu, H., Wang, B., Ma, J., Huang, G., and Viswanathan, H. 2003. Measurement of Creep Compliance of Solid Polymers by Nanoindentation. *Mechanics of Time-Dependent Materials* 7, 3, 189–207.

[46] Menard, K. P. 2001. *Dynamic mechanical analysis*. *A practical introduction*. CRC Press, Boca Raton, Fla.

[47] Meyer, G. and Amer, N. M. 1988. Novel optical approach to atomic force microscopy. *Applied Physics Letters* 53, 12, 1045–1047.

[48] Moharrami, N. and Bull, S. J. 2014. A comparison of nanoindentation pile-up in bulk materials and thin films. *Thin Solid Films* 572, 189–199.

[49] Monclus, M. A. and Jennett, N. M. 2011. In search of validated measurements of the properties of viscoelastic materials by indentation with sharp indenters. *Philosophical Magazine* 91, 7-9, 1308–1328.

[50] Morita, S., Giessibl, F. J., and Wiesendanger, R., Eds. 2009. *Noncontact atomic force microscopy*. *Volume 2*. NanoScience and Technology. Springer Berlin Heidelberg; Springer e-books, Berlin, Heidelberg.

[51] Nix, W. D. and Gao, H. 1998. Indentation size effects in crystalline materials: A law for strain gradient plasticity. *Journal of the Mechanics and Physics of Solids* 46, 3, 411–425.

[52] Odegard, G. M., Gates, T. S., and Herring, H. M. 2005. Characterization of viscoelastic properties of polymeric materials through nanoindentation. *Experimental Mechanics* 45, 2, 130–136.

[53] Oliver, W. C. and Pharr, G. M. 1992. An improved technique for determining hardness and elastic modulus using load and displacement sensing indentation experiments. *Journal of Materials Research* 7, 6, 1564–1583.

[54] Oliver, W. C. and Pharr, G. M. 2004. Measurement of hardness and elastic modulus by instrumented indentation: Advances in understanding and refinements to methodology. *J. Mater. Res.* 19, 1, 3–20.

[55] Oyen, M. L. 2005. Spherical Indentation Creep Following Ramp Loading. *Journal of Materials Research* 20, 8, 2094–2100.

[56] Oyen, M. L. 2006. Analytical techniques for indentation of viscoelastic materials. *Philosophical Magazine* 86, 33-35, 5625–5641.

[57] Oyen, M. L. 2007. Sensitivity of polymer nanoindentation creep measurements to experimental variables. *Acta Materialia* 55, 11, 3633–3639.

[58] Oyen, M. L. and Bushby, A. J. 2007. Viscoelastic effects in small-scale indentation of biological materials. *IJSURFSE* 1, 2/3, 180.

[59] Popov, V. L. 2010. *Contact Mechanics and Friction*. Springer Berlin Heidelberg, Berlin, Heidelberg.

[60] Rugar, D. and Hansma, P. 1990. Atomic Force Microscopy. *Physics Today* 43, 10, 23–30.

[61] Schmitz, I., Schreiner, M., Friedbacher, G., and Grasserbauer, M. 1997. Phase imaging as an extension to tapping mode AFM for the identification of material properties on humidity-sensitive surfaces. *Applied Surface Science* 115, 2, 190–198.

[62] Slouf, M., Strachota, B., Strachota, A., Gajdosova, V., Bertschova, V., and Nohava, J. 2020. Macro-, Micro- and Nanomechanical Characterization of Crosslinked Polymers with Very Broad Range of Mechanical Properties. *Polymers* 12, 12.

[63] Sneddon, I. N. 1948. Boussinesq's problem for a rigid cone. *Math. Proc. Camb. Phil. Soc.* 44, 4, 492–507.

[64] Stone, D. S., Yoder, K. B., and Sproul, W. d. 1991. Hardness and elastic modulus of TiN based on continuous indentation technique and new correlation. *Journal of Vacuum Science & Technology A: Vacuum, Surfaces, and Films* 9, 4, 2543–2547.

[65] Teichert, C. 2002. Self-organization of nanostructures in semiconductor heteroepitaxy. *Physics Reports* 365, 5-6, 335–432.

[66] Tranchida, D., Piccarolo, S., Loos, J., and Alexeev, A. 2007. Mechanical Characterization of Polymers on a Nanometer Scale through Nanoindentation. A Study on Pile-up and Viscoelasticity. *Macromolecules* 40, 4, 1259–1267.

[67] Tweedie, C. A. and van Vliet, K. J. 2006. Contact creep compliance of viscoelastic materials via nanoindentation. *J. Mater. Res.* 21, 6, 1576–1589.

[68] VanLandingham, M. R., Chang, N.-K., Drzal, P. L., White, C. C., and Chang, S.-H. 2005. Viscoelastic characterization of polymers using instrumented indentation. I. Quasi-static testing. *J. Polym. Sci. B Polym. Phys.* 43, 14, 1794–1811.

[69] VanLandingham, M. R., Villarrubia, J. S., Guthrie, W. F., and Meyers, G. F. 2001. Nanoindentation of polymers: an overview. *Macromol. Symp.* 167, 1, 15–44.

[70] Voyiadjis, G. Z., Ed. 2020. *Handbook of Nonlocal Continuum Mechanics for Materials and Structures*. Springer eBook Collection. Springer International Publishing, Cham.

[71] Voyiadjis, G. Z., Malekmotiei, L., and Samadi-Dooki, A. 2018. Indentation size effect in amorphous polymers based on shear transformation mediated plasticity. *Polymer* 137, 72–81.

[72] Wang, Y., Shang, L., Zhang, P., Yan, X., Zhang, K., Dou, S., Zhao, J., and Li, Y. 2020. Measurement of viscoelastic properties for polymers by nanoindentation. *Polymer Testing* 83, 106353.

[73] Woirgard, J., Dargenton, J.-C., Tromas, C., and Audurier, V. 1998. A new technology for nanohardness measurements: principle and applications. *Surface and Coatings Technology* 100-101, 103–109.

[74] Yang, S., Zhang, Y.-W., and Zeng, K. 2004. Analysis of nanoindentation creep for polymeric materials. *Journal of Applied Physics* 95, 7, 3655–3666.

[75] Yong, Y. K., Ahmed, B., and Moheimani, S. O. R. 2010. Atomic force microscopy with a 12-electrode piezoelectric tube scanner. *The Review of scientific instruments* 81, 3, 33701.

[76] Zhang, C. Y., Zhang, Y. W., and Zeng, K. Y. 2004. Extracting the mechanical properties of a viscoelastic polymeric film on a hard elastic substrate. *J. Mater. Res.* 19, 10, 3053–3061.

[77] Zhao, Y., Wang, G.-C., and Lu Toh-Ming. 2001. *Characterization of amorphous and crystalline rough surface*. *Principles and applications*. Experimental methods in the physical sciences v. 37. Academic Press, San Diego.